Dynamic Mixed-Mode Fracture of Bonded Composite Joints for Automotive Crashworthiness

David J. Pohlit II

Thesis submitted to the faculty of the

Virginia Polytechnic Institute and State University

in partial fulfillment of the requirements for the degree of

Master of Science

in

Engineering Mechanics

David A. Dillard - Chair

Scott W. Case

Rakesh K. Kapania

J. Michael Starbuck

June 15, 2007

Blacksburg, Virginia

Keywords: Fracture, Strain Energy Release Rate, Impact, Mode I, Mixed-Mode I/II, Mode II, Mode III, Driven Wedge, Compact Tension, Stick-Slip, Adhesive Joint, Composite, Beam Theory, Viscoelastic, Fracture Envelope

Dynamic Mixed-Mode Fracture of Bonded Composite Joints for Automotive Crashworthiness

David J. Pohlit II

Abstract

An experimental evaluation of the mixed-mode fracture behavior of bonded composite joints is presented. Commonly used experimental techniques for characterizing the mode I, mixed-mode I/II, mode II, and mode III fracture behavior have been employed for the purpose of developing a fracture envelope to be utilized in the automotive design process. These techniques make use of such test geometries as the double cantilever beam (DCB), asymmetric double cantilever beam (ADCB), single-leg bend (SLB), end-loaded split (ELS), and split cantilever beam (SCB) specimens. Symmetric versions of the DCB, SLB, and ELS specimens produced mode mixities of 0°, 41°, and 90° respectively, while the testing of ADCB specimens allowed for mode mixities of 18°, 31°.

Pronounced stick-slip behavior was observed for all specimen test geometries under both quasi-static and dynamic loading conditions. Due to the nature of the adhesive studied, a limited number of data points were obtained under mode I loading conditions. A significant increase in the number of measurable crack initiation events was observed for mixed-mode I/II loading conditions, where stick slip behavior was less pronounced. Additionally, a comparison of the measured fracture energies obtained under mixed-mode I/II loading conditions reveals that the addition of a small mode II component results in a decrease in the mode I fracture energy by roughly 50%, as the

crack was driven to the interface between the adhesive layer and composite adherends. Furthermore, the propensity of debonds to propagate into the woven composite laminate adherends under mode II loading conditions limited the number of crack initiation points that could be obtained to one or two usable data points per specimen. A limited number of experimental tests using the SCB specimen for mode III fracture characterization, combined with a numerical analysis via finite element analysis, revealed a significant mode II contribution toward the specimen edges. Similarly, FE analyses on full bond width and half bond width SCB specimens was conducted, and results indicate that by inducing a bond width reduction of 50%, the mode II contribution is greatly decreased across the entire width of the specified crack front.

To provide a means for comparison to results obtained using the standard DCB specimen, an alternative driven wedge test specimen geometry was analyzed, as this geometry provided a significant increase in the number of measurable data points under mode I loading conditions. A three-dimensional finite element analysis was conducted to establish ratios of simple beam theory results to those obtained via FEA, $\mathcal{G}_{SBT}/\mathcal{G}_{FEA}$, were of particular interest, as these ratios were used to establish correction factors corresponding to specific crack lengths to be used in correcting results obtained from an experimental study utilizing a driven wedge technique. Corrected results show good agreement with results obtained from traditional mode I double cantilever beam tests.

Finally, bulk adhesive experiments were conducted on compact tension specimens to establish a correlation between adhesively bonded composite joint and bulk adhesive fracture behavior under mode I loading conditions. Measured fracture energy values were shown to gradually drop across a range of applied loading rates, similar to the rate-

dependent behavior observed with both the DCB and driven wedge specimens. Application of the time-temperature superposition principle was explored to determine whether or not such techniques were suitable for predicting the fracture behavior of the adhesive studied herein. Good correlation was established between the fracture energy values measured and the value of tan δ obtained from dynamic mechanical analysis tests conducted at corresponding reduced test rates.

Acknowledgements

The author would like to thank:

- Dr. David Dillard for his generosity, patience, guidance, and willingness to support me throughout the duration of this project both as an advisor and a mentor, as well as providing me with tremendous opportunities to learn and grow, both as a student and an individual.

- Dr. Scott Case for taking the time to serve on my committee and provide me with other invaluable opportunities outside of the classroom, as well as useful discussions on composites prior to my graduate studies.

- Dr. Rakesh Kapania for taking the time to serve on my committee, as well as his willingness to provide valuable guidance relevant to various finite element analysis aspects involved in this research.

- Dr. J. Michael Starbuck for taking the time to serve on my committee, as well as for providing me with valuable opportunities to both visit and serve as a summer intern at Oak Ridge National Lab, where I was able to conduct valuable research and establish invaluable contacts within the organization.

- The Automotive Composites Consortium in coordination with the Department of Energy, under cooperative agreement number DE-FC05-95OR22363, for sponsoring this research. Such support does not constitute an endorsement by the Department of Energy of the views expressed herein.

- Several members of the Polymer Matrix Composites Group at ORNL, including George Jacob (currently with Dow Chemical Co.), Don Erdman, Ronny Lomax, Vlasta Kunc, Bob Norris, and Jeanne Phillips, for valuable help with testing equipment, specimen preparation, FE analysis, preparation of paperwork, and valuable conversation.

- Hitendra Singh, Abhijit Chakraborty, Edoardo Nicoli, and Kshitish Patankar for making my time as a part of the Adhesion Science Lab incredibly enjoyable and fulfilling.

- Bev Williams, along with all of the ESM staff, for always making sure my travel plans were arranged to ensure that I was always where I needed to be when I needed to be there.

- Finally, last but most certainly not least, my parents, Dave and Cheryl, for their undying affection and continued support for all that I have ever done. Thank you for teaching me the meaning of hard work, the value of a dollar, and what it truly takes to be humble. I am most certainly a better person having the both of you as parents.

Table of Contents

List of Figures

List of Tables

Chapter 1: Introduction

1.1: Background

When considering the future of automotive design, polymer composites are regarded as promising candidate materials for reducing overall vehicular weight in order to improve fuel economy while maintaining the structural integrity of today's automotive structures. Although riveting and welding have proven successful in both past and present automotive designs, such traditional fastening techniques can reduce the overall structural integrity by causing stress concentrations around affected areas and are often unsuitable for joining composite materials used in structural applications. The use of adhesives in modern automotive design and fabrication provides substantial benefits compared to traditional joining methods.

Adhesively bonded joints offer greater corrosion resistance and consequently an improved life over traditional welding and riveting [1]. While improving the stiffness and overall strength of joints, adhesives provide a means for reducing the overall weight of today's vehicles without sacrificing the integrity of the structure as a whole. Adhesives also allow for the joining of dissimilar materials, which allows for significant flexibility in material selection and styling when considering the intricacies and aesthetics involved in automotive design. Furthermore, adhesives help to distribute load transfer more evenly through joints due to more uniform in-plane loading conditions, which typically aids in providing increased energy absorption capabilities under impact loading scenarios.

Adhesive joints are commonly examined using a fracture mechanics approach, which states that the overall strength of most solids is determined by flaws already present within the material [2]. In an attempt to predict such behavior, numerous test

methods have been devised in order to characterize the fracture behavior and properties of adhesives. There are three basic modes of crack-tip deformation studied in fracture mechanics: pure opening, or mode I, pure in-plane shearing, or mode II, and out-of-plane or scissor shearing, or mode III. Figure 1.1 illustrates the three basic modes of fracture.

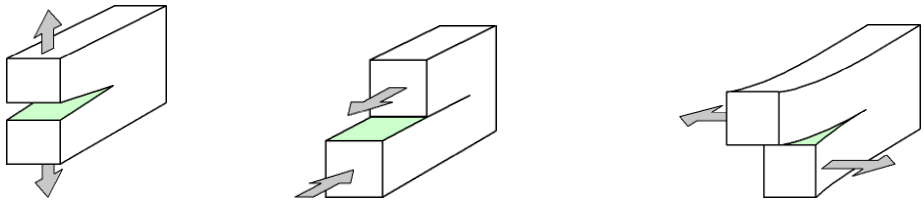

Figure 1.1. Mode I, mode II, and mode III failure modes of fracture [3].

For the purpose of this thesis, all of the above modes of fracture, including that of mixed-mode I/II fracture, will be examined in various bonded composite joint configurations.

1.2: Motivation

The primary goal of this research was to characterize the dynamic fracture behavior of adhesively bonded composite joints under mode I, II, III and mixed-mode I/II applied loading conditions to develop a three-dimensional fracture envelope to be used in automotive design applications. Quasi-static loading conditions were utilized in order to establish baseline characterization values under the various induced modes of fracture; however, results obtained under dynamic loading conditions were of primary concern. Furthermore, bulk material tests were conducted on both the composite adherend and epoxy adhesive materials in order to gather information necessary for future fracture analyses, as well as to establish a means of comparison between bulk dynamic fracture

data and results obtained from bonded joint geometries. Figure 1.2 provides a general depiction of the anticipated fracture envelope to be developed from this work.

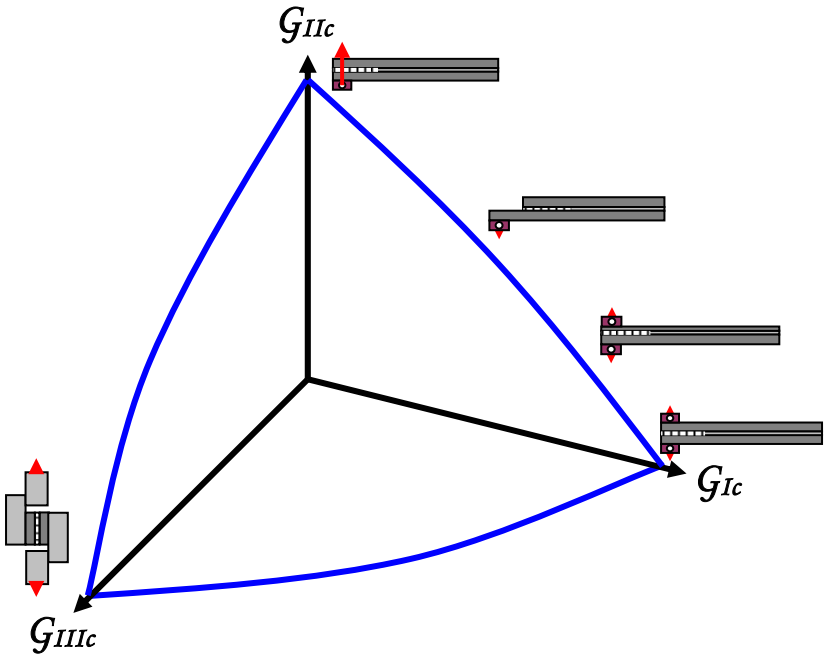

Figure 1.2. Generalized three-dimensional fracture envelope for SIA adhesive.

The modes of fracture studied for the purpose of this thesis were achieved using various specimen geometries: double cantilever beam (mode I), asymmetric double cantilever beam and single leg bend (mixed-mode I/II), end-loaded split (mode II), and split cantilever beam (mode III). All static tests were conducted using an Instron (Norwood, MA) 4505 screw-driven test frame outfitted with a 10kN strain gage-based load cell. All dynamic fracture tests were conducted at Oak Ridge National Laboratory (ORNL – Oak Ridge, TN). Many of these high-rate tests were conducted on a custom-designed MTS (Eden Prairie, MN) servo-hydraulic load frame capable of achieving test velocities up to 18m/s that was outfitted with a Kistler (Winterthur, Switzerland) piezoelectric load cell. In conjunction with the high-rate load frame, a Photron (San Diego, CA) Ultima APX-RS high-speed imaging system was used to acquire crack

propagation data to be used in the dynamic fracture analyses. Additionally, the viscoelastic nature of the adhesive in question was characterized using a TA Instruments (New Castle, DE) Q800 dynamic mechanical analyzer.

1.3: Thesis Organization

This thesis will begin with an in-depth literature review in an attempt to provide sufficient background on and support to the topics that will be addressed throughout the remainder of this thesis. A review of the materials studied, specimen preparation methods followed, and test methods utilized will be discussed next. Finally, this thesis will conclude with the presentation of the analysis methods used, test results obtained, and conclusions drawn from the work conducted for the purpose of this research. This thesis will be organized into the following chapters:

- *Chapter 1*: Provides an introduction to the topics that will be addressed throughout this thesis, including the motivation for performing this research.
- *Chapter 2*: Reviews relevant literature with regards to the following key topics: linear elastic fracture mechanics, test methods for modes I, II, III and mixed-mode I/II fracture, viscoelastic behavior of brittle adhesives, and relevant data analysis methods.
- *Chapter 3*: Presents an overview of the materials used in this research, as well as a detailed account of the test methods used to characterize the quasi-static and dynamic fracture of the various bonded composite joints studied for the purpose of this thesis.

- *Chapter 4*: Provides details pertaining to the analysis methods used to characterize the quasi-static and dynamic fracture behavior of the various bonded composite joint configurations studied for this research.
- *Chapter 5*: Presents the results obtained from this research, including speculation associated with difficulties encountered with regards to dynamic fracture testing of various bonded joint geometries.
- *Chapter 6*: Provides a summary of the research project including relevant conclusions and recommendations for future work.
- *Appendix A*: Correction Factors
- *Appendix B*: Mixed-Mode I/II ADCB Analysis

References

1. Kinloch, A.J., "Interfacial Fracture Mechanical Aspects of Adhesive Bonded Joints – A Review", *Journal of Adhesion*, **10**, 1979, pp. 193-219.

2. Gledhill, R.A. and Kinloch, A.J., "Mechanics of Crack Growth in Epoxide-Resins", *Polymer Engineering and Science*, **19** (2), 1979, pp. 82-88.

3. "Fracture Modes", 2005, Efunda: Engineering Fundamentals, Aug. 29, 2005 http://www.efunda.com/formulae/solid_mechanics/fracture_mechanics/fm_lefm_modes.cfm.

Chapter 2: Literature Review

2.1: Introduction

With an increasing need to make use of adhesives in the joining of dissimilar materials for various load-bearing structures, particularly in the automotive industry, fracture characterization of bonded joints is becoming a necessity. Along with this need, ongoing research has been dedicated to the development of new, and advancement of existing, experimental methods. As such, a focus is needed on all of the various types of failure that can occur in bonded joint configurations, including opening mode (mode I), forward shear (mode II), tearing or out-of-plane shear (mode III), and a combination of any and all of the aforementioned failure modes. While various specimen geometries encompassing all of the different modes of failure have been proposed, only some success has been achieved with regard to the standardization of such test methods. Such geometries include the double cantilever beam (DCB) [1] specimen for mode I and the mixed-mode bending (MMB) [2] specimen for mixed-mode I/II fracture testing.

2.2: Crack Stability

In fracture mechanics tests, stable crack propagation is characterized by a steady, continuous crack growth along the length of the entire test specimen [3]. Unstable crack propagation, or stick-slip behavior, can be characterized as crack jumping from arrest point to arrest point. Such behavior can be characterized by a saw-tooth-shaped load profile, where the load required for crack initiation is greater than that required for stable crack growth [4]. Additionally, others have described this behavior as slow growth through a process zone (stick) followed by rapid crack propagation through virgin

material ahead of the plastic zone (slip) [5]. Several suggestions have been made with regard to why stick-slip behavior occurs, such as specimen geometry, adhesive curing effects, and test condition or environmental effects [5-7].

With regard to unstable, or stick-slip, crack behavior, there are conflicting viewpoints on how to handle the characterization of crack arrest. Many researchers believe that adhesive properties are responsible for crack arrest; therefore static analyses are often utilized in quantifying arrest fracture energy values. Others suggest that dynamic effects must be considered as a result of stress waves and vibrations that occur due to crack acceleration in the slip region, thus resulting in an increase in kinetic energy. Such effects certainly have an effect on resulting crack arrest as a concept of recovered kinetic energy [3]. Moreover, an alternative approach has been suggested for calculating an average fracture energy value, which can be characterized as a change in stored energy divided by the change in crack length for a particular fracture event [8]. However, it should be noted that this value should be considered an upper bound on fracture energy averaged over the corresponding debond area, as kinetic energy may remain post crack arrest or possibly be dissipated during fracture [9]. As a result, initiation fracture energy values will be the primary focus of this thesis given that the arrest values obtained experimentally are believed to be suspect.

2.2.1: Stick-Slip Crack Propagation

Stick-slip behavior, also known as temporal crack instability, is commonly observed in the fracture of adhesively bonded joints [4,7,10]. At a critical strain energy release rate, $\mathcal{G}_c$, rapid, unstable crack growth occurs, thus resulting in decreasing load [7].

Upon reaching an apparent arrest value, $\mathcal{G}_a$, fast crack growth is halted and a period of slow crack growth ensues. For time dependent materials, available energy is converted to kinetic energy that can cause a resulting crack to propagate farther than predicted by static analysis, as a rapidly propagating crack in such materials requires less of the energy that is available. Such a criterion for stick-slip behavior may be stated as [11]:

$$\frac{d\mathcal{G}}{d\dot{a}} > \frac{d\mathcal{G}_c}{d\dot{a}} \tag{2.1}$$

where rate dependence is included for both the applied strain energy release rate, $\mathcal{G}$, and the fracture energy, $\mathcal{G}_c$.

Various features are said to be involved in the development of temporal instability. Inertia effects are believed to result in abrupt crack growth due to a portion of the applied energy being converted to kinetic energy [4]. Additionally, rate dependence of viscoelastic materials is quite sensitive to temperature and strain rate. Furthermore, reflected stress waves propagating through a material are thought to influence the local crack tip stress and strain fields, which directly affect fracture behavior [12].

Using a relationship between strain energy release rate and crack velocity, Maugis [13-14] was able to describe the kinetics associated with crack growth in viscoelastic materials. Describing stick-slip behavior in terms of viscoelastic losses or internal friction at the crack tip, Maugis was able to develop a model describing the effect of crack velocity, $\dot{a}$, on the critical energy release rate, $\mathcal{G}$. For a viscoelastic material, the superposition of the effects of viscoelastic losses and dynamic effects associated with brittle fracture result in two positive branches of the $\mathcal{G}$ versus $\dot{a}$ plot, separated by a negative branch as shown in Figure 2.1 [7].

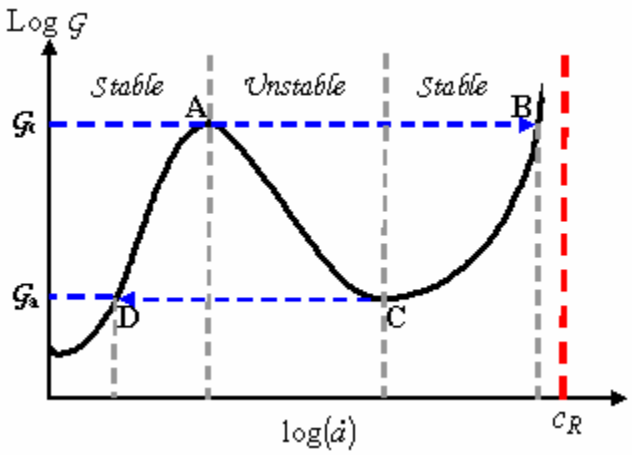

Figure 2.1. Variation in strain energy release rate with crack velocity for a viscoelastic material.

Provided an imposed crack velocity, $\mathcal{G}$ will continue to increase until a critical crack velocity, v_c, is reached. Instability is said to occur when an accelerating crack reaching v_c jumps from point A to point B (slip), as one cannot follow the curve on the negative slope portion of Figure 2.1 due to a decrease in resistance to crack propagation as a result of increasing crack velocity [7]. Similarly, upon slowing down, the ensuing crack jumps from point C to point D (stick), at which point the cycle is repeated for subsequent fracture events.

While the approach provided by Maugis [13-14] provides a reasonable description for stick-slip behavior, it does not account for kinetic energy effects resulting in variability amongst measured fracture energies. Macon *et al.* were able to incorporate a correction to the energy balance that accounted for contributions from kinetic energy, which resulted in a significant reduction in data scatter for measurements of critical strain energy release rate [4]. Research has also shown that such effects can be a direct result of the quality of the developed initiation crack [15-18]. Hine *et al.* were able to show that the measured critical stress intensity factor of polyethersulphone, which should be

independent of specimen geometry and test configuration, varied with significant scatter [17]. It should be noted that when a correction for kinetic energy is implemented, research has shown the shape of the starter crack to be insignificant [4]. In any sense, there are mixed opinions with regard to whether or not fracture energy values measured from an initiation crack should ever be considered in comparative analyses, given the difficulty in generating an appropriate initial flaw [18].

2.2.2: Rate and Temperature Effects

Modern dynamic fracture testing of composite laminates and adhesively bonded composite joints has been pioneered by researchers at Imperial College. Techniques for measuring the mode I [19-20], mode II and mixed-mode I/II [21] fracture behavior of composites and bonded joints have been developed. Additionally, these tests have led to in-depth analysis of dynamic aspects of high-rate tests conducted on high-speed servo-hydraulic test equipment, combined with the development of testing apparatus, such as the loss motion device, necessary for high-rate fracture testing [19-21]. Others have followed the lead in the pursuit of developing relevant test methods for characterizing the dynamic fracture behavior of adhesively bonded joints. Xu *et al.* [22] made use of a falling wedge test in a simple drop tower set-up to determine the mode I impact resistance of electrically conductive adhesives in an inexpensive manner. A similar approach was utilized by Simón *et al.* [8] in not only determining the mode I fracture resistance of bonded composite joints, but also making use of the single leg bend (SLB) and end loaded split (ELS) specimens for mixed-mode I/II and mode II fracture characterization, respectively.

Significant differences may be found in bonded specimens tested at different rates and/or temperatures. With increasing rate or decreasing temperature, unstable crack propagation may occur. However, the initiation of such behavior is dependent on material properties. In the case of rubber-toughened epoxies, much research has shown such material to be highly rate and temperature dependent [23-26]. Additionally, in epoxies, yield stress decreases with increasing temperature or decreasing strain rate, which results in unstable crack propagation due to the formation of greater plastic deformation [6]. Furthermore, stable crack propagation is more likely to occur at lower temperatures where the material in question is below its glass transition temperature, T_g, while maintaining a positive, or possibly zero, slope on the strain energy release rate versus crack velocity curve depicted in Figure 2.1 [27].

Strength and fracture properties of polymers are often correlated with the ability of a viscoelastic material to dissipate energy at small strain rates through the measurement of tan δ via experimental dynamic mechanical analysis [22]. Since the same mechanisms that dissipate energy via viscoelastic behavior are also typically responsible for fracture under large deformations, qualitative relationships can be made between viscoelastic properties, such as tan δ, and fracture properties, such as strain energy release rate. Similarly, some research has had success in quantifying such agreement, which is somewhat surprising given the difference in the large deformations commonly observed in fracture events and the relatively small deformations measured via small strain DMA experiments. Xu *et al.* [22] were able to develop a relationship between the measured fracture energy, G_c, and the loss factor, tan δ, resulting in a very nice correlation between the two different sets of results. This relationship was

established via the development of a master curve, which allowed for the prediction of fracture behavior of a conductive adhesive under impact loading conditions at rates beyond those attainable with modern test equipment. As such, it was found that tan δ was in fact a good indicator of the adhesive's ability to dissipate mechanical energy through heat [22]. Such results could prove quite valuable as DMA tests are much simpler to conduct when compared with traditional fracture experiments; however, relationships should be established only after measurements for tan δ have been made over a range of conditions to be compared with measurements of G_c under constant conditions, as simple linear relationships are not apparent.

2.3: Mode I Fracture

The most widely accepted specimen geometry for determining the mode I strain energy release rate of adhesively bonded joints is the double cantilever beam (DCB). Originally developed by Obreimoff for the assessment of crack propagation in monolithic materials [28], this concept was later extended to the study of adhesive bonds by Ripling and Mostovoy [29-31]. Easily manufactured and implemented experimentally, the DCB test has achieved standardization [1,32] and is typically utilized for characterizing mode I fracture behavior of metals, fibrous composites, and bonded joints. Although the use of tapered DCB specimens has been incorporated by some [33] to account for the variation in slope of the compliance of standard DCB specimens, the standard DCB specimen is typically the specimen geometry of choice due to the cost and complexity associated with manufacturing tapered specimens. In a standard mode I DCB test, a crack is assumed to

be centrally located between two beams, which are subjected to equal and opposite bending moments, as shown in Figure 2.2.

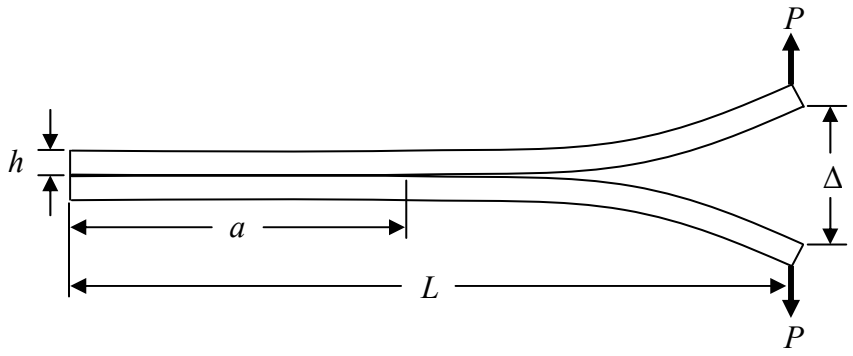

Figure 2.2. Schematic of double cantilever beam (DCB) specimen configuration.

2.3.1: Analysis Techniques

Various methods exist for the analysis of the DCB specimen, many of which are based on the calculated compliance, which is simply the measured opening displacement divided by the applied load. Many compliance-based methods are derived from the following expression originally developed by Irwin and Kies [34]:

$$\mathcal{G}_{Ic} = \frac{P_c^{\,2}}{2b}\frac{dC}{da} \tag{2.2}$$

where P_c is the applied critical load, b is the specimen width, C is the compliance, and a is the crack length.

A commonly used approach for determining the critical mode I fracture energy is based on beam theory. This corrected-displacement method utilized by Blackman *et al.* [19] takes into account beam shear and root rotations, as well as large deflections and end-block effects [36-37]:

$$G_{Ic} = \frac{3}{2}\frac{F}{N}\frac{P\Delta}{b(a+\chi_I h)} \tag{2.3}$$

where Δ is the measured crack tip opening displacement, h is the thickness of one adherend, χ_I is the correction factor for root rotation and crack tip deflection, and F and N are correction factors for large displacements and end-block stiffness effects, respectively. The root rotation and crack tip deflection correction factor, χ_I, can be deduced from the expression for corrected compliance [36]:

$$C = \frac{\Delta}{P} = \frac{8N(a+\chi_I h)^3}{bh^3 E} \tag{2.4}$$

where E is the flexural modulus of the adherend material. Using equation 2.4, the value of χ_I can be determined by plotting $(C/N)^{1/3}$ versus crack length, a, where the intercept of the fit through this data yields the value for χ_I. Additionally, the values for F and N can be determined from the following expressions [36]:

$$F = 1 - \theta_1\left(\frac{\Delta}{a}\right)^2 - \theta_2\left(\frac{l_1\Delta}{a^2}\right) \tag{2.5}$$

$$N = 1 - \theta_3\left(\frac{l_2}{a}\right)^3 - \theta_4\left(\frac{l_1\Delta}{a^2}\right) - \theta_5\left(\frac{\Delta}{a}\right)^2 \tag{2.6}$$

where l_1 and l_2 are end block dimensions provided in Appendix A along with expressions for θ_1 - θ_5.

2.3.2: Dynamic Effects

Often arising during high-rate tests are difficulties acquiring accurate load measurements to be used in subsequent analyses due to dynamic effects. These dynamic effects are likely the result of several possible causes. Inertial effects are believed to have

a great influence on the first peak in the load-time trace for a given test, while oscillations occurring after this initial peak are likely to be caused by stress waves propagating in the test specimen [19,37]. Such phenomena often lead to resonance within load cells, which can result in errors when trying to incorporate load data obtained from measured load traces into typical data analyses. A method for eliminating the need to know measured load data at all is suggested in the form of a displacement analysis method [19]. Again, using compliance as in the static tests, the mode I critical fracture energy can be calculated based on measured displacements and corresponding crack lengths [19]:

$$\mathcal{G}_{Ic} = \frac{3}{16}\frac{F}{N^2}\frac{\Delta^2 h^3 E}{\left(a + \chi_I h\right)} \tag{2.7}$$

As such, the displacement method does not require any knowledge of measured load data, which eliminates possible sources of error associated with erratic load measurements; however, does not take into account kinetic energy effects commonly associated with high-rate testing.

To account for kinetic energy effects, Blackman *et al.* [37] provided an approximation based on the Berry Method where the assumption of a static displacement profile is made to allow for the derivation of crack velocities and thus, computation of kinetic energy. Considering two different cases, a crack velocity of zero prior to crack initiation and steady-state crack propagation where there is a velocity contribution to crack propagation, two expressions for the calculation of the strain energy release rate can be determined. For the instance prior to crack initiation, $\dot{a} = 0$ [37]:

$$\mathcal{G} = \left(\frac{3}{8}\frac{Eh^3V^2}{a^4}\right)t^2 - \left(\frac{33}{280}\frac{EhV^2}{c^2}\right) \tag{2.8}$$

where V is equal to the velocity of one adherend, or half of the applied loading rate, t is time, and c is the longitudinal wave speed in the adherend material, which can be calculated for plane stress conditions as [37]:

$$c = \sqrt{\frac{E}{\rho}} \tag{2.9}$$

or for plane strain conditions as [37]:

$$c = \sqrt{\frac{E}{\rho\left(1-\nu^2\right)}} \tag{2.10}$$

where ρ and υ are the density and Poisson's ratio of the adherends respectively. Likewise, for steady-state crack propagation, $\dot{a} > 0$, the strain energy release rate can be calculated as [37]:

$$\mathcal{G} = \left(\frac{3}{8}\frac{Eh^3V^2}{a^4}\right)t^2 - \left(\frac{111}{560}\frac{EhV^2}{c^2}\right) \tag{2.11}$$

Furthermore, it has been determined that the $\mathcal{G}$ required for steady-state crack propagation is less than that required for crack initiation, which means that there is a transition region related to a mismatch in the boundary conditions between $\dot{a} = 0$ and $\dot{a} > 0$ [37]. Hence, a perturbation study was conducted as an approximation for determining the transient effects associated with this transition region that contribute to the kinetic energy effects associated with high-rates of test [37]. As such, it was concluded that this transition region is responsible for the major dynamic effect contributions in the DCB test. Due to the heavy contribution of material properties to these dynamic effects, it is unclear when such analyses should be employed. Additionally, it has been shown that at test velocities less than 2 m/s, such effects are negligible for a range of materials similar to those utilized herein [38]. Since fracture

energies calculated using traditional static analyses result in conservative estimates, often times the incorporation of dynamic effects is ignored.

2.4: Mixed-Mode I/II Fracture

Given that adhesively bonded joints are rarely subjected to just pure opening (mode I) or pure shear (mode II) modes of loading, the study of a combination of these two modes is crucial in characterizing fracture behavior. Providing useful information in the region between mode I and mode II, mixed-mode I/II fracture data is very important in the development of fracture envelopes. While loading mode plays a key role in determining the level of mode mixity present in an adhesively bonded joint, both materials and geometry also contribute to this factor as well, often a result of the joining of dissimilar materials or geometric asymmetry.

Many specimen configurations can be developed for the study of mixed-mode I/II fracture behavior, simply by incorporating asymmetry into a standard mode I or mode II specimen geometry. For example, some common mixed-mode configurations that make use of this strategy are the asymmetric double cantilever beam (ADCB), asymmetric end notch flexure (AENF), and asymmetric end loaded split (AELS) specimens. Additionally, this same technique can be incorporated into standard mixed-mode I/II specimens such as the single leg bend (SLB), also known as the fixed-ratio mixed-mode (FRMM), and mixed-mode bending (MMB) specimens. By incorporating asymmetry into the geometry of several specimen configurations, various levels of mode-mixity are available for study, thus allowing for a greater characterization of the mixed-mode I/II fracture behavior of a given material system.

The SLB specimen, a form of which has been implemented by Davidson *et al.* [39], lends itself nicely to both quasi-static and dynamic testing as the specimen geometry is quite simple and easy to manufacture. However, in order to allow for dynamic testing on modern servo-hydraulic machines, an adaptation of the SLB specimen has been utilized extensively by several experimentalists [21,40-41]. Figure 2.3 provides an illustration of the SLB specimen geometry.

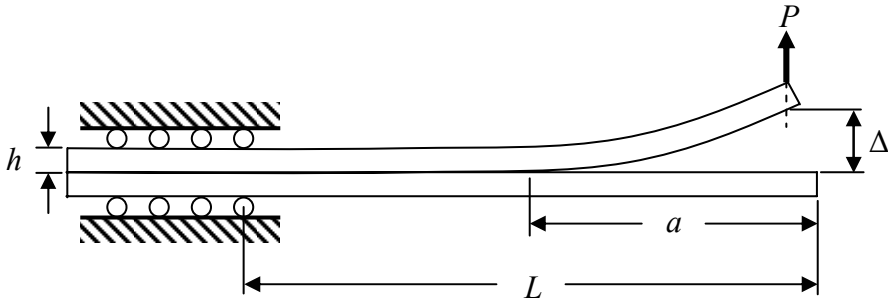

Figure 2.3. Schematic of single leg bend (SLB) specimen configuration.

The ADCB specimen is also commonly utilized [42-45] as it is easily manufactured and tested experimentally in the same fashion as the standard DCB. By altering the thicknesses of the bonded adherends, a limited range of mode-mixities are available. Due to its simplicity and ability to be tested under dynamic loading conditions, the ADCB configuration has been utilized, in combination with the SLB specimen geometry, over a range of applied loading rates for characterizing the mixed-mode I/II fracture behavior of the bonded composite joints studied herein. Figure 2.4 provides a schematic of the ADCB specimen geometry.

The MMB specimen is a widely accepted method for acquiring mixed-mode I/II fracture data [2]. Originally developed by Reeder and Crews [46], the MMB configuration produces fracture under a complete range of mixed-mode I/II conditions

from a single specimen, as it is essentially a combination of DCB and ENF loading conditions [47]. A common difficulty associated with the MMB test is the presence of geometric nonlinearity resulting from large displacements, which makes the analysis of such specimens much more complex. To help alleviate this problem, several iterations and modifications have been made to the original test configuration [40,48]. However, although the MMB specimen works quite well under quasi-static loading conditions, it does not lend well to impact studies, thus it has not been used for the study conducted herein.

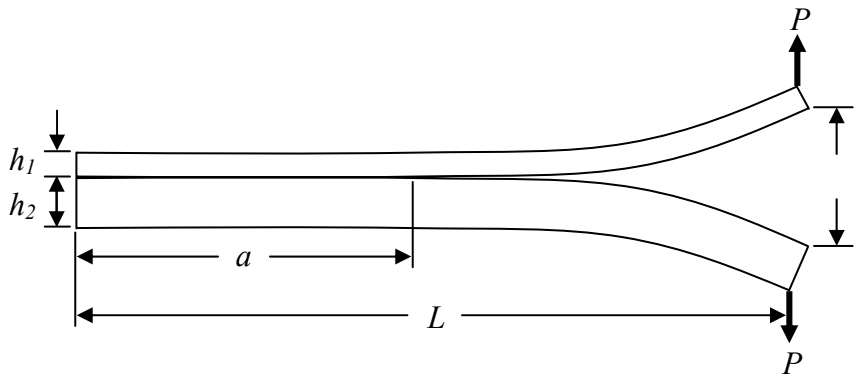

Figure 2.4. Schematic of asymmetric double cantilever beam (ADCB) specimen geometry.

2.4.1: Analysis Techniques

A general mixed-mode failure criterion has been developed by Charalambides *et al.* [49], which assumes that a crack loaded with $\mathcal{G}_{\mathrm{I}}$ and $\mathcal{G}_{\mathrm{II}}$ will have an induced mode I component equal to the failure value, $\mathcal{G}_{\mathrm{o}}$, such that:

$$\mathcal{G}_o = \mathcal{G}_c\left[\cos^2(\psi-\psi_o)+\sin^2\omega\sin^2(\psi-\psi_o)\right] \tag{2.12}$$

where $\mathcal{G}_{\mathrm{c}}$ is the measured fracture energy, ψ is the phase angle of the applied loads, ψ_o is the phase angle which arises from the elastic mismatch across a bimaterial interface and is equal to zero when the materials are elastically identical, and ω is the slope of the

fracture surface roughness, or equal to zero for smooth surfaces [40]. The parameters $\mathcal{G}_o$, ψ_o, and ω can be determined by combining equation 2.12 with the following:

$$\sin^2 \omega = \frac{\mathcal{G}_o}{\mathcal{G}_{Ic}} + \frac{\mathcal{G}_o}{\mathcal{G}_{IIc}} - 1 \tag{2.13}$$

$$\tan^2 \psi_o = \left(1 - \frac{\mathcal{G}_o}{\mathcal{G}_{Ic}}\right) \Big/ \left(1 - \frac{\mathcal{G}_o}{\mathcal{G}_{IIc}}\right) \tag{2.14}$$

where $\mathcal{G}_{Ic}$ and $\mathcal{G}_{IIc}$ are the mode I and mode II critical fracture energies respectively, which can be experimentally measured [49].

For the ADCB geometry, the total mixed-mode strain energy release rate can be estimated by treating the specimen as two separate elastic cantilever beams. By finding the derivative of the strain energy stored in the beams with respect to crack length, a, the resulting strain energy release rate can be calculated using beam theory [42]:

$$\mathcal{G}_{I/IIc} = \frac{3\Delta^2 E_1 E_2 h_1^3 h_2^3}{8a^4\left(E_1 h_1^3 + E_2 h_2^3\right)} \tag{2.15}$$

where E_1, E_2, h_1, and h_2 are the elastic moduli and thicknesses of the two adherends respectively, and Δ is the opening displacement. The above equation provides a good approximation for crack lengths much larger than the beam thicknesses and assumes that the only contribution to the stored energy comes from the bending of the adherends; however, this simple beam model proves to be too stiff for shorter cracks. To more accurately describe the mixed-mode fracture behavior of the ADCB specimen, Creton *et al.* [50] applied Kanninen's beam on elastic foundation model [51] to the simple beam model for calculating $\mathcal{G}_{I/II}$:

$$\mathcal{G}_{I/IIc} = \frac{3\Delta^2 E_1 h_1^{\,3} E_2 h_2^{\,3}}{8a^4}\left[\frac{E_1 h_1^{\,3} C_2^{\,2} + E_2 h_2^{\,3} C_1^{\,2}}{\left(E_1 h_1^{\,3} C_2^{\,3} + E_2 h_2^{\,3} C_1^{\,3}\right)^2}\right] \tag{2.16}$$

where $C_1 = 1 + 0.64 h_1 / a$ and $C_2 = 1 + 0.64 h_2 / a$. It should be noted, however, that in the development of equation 2.16, the foundation modulus was chosen rather arbitrarily, yet the resulting relationship provided a good correlation with experimental data.

Along with the aforementioned models, several alternatives have been presented as well. One such alternative, labeled the global method, was proposed by Williams [52]. Assuming that pure mode II loading is obtained when the curvature of the two adherends of the ADCB specimen is the same, it has been shown that the global method always predicts pure mode I loading as in the symmetric DCB specimen [53], which is certainly not conducive to characterizing the mixed-mode fracture behavior of ADCB specimens. Alternatively, Suo and Hutchinson developed a local method approach, which takes into account the local singular field close to the crack tip and utilizes stress intensity factor partitioning in determining the resulting strain energy release rate [54]. Finite element results [54], combined with experimental results obtained using the local method, suggest that the use of the local method provides a good approximation of the total mixed-mode fracture energy for the ADCB specimen geometry. Key equations involved in the local method approach are provided in Appendix B.

Just as with the DCB geometry, a corrected beam theory approach has been commonly utilized in determining the mode I and mode II portions of the total mixed-mode fracture energy, $\mathcal{G}_{I/IIc}$, for the SLB specimen geometry. Blackman *et al.* suggest a displacement-based approach when considering dynamic loading conditions for symmetric SLB specimens [21]:

$$\mathcal{G}_{Ic} = \frac{12\Delta^2 h^3 E\left(a+\Delta_I\right)^2}{\left[7\left(a+\Delta_{II}\right)^3+\left(L+2\Delta_I\right)^3\right]^2}\cdot\frac{F}{N^2} \tag{2.17}$$

$$\mathcal{G}_{IIc} = \frac{9\Delta^2 h^3 E\left(a+\Delta_{II}\right)^2}{\left[7\left(a+\Delta_{II}\right)^3+\left(L+2\Delta_I\right)^3\right]^2}\cdot\frac{F}{N^2} \tag{2.18}$$

where Δ is the opening displacement, h is the adherend thickness, E is the adherend flexural modulus, a is the crack length, L is the free length of the specimen, Δ_I and Δ_{II} are mode I and mode II correction factors for root rotation and crack-tip deflection respectively, and F and N are correction factors for large displacements and end-block stiffness effects respectively. The mode II crack length correction factor, Δ_{II}, can be approximated as $0.42\Delta_I$ [40]. Furthermore, the correction factors, F and N, can be calculated using the equations provided in Appendix A.

2.4.2: Dynamic Effects & Stability Issues

As discussed previously with regard to the DCB specimen, the inability to accurately measure loads associated with high-rate testing of various mixed-mode specimens results in the need for kinetic energy corrections. Details regarding the procedure utilized to determine the kinetic energy contribution for the SLB test can be found in the literature [21]. Based on previous studies [21], the resulting kinetic energy term for tests conducted up to 3 m/s was shown to be less than 3% of the static fracture energy calculated using equations 2.17 and 2.18 for materials similar to those utilized herein. This same procedure can be applied to the ADCB specimen geometry by incorporating asymmetric thicknesses and elastic moduli into the equations derived in

[21]. Furthermore, it has been shown that stable crack propagation can be obtained in the SLB specimen under static loading conditions for $a/L \geq 0.41$ [21].

2.5: Mode II Fracture

While mode I fracture experimentation has achieved a standardized test method in the double cantilever beam specimen, little progress has been made in recent years toward the establishment of a mode II fracture testing standard. This is somewhat of a surprise given the extensive international round robin conducted in 1997 [55], which featured the testing of four different mode II specimen geometries: end-notched flexure (ENF), stabilized end-notched flexure (SENF), 4-point end-notched flexure, and end loaded split (ELS). A loading schematic of the ELS specimen is provided in Figure 2.5, as this specimen has been utilized for all mode II testing conducted herein.

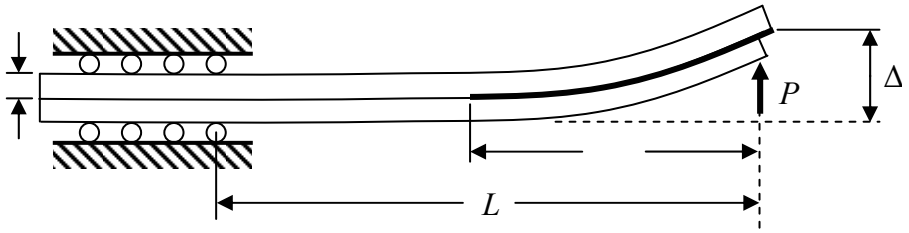

Figure 2.5. Schematic of end loaded split (ELS) specimen geometry.

With goals of determining the influence of test configuration on $\mathcal{G}_{IIc}$ values, examining the influence of crack starter types, assessing the difficulties associated with each test configuration, and evaluating various data reduction methods, one would presume that such involved research would lead to the development of an eventual test standard; however, that is not yet the case [55].

The most commonly utilized mode II test configuration is that of the ENF specimen, which is already a testing standard for the Japanese Industrial Standards (JIS) group [56] and the European Association of Aerospace Industries (AECMA) [57]. The development of the ENF specimen geometry was originally based on work involving the fracture of wood [58]. The ENF test is highly unstable for the range of crack lengths where $a/L < 0.7$ and yields only initiation values of $\mathcal{G}_{\mathrm{IIc}}$, which is why the ENF has not yet achieved international standardization. A variation of this geometry, the SENF test, is much more complex in that it requires known measurements for the crack shear displacement, which is used to control the real-time loading of the specimen [59]. Thus, due to the complex nature of utilizing the SENF specimen, it has been deemed inefficient for international standardization despite the fact that it does provide stable crack propagation. Additionally, the 4ENF test proposed by Martin *et al.* [60] expands even further on the original ENF specimen geometry; however, investigations into the effects of friction reveal that such phenomena are more significant in the 4ENF test than in the original ENF test [61-62]. Combined with difficulty in measuring crack lengths, the 4ENF test has also been deemed unsuitable for standardization.

Originally introduced at Texas A&M [63] and later employed by Russell and Street [64], the ELS specimen has been subjected to several round-robin studies, which have yielded two main conclusions. Many researchers have found it difficult to obtain accurate measured crack lengths, as localized damage in the ELS specimen is only made worse via the use of high-powered optical imaging systems. Secondly, specimen clamping in the test fixture appeared to induce variability among test results [55,59]. However, ongoing research has led to the development of advancements in the

development of alternative techniques that eliminate the need to obtain measured crack lengths for subsequent analyses [59,65], which further increases the accuracy of calculated strain energy release rate values.

2.5.1: Analysis Techniques

Similar to that of the DCB test, an experimental compliance method based on beam theory has often been implemented in calculating the mode II strain energy release rate. Although resting on a rigid foundation instead of an assumed elastic foundation as in the case of the DCB, finite element analyses conducted on the ELS specimen geometry by Wang *et al.* [66] showed that the crack length correction, Δ_{II}, is similar to the value obtained for that of the DCB. Given that the adherends of an ELS specimen are bent in the same direction instead of opposite one another, as is the case with the DCB specimen, this crack length correction is expected to be less than that of the DCB as well. Based on FE results, it was determined that Δ_{II} should be approximately half that of Δ_I [66].

Using a beam theory approach, the mode II strain energy release rate for the ELS specimen geometry can be calculated [65]:

$$G_{IIc} = \frac{9P^2\left(a+\Delta_{II}\right)^2}{4b^2h^3E}\cdot F \tag{2.19}$$

where P, a, b, h, and E are parameters previously described, and F is a correction for large displacements, equations for which can be found in Appendix A. As mentioned previously, Δ_{II} is a correction factor for root rotation and crack tip deflection and can be determined in various ways. The mode II length correction factor can be approximated as $0.42\Delta_I$, where Δ_I is determined from the mode I DCB test as previously discussed. However, in estimating a value for Δ_{II} based on a value of Δ_I, there is an assumption that

the constraint at the clamping point in the ELS test is equivalent to the assumed built-in end constraint of the DCB test, which may not be valid. In fact, research has shown that such an assumption would actually lead to an over-correction of the free length, L [65]. Additionally, approximating Δ_{II} does not take into account the severity of the clamping condition on the ELS specimen. In other words, a lightly clamped specimen may deflect and rotate more at the point of the applied clamp than a specimen clamped to a higher torque and more tightly secured should the surface of the specimen lose contact with the test fixture. As such, other researchers have shown that the additional incorporation of a clamp correction factor, Δ_{clamp}, provides more accurate calculations for strain energy release rate [59,65].

In order to determine a value for Δ_{clamp}, an inverse ELS test is performed, where the cracked portion of the specimen is held completely within the clamp of the test fixture, so that $a = 0$, and thus the un-cracked beam compliance, C_o, can be determined [65]:

$$\left(\frac{C_o}{N}\right)^{1/3} = \left(\frac{1}{2bh^3E}\right)^{1/3} L + \left(\frac{1}{2bh^3E}\right)^{1/3} \Delta_{clamp} \tag{2.20}$$

Thus, by measuring C_o for a variety of different span lengths, L, a plot of $(C_o/N)^{1/3}$ versus L will yield the clamp correction, which is equal to the negative L-axis intercept of the aforementioned plot. Therefore, the compliance of the cracked specimen, when subjected to mode II loading conditions using the ELS specimen, can be calculated as [65]:

$$C = \frac{\Delta}{P} = \frac{3\left(a + \Delta_{II}\right)^3 + \left(L + \Delta_{clamp}\right)^3}{2bh^3E} \cdot N \tag{2.21}$$

Hence, the mode II strain energy release rate, $\mathcal{G}_{IIc}$, can be calculated via a work-based method as:

$$\mathcal{G}_{IIc} = \frac{9P\Delta\left(a+\Delta_{II}\right)^2}{2b\left[3\left(a+\Delta_{II}\right)^3+\left(L+\Delta_{clamp}\right)^3\right]}\cdot\frac{F}{N} \tag{2.22}$$

2.5.2: Dynamic Effects & Stability Issues

Due to the same concerns raised over oscillatory load measurements as a result of dynamic loading conditions, Blackman *et al.* recommend the use of a displacement-based analysis, method for calculating $\mathcal{G}_{IIc}$ [21]:

$$\mathcal{G}_{IIc} = \frac{9\Delta^2 h^3 E\left(a+\Delta_{II}\right)^2}{\left[3\left(a+\Delta_{II}\right)^3+\left(L+2\Delta_{I}\right)^3\right]^2}\cdot\frac{F}{N} \tag{2.23}$$

However, the compliance calculation shown in equation 2.21 can also be utilized to incorporate the clamp correction as well. As discussed previously for both mode I and mixed-mode I/II loading conditions, the need to incorporate the effects of kinetic energy associated with dynamic loading has been analyzed for the mode II ELS specimen geometry. Blackman *et al.* showed that the use of standard static analysis methods resulted in $\mathcal{G}_{IIc}$ values within 3% of those calculated using dynamic methods, which incorporate kinetic energy effects [21]. It should be noted, however, that these findings were limited to test rates of > 3 m/s, thus concluding that static analyses are sufficient for test velocities lower than this value.

Along with load measurement issues, stability concerns also arise when dynamic loading conditions are implemented in experimental fracture testing. Blackman *et al.* reported findings of highly unstable crack propagation, or stick-slip, behavior when utilizing the ELS specimen [21] for both quasi-static and high-rate fracture testing.

Results from previous research conducted by Blackman *et al.* also indicate that in order to achieve stable crack propagation when making use of the ELS specimen, a stability condition of $a/L \geq 0.6$ should be used [36,55,65]. Other researchers have achieved results similar to this, although a stability condition of $a/L \geq 0.5$ has also proved to be sufficient for achieving stable crack propagation as well [66-67]. In any case, it has been shown that by ensuring a crack length to free length ratio greater than 0.6, stable crack growth should be obtained. Additionally, it has been concluded that both specimen configuration and material play a role in determining the level of stability achievable in any particular type of fracture test [21].

2.6: Mode III Fracture

While existing fracture data on composites and adhesively bonded joints concentrate primarily on mode I and mode II types of failure, with varying levels of mode-mixity in between, very little research has been successfully conducted on the study of mode III, or tearing mode, failures. While several different specimen geometries have been proposed, there has yet to be an acceptable configuration for testing standardization. Although it is thought that mode III type failures dominate only in certain complex loading conditions, it is imperative to be able to quantify such material system limitations in order to accurately account for all possible types of failure.

One proposed geometry for the study of mode III fracture is that of the crack rail shear (CRS) specimen [68-69]. Considering both double and single crack versions of the CRS specimen, finite element analysis has shown that mode III failure is dominant. While mode I and II components are present, they have been shown to be small [69].

However, given the very low compliance of the CRS specimen, an experimental compliance analysis technique could not be employed, thus requiring the use of strain gauges for the detection of crack growth. Furthermore, high coefficients of variation (up to 25%) for the mode III strain energy release rate have been reported for the CRS specimen and the crack growth has been proven to be non-uniform [70].

Another geometry utilized for the study of mode III fracture is the edge-crack torsion specimen [71]. Making use of simple specimen geometry and corresponding test apparatus, the ECT test is easily implemented experimentally. Additionally, experimental compliance and classical lamination theory (CLT) techniques are utilized for data analysis, both of which are easily implemented. However, it has been shown that several specimens are needed in order to obtain one data point. In addition, with the inclusion of CLT into the data analysis techniques, there has been observed discrepancies between the value of D_{66}, a stiffness constant, predicted by CLT and that measured experimentally [72]. Furthermore, it has been shown that the ECT test is specimen lay-up dependent for tests conducted on composite laminates [72]. Finally, as with several other proposed mode III test configurations, a mode II contribution has been shown to exist near the ends of the specimen at the points of loading and support [73].

Donaldson *et al.* [74-75] made use of a split cantilever beam (SCB) specimen, which is very similar to the standard DCB test, with the exception that the applied loading direction is parallel to the crack instead of perpendicular. Figure 2.6 illustrates this more clearly.

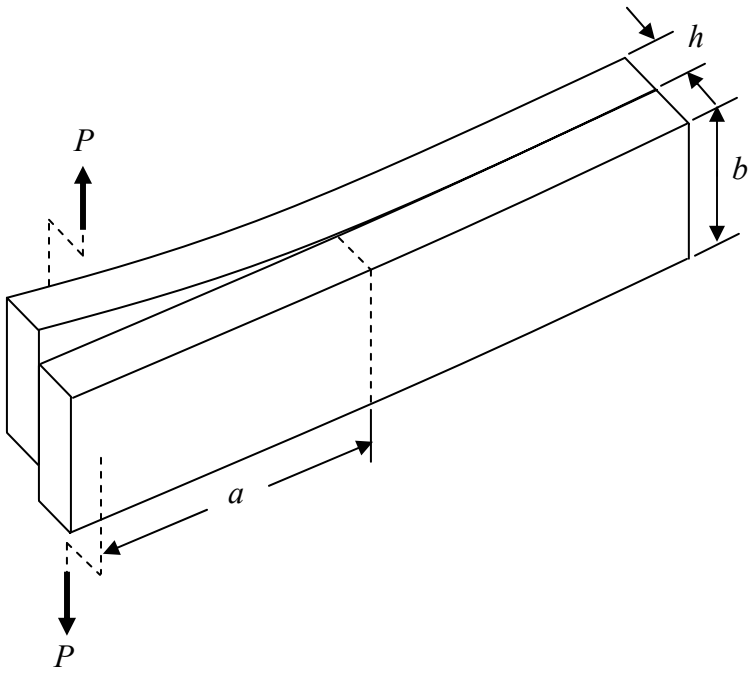

Figure 2.6. Schematic of split cantilever beam (SCB) specimen geometry.

While the SCB specimen is easily manufactured and lends itself nicely to impact loading conditions via a relatively simple testing apparatus, there are several items that must be addressed prior to drawing any significant conclusions from experimental data. First, research has shown that there is a small opening, or mode I, component at the point of the applied load [75]. However, the significance of the mode I contribution can not be quantified without the aid of an in-depth finite element analysis study. Additionally, it should also be noted that for short crack lengths, the SCB specimen geometry provides close to pure mode III loading. Martin *et al.* have shown that there exists a significant mode II contribution near the specimen edges via finite element analysis [76-77]. For a crack length, a = 25.4 mm, it was concluded that mode III failure was dominant along approximately 85% of the crack front, while mode II failure was dominant in the region of approximately 15% near the specimen edges [76]. In addition, for a crack length, a =

127.1 mm, the crack front was shown to be dominated by mode III for about 55%, while mode II dominated the remaining 45% of the SCB specimen [76].

As such, an alternative test apparatus has been proposed [76] that eliminates the bending moment at the crack front by imposing two loads on each arm of the specimen such that the net moment is zero; however, the apparatus described in [76] has not been utilized for the study conducted herein. Results indicate that true mode III failures were induced using the proposed alteration to the original SCB testing apparatus. Although several flaws have been proven to be present in determining the mode III strain energy release rate using the SCB specimen, it does hold the most promise in that it is a beam-type specimen, which may be rather simple to analyze, it has a high compliance that can be measured experimentally, and the specimen is easily manufactured. Therefore, the SCB specimen has been utilized for characterizing the mode III fracture behavior of the adhesive studied herein.

2.6.1: Analysis Techniques

Given the ability to readily measure the compliance of the SCB specimen experimentally, an experimental compliance analysis technique is often utilized for calculating the mode III strain energy release rate, $\mathcal{G}_{\mathrm{IIIc}}$ [74]:

$$\mathcal{G}_{IIIc} = \frac{nP\Delta}{2ba} \tag{2.24}$$

where P is the applied load, Δ is the opening displacement, b is the specimen width, a is the crack length, and n is the compliance calibration factor, or the slope of the linear curve fit for the $\log(C)$ versus $\log(a)$ plot, where C is the measured compliance. It should be noted that for $n = 3$, the resulting equation is that predicted using beam theory.

An alternative method, one that has been shown to provide more satisfactory results for this particular specimen geometry, is the area method [74-75]. This method can also be thought of as an energy method, as it can be said that the area under the load-displacement curve is equal to the energy lost during crack propagation. As such, the mode III strain energy release rate, $\mathcal{G}_{\mathrm{IIIc}}$, can be calculated using this method [74]:

$$\mathcal{G}_{IIIc} = \frac{1}{2b}\left[P_i\left(\frac{d\Delta}{da}\right)_i - \Delta_i\left(\frac{dP}{da_i}\right)\right] \tag{2.25}$$

where the quantities $d\Delta$, da, and dP are the end displacement, crack length, and load increments, respectively, from the i to the $i+1$ data.

2.7: Conclusion

The various specimen geometries covered in this chapter can all be used in determining the fracture behavior of adhesively bonded joints, thus resulting in the eventual development of fracture envelopes to be utilized later in the design process. Some test configurations have proven to be more successful than others, yet only two of the specimen geometries discussed, the DCB for mode I and the MMB for mixed-mode I/II, have achieved standardization. Additionally, only one of the two standardized specimens, the DCB, lends itself readily to impact loading conditions. Therefore, much more research is needed to develop standardized test methods that can be used for both slow and high-rate tests to help further the understanding behind the fracture of adhesive joints.

Based on the review of the various test methods, combined with available test equipment and the need to utilize simplistic specimen geometries for both quasi-static

and dynamic loading conditions, the DCB, ADCB, SLB, ELS, and SCB specimens were chosen for the mode I, mixed-mode I/II, mode II, and mode III fracture characterization of the adhesively bonded composite joints studied herein. Standard beam theory analysis techniques, often with the inclusion of various correction factors, have been chosen for the data analysis of the various tests given their proven reliability and repeatability in previously conducted experiments.

References

1. ASTM D-3433, "Standard Test Method for Fracture Strength in Cleavage of Adhesives in Bonded Metal Joints", in *Annual Book of ASTM Standards*, 2003, ASTM: West Conshohocken, PA.
2. ASTM D-6671, "Standard Test Method for Mixed Mode I-Mode II Interlaminar Fracture Toughness of Unidirectional Fiber Reinforced Polymer Matrix Composites", in *Annual Book of ASTM Standards*, 2004, ASTM: West Conshohocken, PA.
3. Gledhill, R. A. and Kinloch, A. J., "Mechanics of Crack Growth in Epoxide Resins", *Polymer Engineering and Science*, **19** (2), 1979, pp. 82-88.
4. Macon, D. J. and Anderson, G. L., "Kinetic Energy Corrections for Slip-Stick Behavior in Brittle Adhesives", *Journal of Applied Polymer Science*, **86**, 2002, pp. 1821-1828.
5. Yamini, S. and Young, R. J., "Stability of Crack propagation in Epoxy Resins", *Journal of Materials Science*, **15**, 1980, pp. 1823-1831.
6. Kinloch, A. J. and Williams, J. G., "Crack Blunting Mechanisms in Polymers", *Journal of Materials Science*, **15**, 1980, pp. 987-996.
7. Ashcroft, I. A., Hughes, D. J., and Shaw, S. J., "Mode I Fracture of Epoxy Bonded Composite Joints: Quasi-Static Loading", *International Journal of Adhesion and Adhesives*, **21**, 2001, pp. 87-99.

8. Simón, J. C., Johnson, E., and Dillard, D. A., "Characterizing Dynamic Fracture Behavior of Adhesive Joints Under Quasi-Static and Impact Loading", *Journal of ASTM International*, **2** (7), 2005, pp. 1-19.
9. Dillard, D. A., Jacob, G. C., Pohlit, D. J., and Starbuck, J. M., "On the Use of a Driven Wedge Test to Acquire Dynamic Fracture Energies of Bonded Beam Specimens: Part I – Motivation and Experimental Implementation", In review (*Journal of Adhesion*).
10. Kinloch, A. J., *Adhesion and Adhesives: Science and Technology*, Chapman and Hall: London, 1987.
11. Williams, J. G., *Fracture Mechanics of Polymers*, Chichester: Ellis Horwood Limited, 1984.
12. Anderson, T. L., *Fracture Mechanics: Fundamentals and Applications*, CRC Press: Boca Raton, 1991.
13. Maugis, D. and Barquins, M., "Fracture Mechanics and the Adherence of Viscoelastic Bodies", *Journal of Physics. D, Applied Physics*, **11**, 1978, pp. 1989-2023.
14. Maugis, D., "Subcritical Crack Growth, Surface Energy, Fracture Toughness, Stick-Slip and Embrittlement – A Review", *Journal of Materials Science*, **20**, 1985, pp. 3041-3073.
15. Schroeder, J. A., "Fracture Toughness and Molecular Structure of Unfilled Epoxy Adhesives", *Journal of Materials Science*, **23** (9), pp. 3073-3082.

16. Atkins, A. G., Lee, C. S., and Caddell, R. M., "Time-Temperature Dependent Fracture Toughness of PMMA", *Journal of Materials Science*, **10** (8), pp. 1381-1393.

17. Hine, P. J., Duckett, R. A., and Ward, I. M., "A Double-Torsion Study of the Fracture of Polyethersulphone", *Journal of Materials Science*, **19** (11), pp. 3796-3805.

18. Dillard, D. A., McDaniels, P. R., and Hinkley, J. A., "The Use of an Eccentric Compressive Load to Aid in Precracking Single Edge Notch Bend Specimens", *Journal of Materials Science Letters*, **12** (16), pp. 1258-1260.

19. Blackman, B. R. K., Dear, J. P., Kinloch, A. J., MacGillivray, H., Wang, Y., Williams, J. G., and Yayla, P., "The Failure of Fibre Composites and Adhesively Bonded Fibre Composites Under High Rates of Test: Part I - Mode I Loading - Experimental Studies", *Journal of Materials Science*, **30**, 1995, pp. 5885-5900.

20. Blackman, B. R. K., Kinloch, A. J., Taylor, A. C., and Wang, Y., "The Impact Wedge-Peel Performance of Structural Adhesives", *Journal of Materials Science*, **35**, 2000, pp. 1867-1884.

21. Blackman, B. R. K., Dear, J. P., Kinloch, A. J., MacGillivray, H., Wang, Y., Williams, J. G., and Yayla, P., "The Failure of Fibre Composites and Adhesively Bonded Fibre Composites Under High Rates of Test: Part III – Mixed-Mode I/II and Mode II Loadings", *Journal of Materials Science*, **31**, 1996, pp. 4467-4477.

22. Xu, S. Y. and Dillard, D. A., "Determining the Impact Resistance of Electrically Conductive Adhesives Using a Falling Wedge Test", *IEEE Transactions on Components and Packaging Technologies*, **26** (3), 2003, pp. 554-562.

23. Kinloch, A. J., Shaw, S. J., Tod, D. A., and Hunston, D. L., "Deformation and Fracture Behavior of a Rubber-Toughened Epoxy: 1. Microstructure and Fracture Studies", *Polymer*, **24** (10), 1983, pp. 1341-1354.

24. Kinloch, A. J., Shaw, S. J., and Hunston, D. L., "Deformation and Fracture Behavior of a Rubber-Toughened Epoxy: 2. Failure Criteria", *Polymer*, **24** (10), 1983, pp. 1355-1363.

25. Huang, Y. and Kinloch, A. J., "The Use of Time-Temperature Superpositioning in Studying the Fracture Properties of Rubber-Toughened Epoxy Polymers", *Journal of Adhesion*, **41**, 1993, pp. 5-22.

26. Kinloch, A. J. and Shaw, S. J., "The Fracture Resistance of a Toughened Epoxy Adhesive", *Journal of Adhesion*, **12**, 1981, pp. 59-77.

27. Yamini, S. and Young, R. J., "The Mechanical Properties of Epoxy Resins Part II: Effect of Plastic Deformation Upon Crack Propagation", *Journal of Materials Science*, **15**, 1980, pp. 1823-1831.

28. Obreimoff, J. W., "The Splitting Strength of Mica", in *Proceedings of the Royal Society of London*, **127A**, 1930, pp. 290-297.

29. Ripling, E. J., Mostovoy, S., and Patrick, R. L., "Application of Fracture Mechanics to Adhesive Joints", *Adhesion*, *ASTM STP 360*, American Society for Testing and Materials, Philadelphia, 1964, pp. 5-19.

30. Ripling, E. J., Mostovoy, S., and Patrick, R. L., "Measuring Fracture Toughness of Adhesive Joints, *Materials Research & Standards*, **4**, 1964, pp. 129-134.

31. Mostovoy, S., Crosley, P. B., and Ripling, E. J., "Use of Crack-Line Loaded Specimens for Measuring Plane-Strain Fracture Toughness", *Journal of Materials*, **2**, 1967, pp. 661-681.

32. BSI. *BS-7991*: "Determination of the Mode I Adhesive Fracture Energy, G_{Ic}, of Structural Adhesives Using the Double Cantilever Beam (DCB) and Tapered Double Cantilever Beam (TDCB) Specimens", 2001.

33. Blackman, B. R. K., Hadavinia, H., Kinloch, A. J., Paraschi, M., and Williams, J. G., "The Calculation of Adhesive Fracture Energies in Mode I: Revisiting the Tapered Double Cantilever Beam (TDCB) Test", *Engineering Fracture Mechanics*, **70**, 2003, pp. 233-248.

34. Irwin, G. R. and Kies, J. A., "Critical Energy Rate Analysis of Fracture Strength", *Welding Journal*, **33**, 1954, pp. 193-198.

35. Williams, J. G., "Large Displacement and End Block Effects in the 'DCB' Interlaminar Test in Modes I and II", *Journal of Composite Materials*, **21**, 1987, pp. 330-347.

36. Hashemi, S., Kinloch, A. J., and Williams, J. G., "The Analysis of Interlaminar Fracture in Uniaxial Fibre-Polymer Composites", in *Proceedings of the Royal Society of London. Series A, Mathematical and Physical Sciences*, **427** (1872), 1990, pp. 173-199.

37. Blackman, B. R. K., Kinloch, A. J., Wang, Y., and Williams, J. G., "The Failure of Fibre Composites and Adhesively Bonded Fibre Composites Under High Rates of Test: Part II - Mode I Loading - Dynamic Effects", *Journal of Materials Science*, **31**, 1996, pp. 4451-4466.

38. Teo, W. S., Blackman, B. R. K., Kinloch, A. J., and Rodriguez-Sanchez, F. S., "The Analysis of Fracture Mechanics Data from High-Rate Tests" in *Proceedings of the 30th Annual Meeting of The Adhesion Society*, 2007, Tampa, Florida, USA.
39. Davidson, B. R. and Sundararaman, V., "A Single Leg Bending Test for Interfacial Fracture Toughness Determination", *International Journal of Fracture*, **78**, 1996, pp. 193-210.
40. Kinloch, A. J., Wang, Y., Williams, J. G., and Yayla, P., "The Mixed-Mode Delamination of Fibre Composite Materials", *Composites Science and Technology*, **47**, 1993, pp. 225-237.
41. Choi, N. S., Kinloch, A. J., and Williams, J. G., "Delamination Fracture of Multidirectional Carbon-Fiber/Epoxy Composites Under Mode I, Mode II, and Mixed-Mode I/II Loading", *Journal of Composite Materials*, **33**, 1999, pp. 73-100.
42. Xiao, F., Hui, C. Y., and Kramer, E. J., "Analysis of a Mixed Mode Fracture Specimen: The Asymmetric Double Cantilever Beam", *Journal of Materials Science*, **28**, 1993, pp. 5620-5629.
43. Sundararaman, V. and Davidson, B. D., "An Unsymmetric Double Cantilever Beam Test for Interfacial Fracture Toughness Determination", *International Journal of Solids and Structures*, **34** (7), 1997, pp. 799-817.
44. Ducept, F., Gamby, D., and Davies, P., "A Mixed-Mode Failure Criterion Derived from Tests on Symmetric and Asymmetric Specimens", *Composites Science and Technology*, **59**, 1999, pp. 609-619.

45. Guo, Y.-J. and Weitsman, Y. J., "A Modified DCB Specimen to Determine Mixed Mode Fracture Toughness of Adhesives", *Engineering Fracture Mechanics*, **68**, 2001, pp. 1647-1668.

46. Reeder, J. R. and Crews, J. H. Jr., "The Mixed-Mode Bending Method for Delamination Testing", *AIAA Journal*, **28** (7), 1990, pp. 1270-1276.

47. Bhashyam, S. and Davidson, B. D., "An Evaluation of Data Reduction Methods for the Mixed Mode Bending Test", *AIAA*, 1996, pp. 886-896.

48. Reeder, J. R. and Crews, J. H. Jr., "Redesign of the Mixed-Mode Bending Delamination Test to Reduce Nonlinear Effects", *Journal of Composites Technology and Research*, **14** (1), 1992, pp. 12-19.

49. Charalambides, M., Kinloch, A. J., Wang, Y., and Williams, J. G., "On the Analysis of Mixed-Mode Failure", *International Journal of Fracture*, **54**, 1992, pp. 269-291.

50. Creton, C., Kramer, E. J., Hui, C.-Y., and Brown, H. R., "Failure Mechanisms of Polymer Interfaces Reinforced with Block Copolymers", Macromolecules, **25** (12), 1992, pp. 3075-3088.

51. Kanninen, M. F., "An Augmented Double Cantilever Beam Model for Studying Crack Propagation and Arrest", *International Journal of Fracture*, **9** (1), 1973, pp. 83-92.

52. Williams, J. G., "On Calculation of the Energy Release Rate for Cracked Laminates", *International Journal of Fracture*, **36**, 1988, pp. 101-119.

53. Ducept, F., Gamby, D., and Davies, P., "A Mixed-Mode Failure Criterion Derived from Tests on Symmetric and Asymmetric Specimens", *Composites Science and Technology*, **59**, 1999, pp. 609-619.

54. Hutchinson, J. W. and Suo, Z., "Mixed Mode Cracking in Layered Materials", *Advances in Applied Mechanics*, **29**, 1992, pp. 64-122.

55. Davies, P., Sims, G. D., Blackman, B. R. K., Brunner, A. J., Kageyama, K., Hojo, M., Tanaka, K., Murri, G., Rousseau, C., Gieseke, B., and Martin, R. H., "Comparison of Test Configurations for Determination of Mode II Interlaminar Fracture Toughness Results from International Collaborative Test Programme", *Plastics, Rubber and Composites*, **28** (9), 1999, pp. 432-437.

56. JIS. *JIS 7086*: "Testing Methods for Interlaminar Fracture Toughness of Carbon Fiber Reinforced Plastics", 1993.

57. AECMA. *AECMA Aerospace Series, Carbon Fibre Reinforced Plastics*: "Determination of Interlaminar Fracture Toughness Energy Mode I - $\mathcal{G}_{Ic}$ (pr EN6033) and Mode II - $\mathcal{G}_{IIc}$ (pr EN6034)", 1995.

58. Barrett, J. D. and Foschi, R. O., "Mode II Stress-Intensity Factors for Cracked Wood Beams", *Engineering Fracture Mechanics*, **9** (2), 1977, pp. 371-378.

59. Blackman, B. R. K., Brunner, A. J., and Williams, J. G., "Mode II Fracture Testing of Composites: A New Look at an Old Problem", *Engineering Fracture Mechanics*, **73**, 2006, pp. 2443-2455.

60. Martin, R. H. and Davidson, B. D., "Mode II Fracture Toughness Evaluation Using Four Point Bend, End Notched Flexure Test", *Plastics, Rubber and Composites*, **28** (8), 1999, pp. 401-406.

61. Schuecker, C. and Davidson B. D., "Effect of Friction on the Perceived Mode II Delamination Toughness From Three and Four Point Bend End-Notched Flexure Tests", in *Composites Structures Theory and Practice*, 2004, ASTM: West Conshohocken, PA, pp. 334-344.

62. Davies, P., "Influence of ENF Specimen Geometry and Friction on the Mode II Delamination Resistance of Carbon/PEEK", *Journal of Thermoplastic Composite Materials*, **10** (4), 1997, pp. 353-361.

63. Vanderkley, P. S., "Mode I-Mode II Delamination Fracture Toughness of a Unidirectional Graphite/Epoxy Composite", Master's Thesis, Texas A&M University, College Station, TX, 1981.

64. Russell, A. J. and Street, K. N., "The Effect of Matrix Toughness on Delamination: Static and Fatigue Fracture Under Mode II Shear Loading of Graphite Fiber Composites", in *Toughened Composites*, *ASTM STP-937*, 1987, pp. 275-294.

65. Blackman, B. R. K., Kinloch, A. J., and Paraschi, M., "The Determination of the Mode II Adhesive Fracture Resistance, G_{IIc}, of Structural Adhesive Joints: An Effective Crack Length Approach", *Engineering Fracture Mechanics*, **72**, 2005, pp. 877-897.

66. Wang, Y. and Williams, J. G., "Corrections for Mode II Fracture Toughness Specimens of Composites Materials", *Composites Science and Technology*, **43**, 1992, pp. 251-256.

67. Wang, Y. and Vu-Khanh, T., "Use of End-Loaded-Split (ELS) Test to Study Stable Fracture Behavior of Composites Under Mode II Loading", *Composite Structures*, **36**, 1996, pp. 71-79.

68. Becht, G. and Gillespie, J. W. Jr., "Design and Analysis of the Crack Rail Shear Specimen for Mode III Interlaminar Fracture", *Composites Science and Technology*, **31**, 1988, pp. 143-157.

69. Becht, G. and Gillespie, J. W. Jr., "Numerical and Experimental Evaluation of the Mode III Interlaminar Fracture Toughness of Composite Materials", *Polymer Composites*, **10** (5), 1989, pp. 293-304.

70. Robinson, P. and Song, D. Q., "The Development of an Improved Mode III Delamination Test for Composites", Composites Science and Technology, 52, 1994, pp. 217-233.

71. Lee, S. M., "An Edge Crack Torsion Method for Mode III Delamination Fracture Testing", *Journal of Composites Technology and Research*, **15** (3), 1993, pp. 193-201.

72. Zhao, D. and Wang, Y., "Mode III Fracture Behavior of Laminated Composite with Edge Crack in Torsion", *Theoretical and Applied Fracture Mechanics*, **29**, 1998, pp. 109-123.

73. Li, J., Ming Lee, S., Lee, E. W., and O'Brien, T. K., "Evaluation of the Edge Crack Torsion (ECT) Test for Mode III Interlaminar Fracture Toughness of Laminated Composites", *Journal of Composites Technology & Research*, **19** (3), 1997, pp. 174-183.

74. Donaldson, S. L., "Mode III Interlaminar Fracture Characterization of Composite Materials", *Composites Science and Technology*, **32**, 1988, pp. 225-249.

75. Donaldson, S. L., Mall, S., and Lingg, C., "The Split Cantilever Beam Test for Characterizing Mode III Interlaminar Fracture Toughness", *Journal of Composites Technology & Research*, **13** (1), 1991, pp. 41-47.

76. Martin, R. H., "Evaluation of the Split Cantilever Beam for Mode III Delamination Testing", in *Composite Materials: Fatigue and Fracture (Third Volume)*, *ASTM STP 1110*, 1991, pp. 243-266.

77. Sharif, F., Kortschot, M. T., and Martin, R. H., "Mode III Delamination Using a Split Cantilever Beam", in *Composite Materials: Fatigue and Fracture (Fifth Volume)*, *ASTM STP 1230*, 1995, pp. 85-99.

Chapter 3. Specimen Preparation & Test Methods

This section will provide a brief explanation of the materials used for this study, as well as a detailed account of the specimen fabrication process. The specimen preparation methods utilized in this study will also be discussed. Additionally, the methods of test will be discussed regarding the various modes of fracture studied for the purpose of this thesis. These methods will include mode I, mixed-mode I/II, mode II, and mode III fracture characterization.

3.1: Materials

Materials were chosen for this study based on the needs of today's automotive industry for continuing innovations with regard to automotive light-weighting. Standard bonded beam specimens were used in order to facilitate both the manufacturing and testing processes. All specimens were configured in such a way as to simulate the modes of fracture possible within automotive structures.

The adherend material, MTM49/CF0501, was comprised of a plain weave balanced carbon fabric (T300B-40B) pre-impregnated with an epoxy matrix system. This material was provided by the Advanced Composites Group (Tulsa, OK), and subsequent 625x625mm fabricated panels were provided by Pacific Composites, Inc. (San Clemente, CA) in various material orientation configurations as shown in Table 3.1.

Table 3.1. Composite adherend material lay-up configurations.

Ply Count	Thickness (mm)	Orientation
11	2.8	$((0/90,\pm45)_4,(0/90)_3)_T$
20	4.6	$((0/90,\pm45)_5)_S$
36	8.5	$((0/90,\pm45)_9)_S$

These larger panels were later quartered to a size of 300x300mm in order to facilitate the bonding process. The adhesive chosen for the purpose of this thesis was PL-731-SI, a commercially available two-part epoxy system provided by Sovereign Specialty Chemicals, Inc. (Buffalo, NY). All adhesive was supplied in the form of 400mL cartridges, with an resin-to-hardener dispense ratio of 4:1.

3.2: Specimen Fabrication

All bonded composite specimens used for this study were prepared by Ronny Lomax of the Polymer Matrix Composites Group at Oak Ridge National Laboratory. Each composite plate was thoroughly cleaned using a combination of ethanol alcohol and acetone in an attempt to remove any unwanted contaminants, especially remnants of release agents left over from the initial panel fabrication process. A 50mm long piece of Teflon film was then applied to one end of each composite plate half in order to incorporate a starter crack into each bonded specimen. Spring-steel shims were bonded to each side of the composite plates using a standard cyanoacrylate in order to control the eventual bond-line thickness of 0.5mm, as illustrated in Figure 3.1.

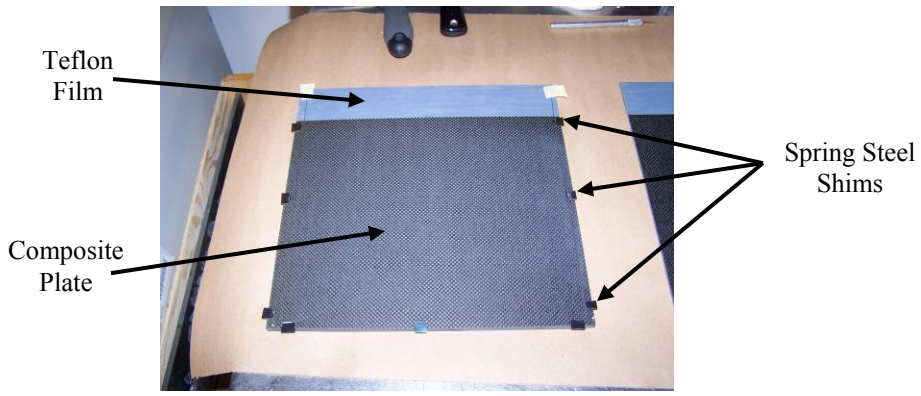

Figure 3.1. Spring-steel shim placement during bonded composite plate fabrication.

Prior to dispensing, the adhesive was centrifuged in order to remove air pockets within the material cartridge in an attempt to minimize the number of voids present in the bonded specimens. The adhesive was then dispensed in a 4:1 ratio using a MixPac (MixPac Systems AG, Switzerland) DP 200-70 pneumatic dispensing gun. A 200mm static mixing tube was used to combine the resin and hardener in order to ensure that an adequate mix of the two adhesive components was applied to each composite plate. Additionally, the adhesive was later spread across each composite plate half using a standard 12 inch drywall trowel in order to ensure an even spread of adhesive across the bonding face, as shown in Figures 3.2 a and b.

(a) ***(b)***

Figure 3.2. Adhesive dispensing and spreading process during composite plate bonding process.

The composite plate halves were then sandwiched together and placed in a platen press for curing. The plates were ramped up to 127°C over the course of one hour, and held at 127°C for the duration of one hour in order to ensure full cure. The bonded plates were then allowed to air cool prior to removing them from the press.

3.3: Specimen Preparation

To facilitate the specimen manufacturing process, all specimens were fabricated in a bonded plate configuration, as previously mentioned, from which the eventual beam specimens were cut. The bonded plates were first squared off according to the weave pattern of the composite adherend material in order to develop a primary cutting edge. The bonded plates were then cut into 25.4mm wide specimens using a Felker 41AR wet saw (Olathe, KS) fitted with a diamond blade using water cooling.

A pre-cracking process was also incorporated for all bonded specimens to develop a sharp crack tip prior to the initial loading procedure. The end of each bonded specimen not containing the Teflon film insert was clamped in a table-top vise. A C-clamp was placed at a point that was about 55mm from the load application point for all mode I DCB, mixed-mode I/II ADCB, and mode III SCB specimens in order to facilitate crack arrest during the pre-cracking procedure. Additionally, a C-clamp was placed at a point that was roughly 60% of the total specimen free length for all mixed-mode I/II SLB and mode II ELS specimens for this same purpose [1-5]. A stainless-steel wedge was then lightly hammered down into the bonded joint region, allowing the composite adherends to separate up to the clamped region of the specimen, thus developing a sharp crack tip suitable for testing. Figure 3.3 better illustrates this procedure.

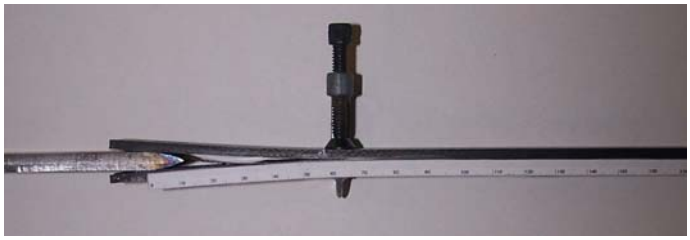

Figure 3.3. Specimen pre-cracking procedure.

Each individual bonded specimen was then drilled with size 8-32 holes using a drilling template manufactured specifically for this purpose. These holes were then tapped to allow for the attachment of mechanically fastened steel loading blocks to be used for most of the fracture testing discussed in this thesis. Although uncommon to thread composite materials, the loads observed during all testing were sufficiently small to allow this approach to work well. The use of a drilling template allowed for a highly accurate and repeatable drilling procedure to be used for each of the bonded specimens. A paper ruler was later attached to each specimen in order to aid in visual crack length measurements during static tests. For all dynamic tests, one side of each bonded composite specimen was painted white using water-based typewriter correction fluid, onto which 5mm marks were drawn with a fine-point pen to provide a visual reference of measurement during all high-rate tests. Typical prepared bonded composite specimens are illustrated in Figure 3.4.

(*a*)

(*b*)

Figure 3.4. Typical bonded composite specimen configurations prior to testing: (*a*) static and (*b*) dynamic.

3.4: Static Test Setup

All static tests were conducted using an Instron (Norwood, MA) 4500 series screw-driven test frame outfitted with a 10kN strain-gage load cell. Load-displacement data was collected using software developed in-house using National Instruments LabVIEW™ (Austin, TX) software. All data was later analyzed using spreadsheets developed by the author that allowed for various types of analyses for each specimen configuration. Load was applied to each specimen through the use of mechanically fastened steel loading blocks. All static tests were conducted under a controlled displacement rate of 1.67×10^{-5} m/s.

Crack lengths were measured visually using the attached paper rulers, as previously mentioned. Upon initial crack propagation, each specimen was unloaded in order to determine whether or not plastic deformation had occurred within the adherend material. Although observations were made in order to determine whether or not plastic deformation had occurred during each test, no such deformation was visible for any of the test specimen geometries in question. Due to the unstable nature of the adhesive in

question, the recommended loading-unloading procedure described in the ASTM standard [6] was not followed for the purpose of this thesis. Instead, the British standard [7] was followed in the interest of time, as typical static DCB tests could last approximately 90 minutes under the applied static loading rate.

3.4.1: Double Cantilever Beam

The testing protocol developed by Kinloch *et al.* [7] was adopted for the purpose of conducting mode I fracture tests. Figure 3.5 shows the DCB specimen configuration.

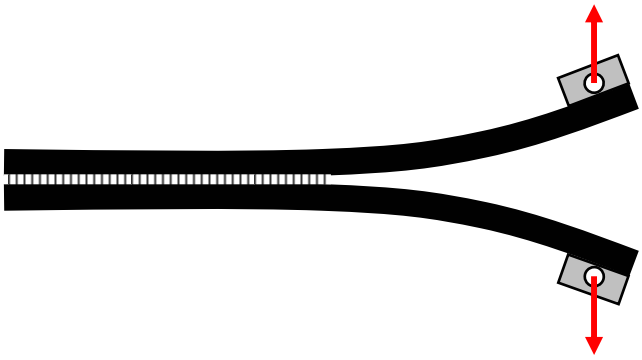

Figure 3.5. Double cantilever beam (DCB) specimen configuration.

Several analysis methods are described within [7], which provides a more thorough characterization of the specimen geometry. Using measured load, displacement, and crack length data, in combination with material properties and specimen geometric parameters, the critical mode I strain energy release rate, G_{Ic}, could be calculated for all specimens using the methods described within the testing protocol.

3.4.2: Asymmetric Double Cantilever Beam

The asymmetric double cantilever beam (ADCB) geometry studied for the purpose of this thesis consisted of one of two possible specimen configurations: 11x20 or 11x36 bonded specimens. Regarding the asymmetrically bonded specimens utilized in

this study, the 11x20 specimens consisted of an 11-ply adherend bonded to a 20-ply adherend resulting in a 7.9mm thick test specimen, which includes the 0.5mm bond-line thickness. Similarly, the 11x36 specimens consisted of an 11-ply adherend bonded to a 36-ply adherend resulting in a 11.85mm thick test specimen, also including the bond-line thickness. These specimens were loaded in the same configuration as a standard DCB specimen, using the same mechanically fastened steel loading blocks, as illustrated in Figure 3.6. All data – load, displacement, and crack length – were captured using the same test equipment utilized in the DCB tests. Additionally, multiple analysis methods were utilized for comparison purposes, in order to quantify variations in results amongst existing theories [8-12].

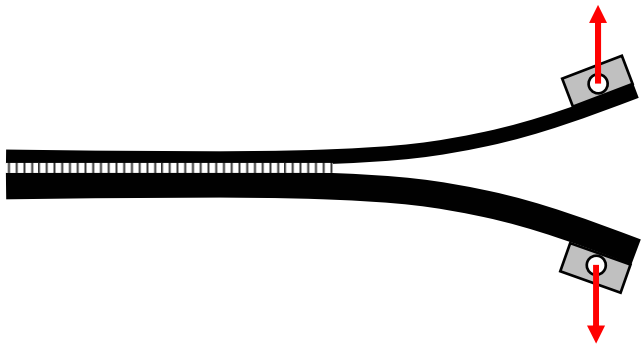

Figure 3.6. Asymmetric double cantilever beam (ADCB) specimen configuration.

3.4.3: Single Leg Bend

A test fixture was developed in-house [13] for the mixed-mode I/II testing of the single leg bend (SLB) specimen geometry in order to achieve a constant mode-mix ratio, $\mathcal{G}_{Ic}/\mathcal{G}_{IIc}$, of 1.33. Additionally, the developed fixture can also be used for alternative loading modes, such as asymmetric specimens where the mode mixity ratio is not 1.33, although such specimens were not tested for the purpose of this study. The fixture

consisted of a precision milled steel shaft that was allowed to slide laterally through a fixed mounted linear ball bearing. This free lateral movement allowed the path of applied loading to remain in alignment with the fixed base of the test fixture while the specimen moment arm decreased under large displacements. The specimen was mounted on the far end of the shaft using a mounting block/clamping plate arrangement. Figure 3.7 illustrates the SLB test fixture used for the studies conducted for the purpose of this thesis. All components and materials are commercially available and were purchased from McMaster-Carr (Atlanta, GA). The load was applied to the specimen via one mechanically fastened steel loading block attached to the bottom beam arm, as illustrated in Figure 3.7.

Measured load, displacement, and crack length data, in combination with material properties and specimen geometric parameters, were used to calculate the critical mixed-mode I/II strain energy release rate, $\mathcal{G}_{I/IIc}$, which was calculated using load, displacement, and work-based analysis methods for comparison purposes [1-5].

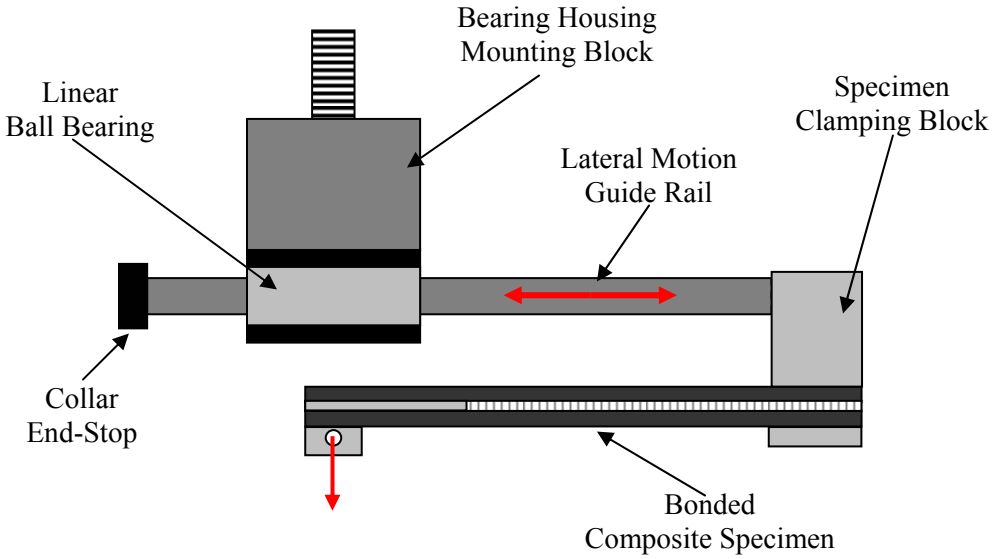

(*a*)

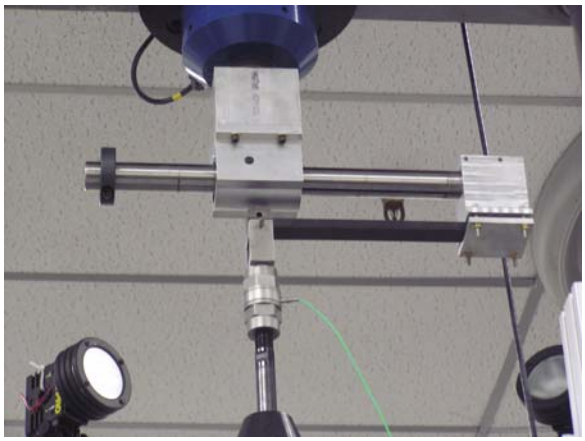

(*b*)

Figure 3.7. Single leg bend test fixture: (*a*) schematic and (*b*) actual photo.

3.4.4: End-Loaded Split

The same test fixture developed for the mixed-mode I/II SLB testing was used for the mode II end-loaded split (ELS) testing as well [1,3-5,14-15]. This was due to the fact that the same free lateral motion of the specimen was necessary as the effective specimen moment arm decreased with increasing displacement. The only difference among the

two tests is that, instead of pulling the bottom arm like in the SLB test, the load was applied through a mechanically fastened steel loading block attached to the top arm instead. Thus, both beam arms were pulled in the same direction creating a pure mode II fracture condition. This concept is better illustrated in Figure 3.8.

Finally, measured load, displacement, and crack length data, in combination with material properties and specimen geometric parameters, were used to calculate the critical mode II strain energy release rate, $\mathcal{G}_{IIc}$. However, it should be noted that only one data point was obtained for each ELS specimen; following this initiation, the crack propagation jumped through the adhesive layer and resulted in composite adherend failure.

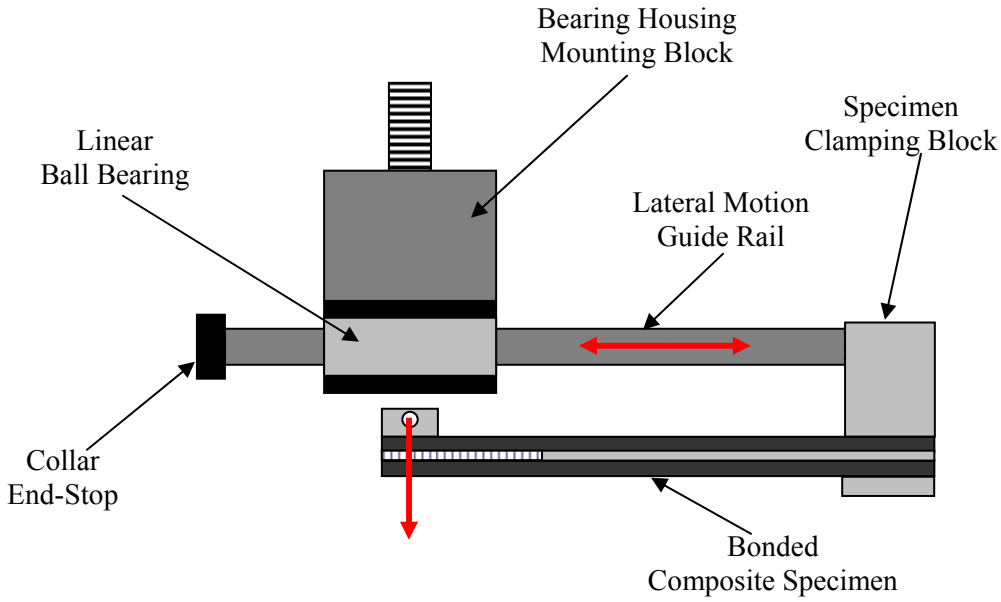

Figure 3.8. End-loaded split (ELS) specimen configuration.

3.4.5: Split Cantilever Beam

Very little experimental work has been attempted for characterizing the mode III fracture behavior of materials, and even less has proved successful. Although several

proposed test geometries exist [16-18], not one has been adopted as a standard test method. For the purpose of this thesis, the split cantilever beam (SCB) specimen was chosen to characterize the mode III fracture behavior of the bonded composite joints in question. This geometry was chosen due to its simplicity, which aided in timely specimen fabrication and testing implementation. A simple loading apparatus was manufactured in-house based on previous work by Donaldson *et al.* [17]. Due to the specimen configuration, this apparatus was necessary in order to keep the applied loading arms in alignment throughout the testing procedure. The SCB test specimen configuration with corresponding loading apparatus is illustrated in Figure 3.9.

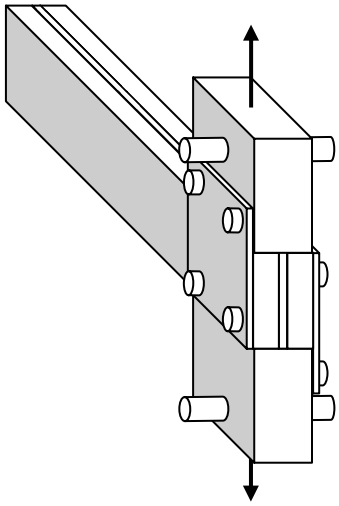

Figure 3.9. Split cantilever beam (SCB) specimen configuration.

3.5: Dynamic Test Setup

All dynamic fracture testing discussed within this thesis was conducted at the Oak Ridge National Laboratory (ORNL – Oak Ridge, TN). The experiments were conducted using a custom made MTS (Eden Prairie, MN) servo-hydraulic test machine outfitted with either a 2.2kN or 40kN Kistler (Winterthur, Switzerland) piezoelectric load cell depending on the type of test to be conducted (i.e. the 2.2kN load cell was used only for

mode I DCB testing because the measured loads were sufficiently low). This machine was designed by staff members at ORNL in collaboration with employees of MTS. Capable of achieving test velocities up to 18m/s, this machine makes use of a robust power-plant that includes two 190 liter accumulators and a 25.2 liter/s main servo valve. Figure 3.10 provides images of the 18 m/s testing machine.

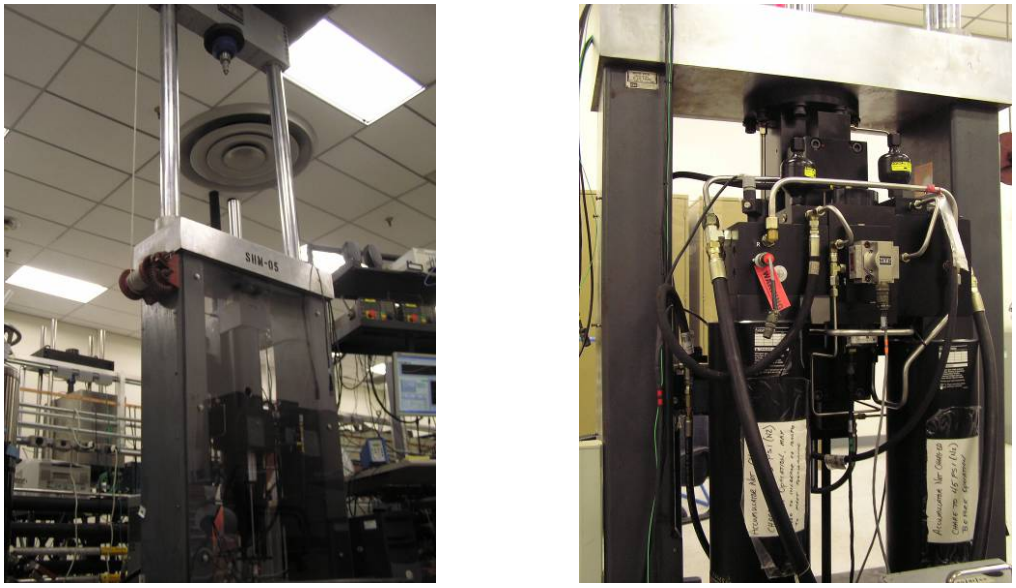

Figure 3.10. Custom designed MTS test machine capable of achieving a maximum test velocity of 18m/s: frontal view of test machine (left) and machine power-plant (right).

All data acquisition software for this machine was developed in-house by Don Erdman at ORNL using National Instruments (Austin, TX) LabVIEW software. A lightweight slack adaptor was developed from standard off-the-shelf components, such as a linear ball bearing with an aluminum pillow-block housing, a stainless steel shaft, and aluminum stock. The slack adaptor was implemented to allow the test machine to reach the maximum user specified velocity for each test prior to applying any load to the test specimens. A schematic of the slack adaptor setup used for the dynamic DCB tests is

shown in Figure 3.11. Slight variations were made to the overall set-up depicted in Figure 3.11 for the mixed-mode I/II and mode II tests; however, the same general configuration remained the same. It should also be noted that Figure 3.11 is not drawn to scale in order to more clearly illustrate some of the smaller components that make up the load train of the dynamic testing set-up.

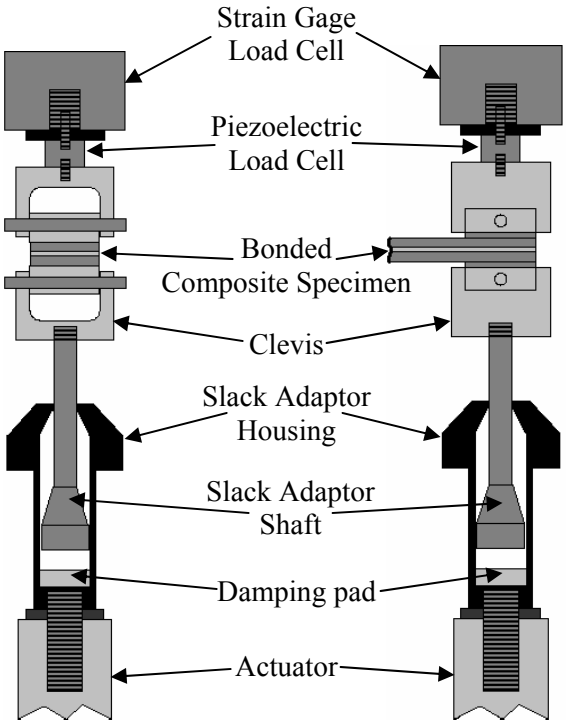

Figure 3.11. Slack adaptor set-up used for DCB high-rate testing.

Dynamic fracture tests on the same system of materials were also conducted on a separate hydraulic test machine in a coordinated study [19]. Although the test equipment and associated slack adaptor were different, it will be shown later in the Results chapter of this thesis that data obtained in both cases agree quite well.

In conjunction with the testing machines, a high-speed imaging system was used for monitoring crack propagation and essentially for determining initiation and arrest

crack lengths for all tests. A Photron (San Diego, CA) Ultima APX-RS high-speed camera purchased from Motion Capture Technologies (Valdese, NC) provided the ability to capture full 1024x1024 pixel resolution at up to 3000 frames per second with a two second record duration. Additionally, 512x512 pixel resolution at up to 10,000 frames per second was available, as well as a top recording speed of 250,000 frames per second with 128x16 pixel resolution, although such a high frame rate was never utilized for the purpose of this thesis.

3.5.1: Double Cantilever Beam

Dynamic double cantilever beam specimens were mounted in the hydraulic load frame and subjected to applied loads in the same manner as described in the static test setup section of this thesis, only under much higher test velocities up to 10m/s. As previously mentioned, all dynamic DCB crack length data was collected visually using the high-speed imaging system. Settings of 1500, 3000, and 9000 frames per second were utilized for test rates of 0.01, 0.1, and 1m/s respectively, while a setting of 12000 frames per second was utilized for the limited number of tests conducted at 10m/s. Load, displacement, and time data were captured from the load cell via the load frame data acquisition software.

According to the literature, there are several complications associated with high-rate fracture testing data acquisition. It has been shown that relevant load data can not be obtained using a standard strain gage load cell due to reflected stress wave propagation within the adherend materials, which often result in large noise induction into the captured load signal, thus resulting in unusable data [20-21]. By using a piezoelectric

load cell instead, a much higher frequency response is obtained when compared with traditional strain gage load cells, which allows for a more effective means for measuring dynamic loads. It has also been suggested that the same theory should apply for the measured displacement data due to the vibrations present within the test specimens associated with dynamic testing. However, for the purpose of this thesis, it was determined that the measurements obtained from the load frame actuator displacement were adequate due to the large displacements that were observed for all mode I test specimen configurations. Furthermore, although the presence of noise did result in a more tedious analysis approach, the measured loads were also incorporated into the analysis due to the high frequency capabilities of the utilized piezoelectric load cells. Therefore, a work-based analysis was employed when calculating the mode I critical strain energy release rate, G_{Ic}, thru the use of directly measured load-displacement data.

3.5.2: Driven Wedge

In combination with the standard DCB test configuration, an alternative specimen geometry has been analyzed to provide a correlation amongst various experimental configurations to more accurately characterize the mode I fracture behavior of the adhesive studied herein. An alternative bonded joint configuration was analyzed experimentally in a related study in the form of a driven wedge test specimen [22], while numerical analysis on this specimen configuration was conducted to obtain fracture energy corrections as part of this thesis.

Using the driven wedge specimen configuration, the crack faces of a bonded joint are in contact with a wedge that is driven along the length of the specimen, thus splitting

the specimen apart in a mode I configuration [22]. This technique has proven to be especially useful for characterizing material systems exhibiting pronounced stick-slip fracture behavior. A schematic of the test configuration is illustrated in Figure 3.12.

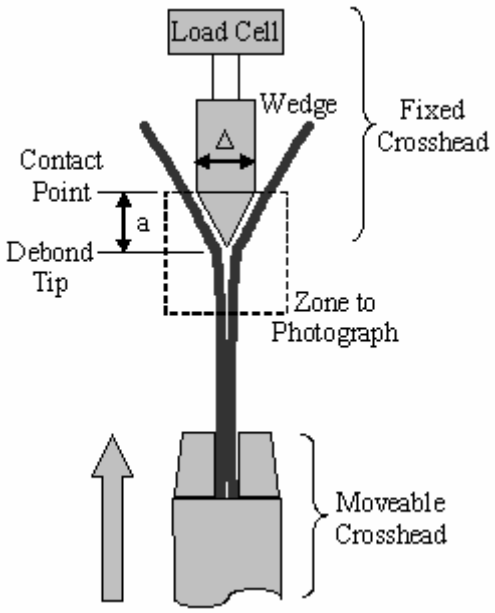

Figure 3.12. Schematic of driven wedge test configuration [22].

Due to the relatively short beam lengths (i.e. short crack lengths) associated with this test configuration, simple beam theory analyses resulted in excessively large fracture energy values. Since beam theory analysis methods do not take into account such phenomena as beam shear, root rotation, and end effects, numerical analyses were conducted on the driven wedge geometry to develop correction factors as a function of crack length to provide a more accurate characterization of the fracture behavior measured under the specified experimental conditions. Although details regarding the experimental test procedure utilized for this study, along with initial experimental results and in-depth discussions, will not be discussed herein, such information is available [22].

3.5.3: Compact Tension

To further understand the mode I fracture behavior of the adhesive studied herein, bulk adhesive compact tension (CT) specimens were tested over a range of globally applied loading rates. In combination with previously conducted experiments [23], results obtained from the CT tests provide valuable insight into the performance of the adhesive in question with regard to energy absorption capabilities. Additionally, thermal analysis results indicate that the time-temperature-superposition principle (TTSP) may be used to successfully predict the impact performance of the adhesive studied herein over a large range of theoretical loading rates with good accuracy.

To manufacture the CT specimens, the adhesive was first degassed in a centrifuge for 15 minutes at room temperature. A stainless steel plate coated with Lily RAM 225 mold release was used as a base mold in preparing the neat adhesive plaques. A silicon rubber dam, combined with appropriate spacers, was utilized as a support to a top plate in order to provide the desired thickness of the adhesive plaque once cured. Upon clamping the plates together, the assembly was cured for 60 minutes in a convection oven at 125°C, as per the manufacturer's suggestions. This procedure yielded cured neat adhesive plaques with a thickness of 8mm.

Once cured, CT specimens were fabricated according to ASTM standards [24] using a standard milling machine. Notches were incorporated into each sample at a depth of $0.45 a/w$, which is the minimum acceptable crack length according to [24], by using a high-speed steel slitting saw, where a is the crack length and w is the specimen depth. All specimens were pre-cracked manually by tapping a razor blade with a small hammer.

Finally, once fully prepared, all CT specimens were held for a minimum of seven days at room temperature prior to testing.

All CT tests were conducted on the same custom-designed MTS servo-hydraulic machine (MTS Corporation, Eden Prairie, MN) used for the bonded joint tests. A 9kN piezoelectric load cell was used for acquiring load measurements. Custom LabVIEW (National Instruments, Austin, TX) software was used for all data acquisition, providing sampling rates up to 100,000 data points per second. Furthermore, a slack adaptor, or loss motion device, was incorporated into the load train to allow the machine to reach the full specified test velocity prior to engaging the specimen, as well as to help provide sufficiently smooth loading profiles. This design made use of a small, off-the-shelf linear ball bearing combined with a 6.35mm diameter stainless steel rod and custom-machined aluminum housing to provide an adequate travel distance for test velocities up to 10m/s. A schematic of the modified load train utilized for all high-rate CT tests is illustrated in Figure 3.13.

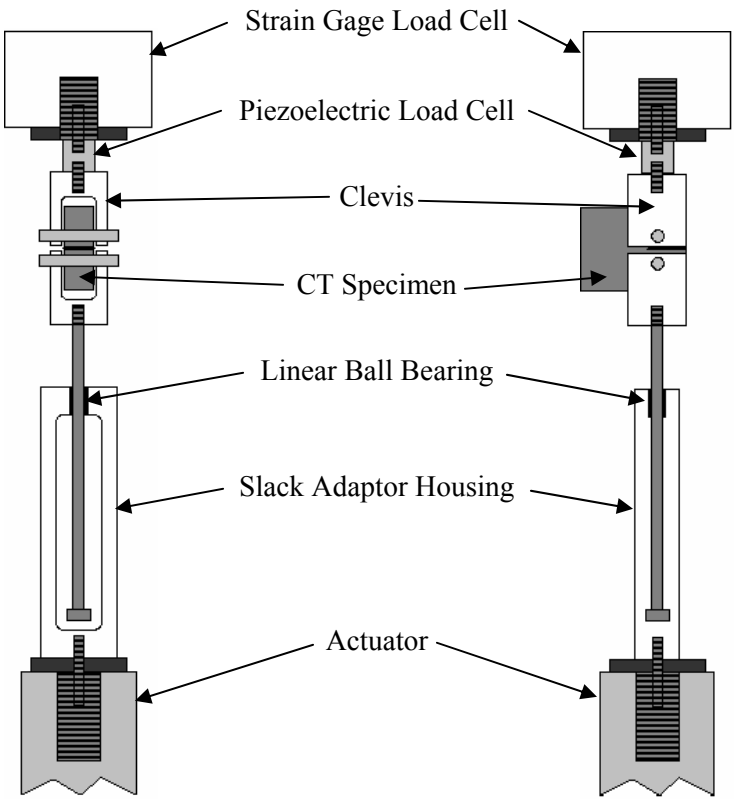

Figure 3.13. Modified load train used for dynamic compact tension tests.

3.5.4: Asymmetric Double Cantilever Beam

Asymmetric double cantilever beam specimens subjected to dynamic loads were tested in the same fashion as those subjected to static loads as described earlier in this thesis. Multiple analysis methods were utilized for purposes of comparison; however, a work-based method was chosen to be used for calculating the final results reported later in this thesis.

3.5.3: Single Leg Bend

The dynamic single leg bend specimens were tested using the same fixture as described in the static test setup section of this thesis. The same constant mixed-mode I/II ratio, $\mathcal{G}_{Ic}/\mathcal{G}_{IIc}$, was maintained at 1.33 as previously discussed. Data collection for this

testing procedure involved load, displacement, and time data capturing via the piezoelectric load cell output, as well as crack length measurements via the high-speed imaging system. Load-based, displacement-based, and work-based analysis methods were utilized for comparison purposes; however, a work-based method was used to calculate the final results reported in the Results section of this thesis [25]. As previously mentioned, a pre-cracking criterion of 60% of the total free length of the bonded beam specimen was employed.

3.5.4: End-Loaded Split

The dynamic ELS specimens were tested using the same fixture as described in the static test setup section of this thesis. Just as in the case of the dynamic SLB tests, load, displacement, and time data were collected from the piezoelectric load cell, while crack length data was captured from the high-speed imaging system. Load-based, displacement-based, and work-based analysis methods were also utilized for these mode II tests for comparison purposes; however, it should be noted that a work-based analysis was used to calculate the final results reported in the Results section of this thesis [25]. Additionally, the same pre-cracking criterion of 60% of the total free length of the bonded beam specimens as previously described was implemented.

References

1. Hashemi, S., Kinloch, A. J., and Williams, J. G., "The Analysis of Interlaminar Fracture in Uniaxial Fibre-Polymer Composites", *Proceedings of the Royal Society of London. Series A, Mathematical and Physical Sciences*, **427** (1872), 1990, pp. 173-199.
2. Kinloch, A. J., Wang, Y., Williams, J. G., and Yayla, P., "The Mixed-Mode Delamination of Fibre Composite Materials", *Composites Science and Technology*, **47**, 1993, pp. 225-237.
3. Choi, N. S., Kinloch, A. J., and Williams, J. G., "Delamination Fracture of Multidirectional Carbon-Fiber/Epoxy Composites Under Mode I, Mode II, and Mixed-Mode I/II Loading", *Journal of Composite Materials*, **33** (1), 1999, pp. 73-100.
4. Simón, J. C., Johnson, E., and Dillard, D. A., "Characterizing Dynamic Fracture Behavior of Adhesive Joints Under Quasi-Static and Impact Loading", *Journal of ASTM International*, **2** (7), 2005.
5. Simón, J. C., "Response and Failure of Adhesively Bonded Automotive Composite Structures under Impact Loads", Master's Thesis, Virginia Tech, Blacksburg, VA, 2004.
6. ASTM D-3433, Standard Test Method for Fracture Strength in Cleavage of Adhesives in Bonded Metal Joints, in *Annual Book of ASTM Standards*, 2003, ASTM: West Conshohocken, PA.

7. BSI. BS-7991: "Determination of the Mode I Adhesive Fracture Energy, $\mathcal{G}_{Ic}$, of Structural Adhesives Using the Double Cantilever Beam (DCB) and Tapered Double Cantilever Beam (TDCB) Specimens", 2001.
8. Hutchinson, J. W., and Suo, Z., "Mixed Mode Cracking in Layered Materials", *Advances in Applied Mechanics*, **29**, 1992, pp. 63-191.
9. Ducept, F., Gamby, D., and Davies, P., "A Mixed-Mode Failure Criterion Derived From Tests on Symmetric and Asymmetric Specimens", *Composites Science and Technology*, **59**, 1999, pp. 609-619.
10. Fernlund, G. and Spelt, J. K., "Mixed Mode Energy Release Rates for Adhesively Bonded Beam Specimens", *Journal of Composites Technology & Research*, *JCTRER*, **16** (3), 1994, pp. 234-243.
11. Xiao, F., Hui, C. Y., and Kramer, E. J., "Analysis of a Mixed Mode Fracture Specimen: the Asymmetric Double Cantilever Beam", *Journal of Materials Science*, **28**, 1993, pp. 5620-5629.
12. Guo, Y.-J. and Weitsman, Y. J., "A Modified DCB Specimen to Determine the Mixed Mode Fracture Toughness of Adhesives", *Engineering Fracture Mechanics*, **68**, 2001, pp. 1647-1668.
13. Pohlit, D. J., Dillard, D. A., Starbuck, J. M., and Jacob, G. C., "Mixed Mode Fracture Characterization of Bonded Composite Joints for Automotive Crashworthiness", *Proceedings of the 30th Annual Meeting of the Adhesion Society*, 2007, Tampa, FL, USA.
14. Blackman, B. R. K., Kinloch, A. J., and Paraschi, M., "The Determination of the Mode II Adhesive Fracture Resistance, $\mathcal{G}_{IIc}$, of Structural Adhesive Joints: An

Effective Crack Length Approach", *Engineering Fracture Mechanics*, **72**, 2005, pp. 877-897.

15. Blackman, B. R. K., Brunner, A. J., and Williams, J. G., "Mode II Fracture Testing of Composites: A New Look at an Old Problem", *Engineering Fracture Mechanics*, **73**, 2006, pp. 2443-2455.
16. Becht, G. and Gillespie, J. W., "Design and Analysis of the Crack Rail Shear Specimen for Mode III Interlaminar Fracture", *Composites Science and Technology*, **31**, 1988, pp. 143-157.
17. Donaldson, S. L., "Mode III Interlaminar Fracture Characterization of Composite Materials", *Composites Science and Technology*, **32**, 1988, pp. 225-249.
18. Lee, S. M., "An Edge Crack Torsion Method for Mode III Delamination Fracture Testing", *Journal of Composites Technology & Research*, **15** (3), 1993, pp.193-201.
19. Jacob, G. C., "Automotive Crashworthiness of Adhesively Bonded Carbon Fiber Polymer Composite Structures", Ph.D. Dissertation, University of Tennessee, Knoxville, TN, 2006.
20. Blackman, B. R. K., Dear, J. P., Kinloch, A. J., MacGillivray, H., Wang, Y., Williams, J. G., and Yayla, P., "The Failure of Fibre Composites and Adhesively Bonded Fibre Composites Under High Rates of Test: Part I – Mode I Loading – Experimental Studies", *Journal of Materials Science*, 30, 1995, pp. 5885-5900.
21. Blackman, B. R. K., Kinloch, A. J., Wang, Y., and Williams, J. G., "The Failure of Fibre Composites and Adhesively Bonded Fibre Composites Under High Rates

of Test: Part II – Mode I Loading – Dynamic Effects", *Journal of Materials Science*, 31, 1996, pp. 4451-4466.

22. Dillard, D. A., Jacob, G. C., Pohlit, D. J., and Starbuck, J. M., "On the Use of a Driven Wedge Test to Acquire Dynamic Fracture Energies of Bonded Beam Specimens: Part I - Motivation and Experimental Implementation", To be submitted (*Journal of Adhesion*).
23. Jacob, G. C., Starbuck, J. M., Pohlit, D. J., and Dillard, D. A., "Evaluating the Rate-Dependent Fracture Toughness of an Automotive Adhesive", In review (*Journal of Adhesion*).
24. ASTM D-5045, "Standard Test Methods for Plane-Strain Fracture Toughness and Strain Energy Release Rate of Plastic Materials", in *Annual Book of ASTM Standards*, 2004, ASTM: West Conshohocken, PA.
25. Blackman, B. R. K., Dear, J. P., Kinloch, A. J., MacGillivray, H., Wang, Y., Williams, J. G., and Yayla, P., "The Failure of Fibre Composites and Adhesively Bonded Fibre Composites Under High Rates of Test: Part III - Mixed-Mode I/II and Mode II Loadings", *Journal of Materials Science*, **21**, 1996, pp. 4467-4477.

Chapter 4. Fracture Analysis Methods

This section will provide details regarding the analysis methods employed in characterizing the fracture behavior of the various bonded joint geometries studied for this thesis. Each specimen configuration makes use of multiple analysis methods for comparison purposes; however, only the analysis methods used to report the final results at the end of this thesis will be examined in detail herein. Both static and dynamic fracture analysis methods will be discussed, including the use of appropriate correction factors obtained from the literature. Due to the stick-slip nature of the adhesive studied for the research described in this thesis, only the critical fracture energy, $\mathcal{G}_c$, will be considered when reporting the final results. Since researchers believe that arrest values obtained under stick-slip crack propagation are lower than the values that would be obtained if inertial effects were not involved [1] (i.e. non stick-slip behavior), the true arrest value of the adhesive material studied herein is believed to be higher than the apparent arrest values obtained experimentally. Therefore, experimentally measured arrest values will be discussed briefly in the Results section of this thesis; however, a much greater emphasis will be placed on the initiation, or critical, fracture energy, $\mathcal{G}_c$, instead. Additionally, load, opening displacement, and time data were collected for all tests using custom data acquisition software developed in-house. Crack length data was collected visually for all static tests, while the use of a high-speed imaging system was used to collect such data for all dynamic tests.

4.1: Double Cantilever Beam

As previously mentioned, static double cantilever beam tests were conducted using an Instron (Norwood, MA) 4500 series screw-driven test machine, while dynamic DCB tests were conducted using a custom-designed MTS (Eden Prairie, MN) servo-hydraulic test frame. Applied loading rates ranged from 1.7×10^{-5} m/s for the static tests to 10 m/s for the dynamic tests, with a number of intermediate test velocities. Two correction factors, as discussed later in this section, were utilized to account for large displacements and beam end-stiffening caused by the use of mechanically fastened steel loading blocks.

4.1.1: Static DCB Analysis

Much research has been conducted regarding mode I fracture using the DCB specimen geometry as an adopted standard [2-4]. For the purpose of this thesis, a Corrected Beam Theory (CBT) approach was selected to analyze the static DCB results obtained during this study [4-5]. This work-based approach utilizes collected load and opening displacement data to determine the static mode I strain energy release rate, $\mathcal{G}_I^{(static)}$, which can be calculated as:

$$\mathcal{G}_I^{(static)} = \frac{3P\Delta}{2b(a+\chi_I)} \cdot \frac{F}{N} \tag{4.1}$$

where P is the applied load, Δ is the opening displacement, b is the specimen width, a is the crack length, χ_I is a crack-length correction factor, F is a large displacement correction factor, and N is an end-block stiffening correction factor. The crack-length correction factor, χ_I, is utilized to account for the fact that the CBT analysis method is derived using a simple beam theory approach, and thus does not account for any shear or

root rotation that occurs at the crack tip [6]. This is due to the assumption that the specimen is a perfectly built-in cantilever beam. A value for this correction factor can be calculated by extrapolating a linear fit through the cube-root of the normalized compliance, $(C/N)^{1/3}$, versus crack length, a, data [4]. The x-intercept of this fit line is the value for the correction factor, χ_1.

The correction factor, F, accounts for the effective shortening of the loaded adherends due to large displacements and the tilting of the mechanically fastened end-blocks, and can be calculated as [7]:

$$F = 1 - \theta_1\left(\frac{\Delta}{L}\right)^2 - \theta_2\left(\frac{\Delta l_1}{L^2}\right) \tag{4.2}$$

where l_1 is illustrated in Figure A.1 and calculations for θ_1 and θ_2 are provided in Appendix A. For the case of the DCB specimen, $L = a$. Additionally, the correction factor, N, accounts for the stiffening effect of the mechanically fastened end-blocks, and can be calculated as [4,7]:

$$N = 1 - \theta_3\left(\frac{l_2}{L}\right)^3 - \theta_4\left(\frac{\Delta l_1}{L^2}\right) - \theta_5\left(\frac{\Delta}{L}\right)^2 \tag{4.3}$$

where l_2 is illustrated in Figure A.1 and calculations for θ_3, θ_4, and θ_5 are provided in Appendix A.

4.1.2: Dynamic DCB Analysis

Research has shown that when conducting fracture experiments under high test rates, it is important to distinguish between actual load data and unusable noise associated with inertia effects [8-10]. With this in mind, a displacement-based analysis approach

was examined for calculating the dynamic mode I strain energy release rate, $\mathcal{G}_{\mathrm{I}}^{(\mathrm{dynamic})}$ [11]:

$$\mathcal{G}_I^{(dynamic)} = \frac{3\Delta^2 h^3 E}{16(a+\chi_I h)^4} \cdot \frac{F}{N^2} \tag{4.4}$$

where E is the adherend flexural modulus. However, in order to maintain consistency amongst all of the different test specimen geometries, the work-based analysis shown in (4.1) of the previous section has been utilized for tabulating the final mode I dynamic fracture energy, $\mathcal{G}_{\mathrm{I}}^{(dynamic)}$. It will be shown in the Results chapter of this thesis that there is a significant difference in results obtained by using load, displacement, and work-based analysis methods, with the work-based method yielding fracture energy results somewhere in between the other two analysis methods. It should also be noted that the value for E should be determined from an independent flexural test; however, the literature does offer a back-calculation for this flexural modulus value to be used as a useful check on the testing procedure [4,7]:

$$E_f = \frac{8(a+\chi_I)^3}{\frac{C}{N} bh^3} \tag{4.5}$$

It is also suggested that if the maximum variation of E_f is more than 10% of the average, then the values calculated for $\mathcal{G}_{\mathrm{I}}$ should be considered suspect [4].

4.2 Driven Wedge Model Development

To evaluate the magnitude of the mode I fracture energy, $\mathcal{G}_{\mathrm{Ic}}$, along the crack front of the driven wedge specimens, a three-dimensional, linear elastic, quasi-static analysis was performed using ABAQUS/CAE [12], a commercially available finite

element software package. Three different specimen configurations were considered in the analysis: symmetric 11-ply, 20-ply, and 36-ply woven composite adherends with thicknesses of 2.8, 4.6, and 8.5 mm, respectively. Interaction between the composite adherends and the simulated wedge was established to allow for direct node-to-surface contact. A master-slave (i.e. wedge-adherend) relationship was established to prevent the wedge from passing through the adherend as it was progressively moved to the specified location during each computational iteration. Furthermore, a frictionless sliding condition was utilized to capture a realistic simulation of the actual experimental tests given that the percentage contribution of friction for the 11, 20, and 36ply specimens during the driven wedge tests were approximated at 0.72, 0.49, and 0.21%, respectively [13]. As such, the frictionless sliding condition assumption utilized for this study is reasonable.

For simplicity, the adhesive layer was not modeled, and thus the resultant strain energy output was a function only of the input adherend material properties in conjunction with the specified displacements, which were controlled directly according to the user specified wedge thickness, as well as the user specified crack lengths. By varying the crack length ahead of the wedge contact points, the energy release rate can be determined as a function of crack length; experimental distances can then be compared against these values to determine fracture energies. To determine the validity of neglecting the adhesive layer, an approach suggested by Penado [14], which is based on the work of Kanninen [15] in making use of a beam on elastic foundation approach, was utilized for determining the variation in compliance with respect to crack length for the various specimen thicknesses. When compared to empirical solutions calculated using a

beam theory approach, which included a shear correction [15], compliance values calculated for specimens without an adhesive layer were within 10-20% of those values calculated for specimens with an adhesive layer within the range of measured crack lengths observed in experimental testing [16]. As such, it was concluded that neglecting the contribution of the adhesive layer in this particular case was acceptable. Additionally, computational time was reduced by using a plane of symmetry on the face of the adherend where the crack was located, which eliminated the need to model both adherends, as well as the resulting mirrored half of the wedge.

The composite adherends were constrained in the *y*-and-*z*-directions along the bonded surface in order to prevent any transverse movement under the applied displacement conditions. Additionally, the back face of the geometry was fixed in order to prevent global specimen movement. Furthermore, a parallel-face boundary condition was established between the bottom face of the wedge geometry and the debonded surface of the adherend. This condition was created in order to maintain tangential sliding of the wedge along the debonded surface of the beam without allowing the wedge to rotate during the simulation. A schematic of the applied boundary conditions is illustrated in Figure 4.1.

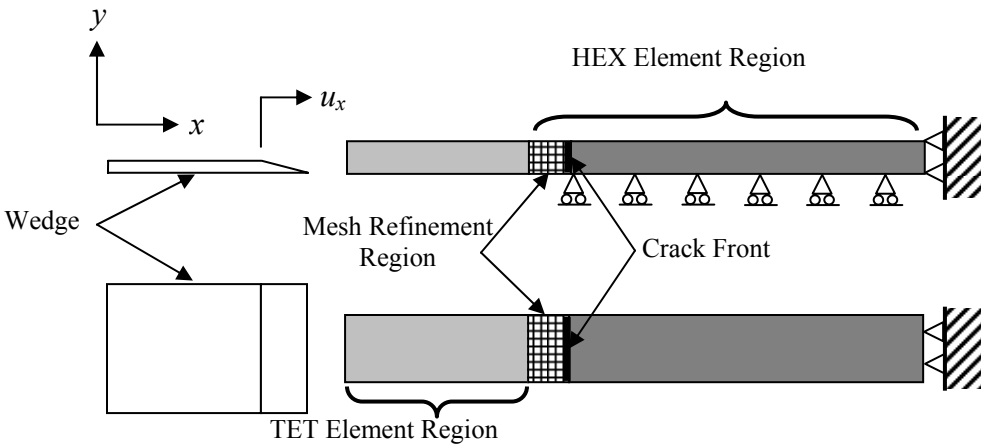

Figure 4.1. Driven wedge specimen FEA schematic.

The adherends were meshed with both four-node linear tetrahedral elements, C3D4, up to a point that was 10mm ahead of the crack front, and quadratic reduced-integration continuum 20-node brick elements, C3D20R, along the remaining length of the geometry. Tetrahedral elements were utilized ahead of the crack front in order to create the linear element region necessary for establishing adequate contact between the adherend and the wedge. Quadratic elements were used throughout the remainder of the specimens in order to provide a more accurate calculation of the resulting J-integral values [12]. Furthermore, a 10mm length mesh refinement region was created, as illustrated in Figure 4.1, in order to provide an adequate element size for the resulting crack contour regions in which calculating the J-integral values for each simulation was conducted. The size of the elements in this refined region were Δx = 1mm, Δy = 1.8mm, and Δz = 0.6mm. Similarly, the wedge geometry was created using the actual test wedge dimensions [14]; however, only a profile of the geometry was necessary since the wedge was modeled as an analytically rigid shell. Although the mesh densities utilized in this study varied because of varying specimen thicknesses and specified crack lengths, typical values of about 30,000 elements and 46,000 degrees of freedom were used for the 11ply specimens. An example of a resulting mesh utilized in this study is illustrated in Figure 4.2.

As previously mentioned, the mode I strain energy release rate was calculated using the built-in J-integral routine in ABAQUS/CAE. A total of five crack-tip contours were utilized to obtain accurate results, as recommended in the software manual [12], with the final contour being used for determining the associated energy release rate for each test, as the final contour always showed convergence amongst the calculated results.

The results obtained from this analysis were then correlated with those obtained using a simple beam theory (SBT) analysis approach in order to establish correction factors to be used in scaling the experimental results. More sophisticated analytical expressions could have been used, but SBT provides a convenient reference calculation upon which corrections can be based.

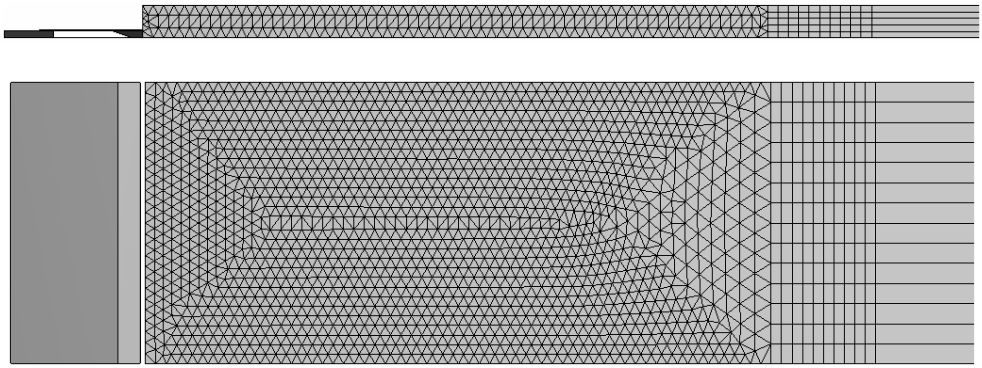

Figure 4.2. Driven wedge geometry mesh developed using ABAQUS/CAE FEA software.

4.3: Compact Tension

According to the ASTM standard [17], the mode I stress intensity factor can be calculated as:

$$K_I = \frac{F}{b\sqrt{w}} \cdot f\left[\frac{a}{w}\right] \tag{4.6}$$

where F is the applied load, b is the specimen thickness, w is the specimen width, a is the crack length, and f is a function of the non-dimensional crack length, a/w, which can be approximated as [17]:

$$f\left[\frac{a}{w}\right] = \frac{2+\left(a/w\right)}{\left(1-\left(a/w\right)\right)^{3/2}}\left[0.866 + 4.64\left(a/w\right) - 13.32\left(a/w\right)^2 + 14.72\left(a/w\right)^3 - 5.6\left(a/w\right)^4\right] \tag{4.7}$$

Additionally, assuming a load trace is linear to failure, a conditional fracture toughness, K_Q, is defined as the value of K_{Ic} calculated using $F = F_{max}$. Should the load-displacement trace prove to be nonlinear, the intercept of the trace and a line drawn at 95% of the linear slope can be used to determine an appropriate corresponding load, F_Q, to be used in calculating K_{Ic}. Furthermore, a plane strain fracture toughness value may be determined as $K_{Ic} = K_Q$ should the characteristic dimensions of the CT specimen be sufficiently large when compared with the resulting plastic zone size at the crack tip. To determine whether or not this plane strain assumption is quantifiably valid, the following expression should be true:

$$b, a, (w-a) > 2.5\left(K_Q / \sigma_y\right)^2 \tag{4.8}$$

where σ_y is the yield strength of the material.

4.4: Asymmetric Double Cantilever Beam

All asymmetric test specimens were manufactured by bonding two adherend materials of dissimilar thickness together in the same fashion as the standard DCB specimen fabrication method. The asymmetry of these specimens provided a constant mode-mixity ratio, dictated by the thickness ratios of the various adherends, which allowed for further fracture characterization of the material system studied herein. These specimens were loaded in the same configuration as used for the symmetric DCB testing, with the thinner adherend always being positioned on top. Three different configurations were tested and analyzed over a range of applied loading rates: 11x20, 20x36, and11x36 bonded composite specimens. It should be noted that not all specimen configurations

were tested across the entire range of applied loading rates studied due to material limitations, which will be reflected in the Results chapter of this thesis.

4.4.1: Static ADCB Analysis

While several methods exist for performing the analysis on ADCB specimens [18-21], a local partitioning method originally proposed by Hutchinson and Suo [22] was selected as the means for presenting the final results presented within this thesis. Using the general assumption of a homogeneous, isotropic layer of material, a general solution for the mode I and mode II stress intensity factor partitions, K_I and K_{II} respectively, under mixed-mode I/II loading conditions for asymmetric test specimens is provided [22]:

$$\begin{aligned} K_I &= \frac{P}{\sqrt{2hU}}\cos\omega + \frac{M}{\sqrt{2h^3V}}\sin(\omega+\gamma) \\ K_{II} &= \frac{P}{\sqrt{2hU}}\sin\omega - \frac{M}{\sqrt{2h^3V}}\cos(\omega+\gamma) \end{aligned} \tag{4.9}$$

where P is the applied load, M is the resulting applied moment, and U, V, γ, and ω are geometric factors that are a function of the adherend thickness ratio, h/H, as illustrated in Figure B.1 of Appendix B. Details regarding the solutions for these geometric factors are also provided in Appendix B.

Assuming a condition of plane strain at the crack tip, the mixed-mode I/II strain energy release rate partitions, $\mathcal{G}_{\mathrm{I}}$ and $\mathcal{G}_{\mathrm{II}}$, can be calculated using the following general form:

$$\mathcal{G} = \frac{K^2\left(1-\nu^2\right)}{E} \tag{4.10}$$

where E is the flexural modulus of the adherend material. Since the flexural modulus of the adherend materials studied for the purpose of this thesis was not constant, an average

modulus was calculated depending on the combination of materials used for the ADCB tests. Values of 45.8GPa, 39.3GPa, and 39.5GPa were calculated for the average adherend flexural moduli of the 11x20, 20x36, and 11x36 bonded composite ADCB specimens respectively.

4.4.2: Dynamic ADCB Analysis

Due to the complexity involved with the analysis associated with the fracture of the ADCB specimens utilizing the local partitioning method [22], only a beam theory displacement-based method was considered when performing the analysis on the dynamic fracture of the asymmetric DCB specimens in this thesis. Therefore, the mixed-mode I/II dynamic fracture energy, $\mathcal{G}_{\text{I/IIc}}$, of the ADCB specimens was calculated as using [18,23]:

$$\mathcal{G}_{I/II}^{(dynamic)} = \frac{3\Delta^2 E_1 E_2 h_1^{\,3} h_2^{\,3}}{8a^4\left(E_1 h_1^{\,3} + E_2 h_2^{\,3}\right)} \tag{4.11}$$

where Δ is the displacement, E_1 and E_2 are the flexural moduli of the thinner and thicker adherends respectively, h_1 and h_2 are the thicknesses of the thinner and thicker adherends respectively, and a is the crack length. Given the fixed-ratio of the mode-mixity associated with the ADCB tests, the total mixed-mode I/II energy release rate, $\mathcal{G}_{\text{I/II}}^{(dynamic)}$, can be partitioned for each specimen geometry into mode I, $\mathcal{G}_{\text{I}}$, and mode II, $\mathcal{G}_{\text{II}}$, fracture energy components [22]. The resulting mode-mixity ratios, $\mathcal{G}_{\text{I}}$:$\mathcal{G}_{\text{II}}$, for the 11x20, 20x36, and 11x36 bonded composite specimens were calculated to be roughly 9.9:1, 6.4:1, and 2.8:1 respectively.

However, to remain consistent throughout the analyses of the data presented herein, a work-based analysis has been utilized for tabulating the final dynamic mixed-mode I/II fracture energy, $\mathcal{G}_{\mathrm{I/II}}^{(dynamic)}$. The compliance of the ADCB specimen, as presented in [23], can be calculated as:

$$C = \frac{\Delta}{P} = \frac{4a^3}{b}\left(\frac{1}{E_1 h_1^{\,3}} + \frac{1}{E_2 h_2^{\,3}}\right) \tag{4.12}$$

Therefore, using algebraic manipulation, the work-based mixed-mode I/II fracture energy can be calculated as:

$$\mathcal{G}_{I/II}^{(dynamic)} = \frac{3P\Delta}{2a} \tag{4.13}$$

4.5: Single Leg Bend

All mixed-mode I/II single leg bend tests were conducted on symmetric, bonded composite specimens that resulted in a fixed-ratio mode-mixity level, $\mathcal{G}_{\mathrm{I}}/\mathcal{G}_{\mathrm{II}}$, of 4:3 [7]. All tests were conducted using an in-house developed sliding test fixture. The motivation behind the development of this fixture was to minimize the transverse load associated with the applied loading configuration. This was achieved by clamping the SLB specimens to a small mounting assembly at the end of a freely sliding shaft, which traveled through a linear ball bearing that was mounted to the load frame. A schematic of the test fixture, along with an actual photograph of the test set-up, has been provided in Chapter 3 of this thesis.

4.5.1: Static SLB Analysis

While other specimen configurations, corresponding test fixtures, and relevant analysis methods associated with the mixed-mode I/II fracture of bonded joints exist [24-28], the single leg bend [29], also known as the fixed-ratio mixed-mode, specimen geometry was chosen because of its simplicity and easy adaptation to both static and dynamic fracture testing. Although several possible analysis methods exist for this particular specimen configuration, a work-based approach has been utilized for the case of static loading. In particular, calculations for the corresponding mode I and mode II components of the total strain energy release rate associated with the mixed-mode I/II fracture, $\mathcal{G}_{I/II}$, of the SLB specimens will be discussed [7]. These components, $\mathcal{G}_{I}$ and $\mathcal{G}_{II}$ respectively, can be calculated as follows:

$$\begin{aligned} \mathcal{G}_I &= \frac{6P\Delta}{b}\left[\frac{\left(a+\chi_I h\right)^2}{7\left(a+\chi_{II}h\right)^3+\left(L+2\chi_I h\right)^3}\right]\cdot\frac{1}{N}, \\ \mathcal{G}_{II} &= \frac{9P\Delta}{2b}\left[\frac{\left(a+\chi_{II} h\right)^2}{7\left(a+\chi_{II}h\right)^3+\left(L+2\chi_I h\right)^3}\right]\cdot\frac{1}{N} \end{aligned} \tag{4.14}$$

where P is the applied load, Δ is the opening displacement, a is the crack length, h is the adherend thickness, b is the specimen width, L is the unclamped, or free, length of the specimen, χ_I is the mode I compliance correction factor, χ_{II} is the mode II compliance correction factor, which can be estimated as $0.42\chi_I$, and N is the end-block stiffening correction factor. It should be noted that a more accurate value for χ_{II} can also be determined experimentally [30-31]; however, for simplicity herein, the referenced approximation will be utilized. Furthermore, the end-block stiffening correction factor, N, can be calculated using (4.3), and the key components of this calculation for the SLB specimen geometry can be found in Appendix A.

4.5.2: Dynamic SLB Analysis

For reasons explained earlier regarding the validity of measured load data gathered from high rates of test, a displacement-based approach was examined when calculating the mode I and mode II strain energy release rate components of the SLB specimens subjected to dynamic loading conditions. These components can be calculated as [7]:

$$\begin{aligned} \mathcal{G}_I &= \frac{12\Delta^2 h^3 E\left(a+\chi_I h\right)^2}{\left[7\left(a+\chi_{II}h\right)^3+\left(L+2\chi_I h\right)^3\right]^2}\cdot\frac{F}{N^2} \\ \mathcal{G}_{II} &= \frac{9\Delta^2 h^3 E\left(a+\chi_{II} h\right)^2}{\left[7\left(a+\chi_{II}h\right)^3+\left(L+2\chi_I h\right)^3\right]^2}\cdot\frac{F}{N^2} \end{aligned} \tag{4.15}$$

where F is a correction for large displacements. Similar to the DCB results that will be reported later in the Results chapter of this thesis, load, work, and displacement-based results for the SLB specimens will be compared, and will again illustrate that results obtained using a work-based analysis method yield fracture energies somewhere in between those calculated using load and displacement-based methods. To remain consistent among test methods, the work-based analysis method of (4.14) has been utilized for determining the critical dynamic mixed-mode fracture energy, $\mathcal{G}_{\mathrm{I/IIc}}^{(dynamic)}$. Additionally, it should be noted that the literature recommends a crack length criterion of $a \geq 0.4L$ [7], which was implemented for the study conducted herein.

4.6: End-Loaded Split

All mode II end-loaded split tests were conducted on symmetric bonded composite specimens using the same test fixture as described in the single leg bend section of the current chapter of this thesis. Due to the load-frame setup, ELS specimens

were subjected to both static and dynamic loading by applying a downward force to the top adherend, thus forcing the two adherends together and creating a mode II in-plane shearing fracture criterion.

4.6.1: Static ELS Analysis

A work-based analysis method based on beam theory was implemented when performing the analysis on the statically-loaded end-loaded split specimens. This method was first described by Hashemi *et al.* [7], but was later updated to account for a mode II compliance correction factor that varied from that obtained from mode I testing [30]. The more recent analysis for the determination of the mode II strain energy release rate, $\mathcal{G}_{\mathrm{II}}$, can be described as follows:

$$\mathcal{G}_{II} = \frac{9P\Delta\left(a+\Delta_{II}\right)^2}{2b\left[3\left(a+\Delta_{II}\right)^3+\left(L+\Delta_{clamp}\right)^3\right]}\cdot\frac{F}{N} \tag{4.16}$$

where P is the applied load, Δ is the opening displacement, a is the crack length, Δ_{II} is the mode II compliance correction factor, b is the specimen width, L is the free length, Δ_{clamp} is a free-length correction factor, and F and N are correction factors for large displacements and end-block stiffening effects. Calculations for the key components of F and N relative to the ELS specimen geometry can be found in Appendix A.

The procedure for determining the free-length correction factor, Δ_{clamp}, is outlined in the literature [30], and a brief outline of this procedure can also be found in Chapter 2 of this thesis, so it will not be elaborately discussed herein. However, it can be said that this correction factor is determined via an inverse ELS test, where the cracked portion of an ELS specimen is held fully within the test fixture clamp and loaded in the same

fashion as a standard ELS specimen. Therefore, the compliance, C_o, of the inversely clamped bonded composite specimen can be determined by [30]:

$$\left(\frac{C_o}{N}\right)^{1/3} = \left(\frac{1}{2bh^3E}\right)^{1/3} L + \left(\frac{1}{2bh^3E}\right)^{1/3} \Delta_{clamp} \tag{4.17}$$

It has been shown that incorporating this free-length correction provides more reasonable results compared with those obtained using more traditional beam theory analysis methods. Furthermore, it is recommended [7] that a stability criterion of $a \geq \sim 0.60L$ be utilized for the ELS specimen geometry.

4.6.2: Dynamic ELS Analysis

Due to the nature of the end-loaded split test, a maximum of two data points were obtained per specimen, although it was much more common to only obtain one data point per test specimen due to the propensity of the crack to propagate into the composite adherends. In the latter case, it was not necessary to utilize a high-speed imaging system in order to monitor crack propagation during high-speed tests on ELS specimens, although high-speed video was still utilized for the purpose of obtaining the resulting videos for subsequent analysis. However, by conducting multiple tests on specimens at multiple applied loading rates, an average mode II fracture energy could be calculated for a given applied loading rate, which will be reported in the Results chapter of this thesis. In general, a displacement-based approach was used to calculate the strain energy release rate, $\mathcal{G}_{II}$, associated with the mode II fracture of bonded composite ELS specimens subjected to dynamic loading conditions [7]:

$$\mathcal{G}_{II} = \frac{9\Delta^2 h^3 E\left(a + \Delta_{II}\right)^2}{\left[3\left(a + \Delta_{II}\right)^3 + \left(L + 2\Delta_I\right)^3\right]^2} \cdot \frac{F}{N^2} \tag{4.18}$$

4.7: Split Cantilever Beam

When compared with the other modes of fracture, limited research has been conducted regarding mode III fracture. Under out-of-plane shear (mode III) loading, several different testing methods have been attempted, such as the crack rail shear (CRS) [32], edge crack torsion (ECT) [33], anticlastic bending [34], and four-point end-notched flexure (4-ENF) [35]. However, a test geometry quite similar to that of the DCB specimen configuration is that of the split cantilever beam (SCB) specimen, which lends itself nicely to both static and dynamic fracture testing. Donaldson [36] was the first to propose this specimen configuration; however, it has been shown that there is a significant mode II component present at the edges of the SCB specimen in the standard configuration [37]. Although test fixture refinements have been shown to help reduce the mode II contribution [38-39], nothing has been proven to completely eliminate the mode II fracture component present in the SCB specimen. However, for simplicity and for the purpose of this thesis, tests were conducted using the SCB specimen geometry in an attempt to characterize the mode III fracture behavior of the adhesive in question. A schematic of the SCB test configuration is illustrated in Figure 4.3.

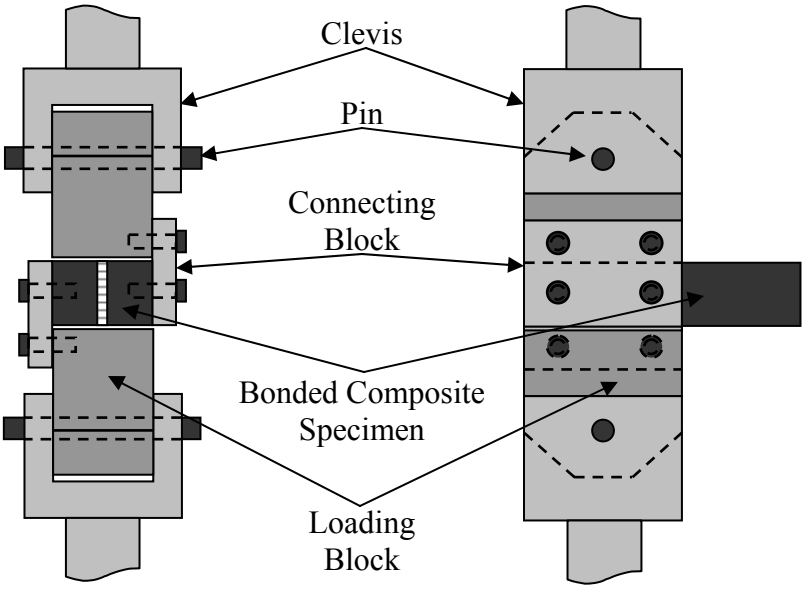

Figure 4.3. Split cantilever beam (SCB) test configuration.

4.7.1: SCB Analysis

With minimal research findings available in the literature with regard to the split cantilever beam specimen geometry, the breadth of the data analysis associated with this test is equally limited. An experimental compliance method was utilized in order to calculate the mode III strain energy release rate, $\mathcal{G}_{\text{III}}$, associated with the SCB tests [36]. However, due to the presence of a significant mode II component toward the specimen edges, this value is actually a total energy release rate, $\mathcal{G}_{\text{tot}}$, and will be referred to as such. This method uses actual experimental data to calculate $\mathcal{G}_{\text{tot}}$, which appears to provide a reasonable means for characterizing the mode III fracture response of this specimen configuration and can be calculated by [36]:

$$\mathcal{G}_{tot} = \frac{nP\Delta}{2ba} \tag{4.19}$$

where P is the applied load, Δ is the opening displacement, b is the bond width, a is the crack length, and n is the slope of the log(C) versus log(a) curve, where C is the measured compliance.

As previously mentioned, there is a significant mode II component at the edges of the SCB specimen geometry, as shown in previous studies [12,37-39]. In the study conducted herein, this could be characterized by a ripping of composite plies from the beam adherends resulting from the combination of mode II and mode III fracture components, thus resulting in a stepped fracture surface. This concept is better illustrated in Figure 4.4.

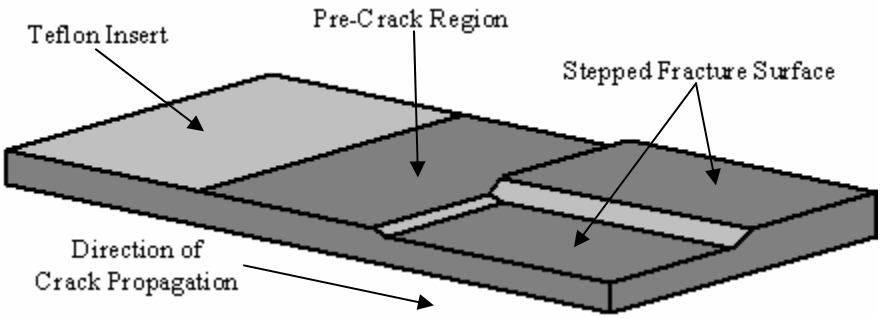

Figure 4.4. Schematic of typical failure surface for SCB specimen.

Finite element analysis has been conducted on the SCB specimen geometry to determine the level of mode II contribution. It has been observed, as will be shown in the Results chapter of this thesis, that the mode II fracture energy component decays rapidly away from the edges of the SCB specimen. While the experimental analysis conducted for the purpose of this thesis does not consider the partitioning of the two present fracture energy components, $\mathcal{G}_{II}$ and $\mathcal{G}_{III}$, it has been assumed that using an average measurement of the total data collected along the length of the SCB specimens provides a reasonable means for characterizing the mode III fracture behavior of the adhesive in question, based

on analytical findings via the aforementioned finite element analysis. This assumption has been made based on the fact that the mode II component closely follows an exponential decay toward the center of the bonded specimen, as previously mentioned, resulting in a mode III dominated central region.

4.7.2: Finite Element Analysis – Full Bond

In order to better understand the mode-mix present in the current SCB specimen geometry, an FE analysis was conducted. Although the experimental study presented herein focuses on the use of composite adherends, isotropic materials were used in the FE analysis for simplicity, as this study was conducted merely to determine the level of $\mathcal{G}_{II}/\mathcal{G}_{III}$ mode-mixity present in the SCB specimen geometry. Furthermore, with the technique used to calculate the various strain energy release rate components, $\mathcal{G}_I$, $\mathcal{G}_{II}$, and $\mathcal{G}_{III}$, which will be described later, the utilization of anisotropic adherends combined with an isotropic adhesive layer is not possible, as stated in [12]. Aluminum adherends were modeled using three-dimensional eight-node linear solid (HEX) brick elements with reduced integration (C3D8R) within the ABAQUS/CAE environment. Additionally, an adhesive layer was created between the two adherends using the same brick elements, with six elements being prescribed through the thickness of the adhesive layer. On average, there were roughly 55,000 elements and 200,000 degrees of freedom utilized for each simulation.

A crack front was prescribed at the leading edge of the adhesive layer using standard partitioning techniques in order to place the crack at the mid-plane of the adhesive layer in an attempt to evaluate the distribution of the different strain energy

release rate components along the prescribed crack front. Furthermore, pin sections were created toward the displaced end of the specimen geometry in an attempt to accurately capture the true specimen geometry set-up and loading configurations. Several models were examined by partitioning the standard beam geometry such that the effects of various prescribed crack lengths could be studied. All models included a refined mesh close to the crack front in both the *x*-*y* and *x*-*z* planes, as illustrated in Figure 4.5. Furthermore, the size of the elements in the refined mesh region near the crack tip were Δx = 0.5mm, Δy = 0.85mm, and Δz = 1.7mm for the adherends, and similarly for the adhesive layer, while the through-the-thickness dimension, Δz, was held constant as previously mentioned.

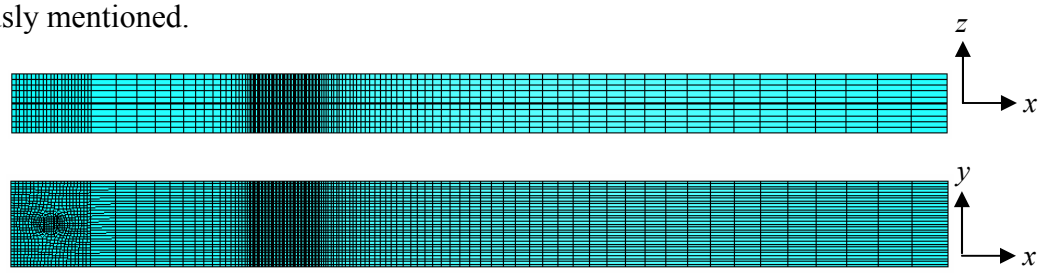

Figure 4.5. Split cantilever beam (SCB) geometry finite element mesh.

Crack lengths ranging from 50mm to 200mm in 25mm increments were studied in order to determine the level of mode-mixity present as a function of the debond length. Stress intensity factors – K_I, K_{II}, and K_{III} – were calculated at the crack tip by specifying a contour integral region in the refined mesh area surrounding the crack tip. A total of five contour integrals were utilized for convergence and accuracy, with the results obtained from the final contour being used in the final calculations, as recommended in [12]. From the calculated stress intensity factors, the strain energy release rate components –

$\mathcal{G}_{\mathrm{I}}$, and $\mathcal{G}_{\mathrm{II}}$ – could be calculated directly using the relationship provided in (4.10). However, $\mathcal{G}_{\mathrm{III}}$ must be calculated using the following relationship:

$$\mathcal{G}_{III} = \frac{K_{III}^{\ 2}(1+\nu)}{E} \tag{4.20}$$

Results from the FE analysis conducted on the SCB specimens show that there is indeed a significant mode II strain energy release rate component present toward the specimen edges. This component, $\mathcal{G}_{\mathrm{II}}$, decays rapidly as one moves more toward the center of the specimen, where the mode III component, $\mathcal{G}_{\mathrm{III}}$, is dominant. In all cases, there is a negligible mode I component, $\mathcal{G}_{\mathrm{I}}$, present at the crack front. Furthermore, it will be shown that the mode-mix ratio, $\mathcal{G}_{\mathrm{II}}/\mathcal{G}_{\mathrm{III}}$, increases with increasing crack length for a full bond width analysis. Detailed results of this analysis will be provided in the Results chapter of this thesis.

4.7.3: Finite Element Analysis – Half Bond

In an attempt to acquire meaningful mode III fracture data, a modification was made to the standard SCB specimen geometry in an analytical sense and an additional FEA study was conducted; however, no experiments were ever conducted on these modified specimens. While the adherends maintained a width of 25mm, the bond width was decreased by a factor of two, resulting in a centrally-located bond of 12.7mm width. This particular geometry was selected for this analysis to determine the effect bond width had on the overall mode-mixity present in the SCB specimen. Moreover, it was believed that by decreasing the bond width, the new specimen may provide an adequate means for characterizing mode III fracture in a more accurate manner by decreasing the contribution of the previously significant mode II strain energy release rate component.

The geometry of the half bond width specimen was created in the same fashion as previously explained within the ABAQUS/CAE environment. Again, crack lengths ranging from 50mm to 200mm in increments of 25mm were studied to determine the effect of crack length on the corresponding level of mode mixity, $\mathcal{G}_I$-$\mathcal{G}_{II}$-$\mathcal{G}_{III}$, present in the modified SCB specimen. The only modification implemented included the partitioning of the plane of symmetry, or fracture surface, to allow for a bond surface, or adhesive layer, of decreased width. As a result, there were roughly 50,000 elements and 180,000 degrees of freedom utilized for each simulation.

Results from the FE analysis show that, while there is still a mode II strain energy release rate component present at the edges of the bond, it is much less significant than observed in the analysis concerning specimens with bonds the full width of the specimen. With the exception of the extreme free edges of the bond, the mode-mix ratio, $\mathcal{G}_{II}/\mathcal{G}_{total}$, reaches a maximum level of 20% for the corresponding range of crack lengths studied, which is roughly half the level observed for simulations conducted on the full bond width specimens. When considering the measurement of the strain energy release rate, $\mathcal{G}_{III}$, in an average sense, this specimen geometry appears to be much more suitable for characterizing the mode III fracture behavior of the material system studied for the purpose of this thesis. Detailed findings of this FE analysis will be presented in the Results chapter of this thesis.

References

1. Anderson, T. L., Fracture Mechanics: Fundamentals and Applications. 2nd Edition. CRC Press: Boca Raton, 1995.
2. Ripling, E. J., Mostovoy, S., and Patrick, R. L., "Application of Fracture Mechanics to Adhesive Joints", in *ASTM STP 360*, 1963.
3. ASTM D-3433-99, "Standard Test Method for Fracture Strength in Cleavage of Adhesives in Bonded Metal Joints", in *Annual Book of ASTM Standards*, 2003, ASTM: West Conshohocken, PA.
4. BSI. *BS-7991*: "Determination of the Mode I Adhesive Fracture Energy, G_{Ic}, of Structural Adhesives Using the Double Cantilever Beam (DCB) and Tapered Double Cantilever Beam (TDCB) Specimens", 2001.
5. Blackman, B. R. K., Kinloch, A. J., Paraschi, M., and Teo, W. S., "Measuring the Mode I Adhesive Fracture Energy, G_{Ic}, of Structural Adhesive Joints: The Results of an International Round-Robin", *International Journal of Adhesion & Adhesives*, **23**, 2003, pp. 293-305.
6. Williams, J. G., "End Corrections for Orthotropic DCB Specimens", *Composites Science and Technology*, **35**, 1989, pp. 367-376.
7. Hashemi, S., Kinloch, A. J., and Williams, J. G., "The Analysis of Interlaminar Fracture in Uniaxial Fibre-Polymer Composites", *Proceedings of the Royal Society of London. Series A, Mathematical and Physical Sciences*, **427** (1872), 1990, pp. 173-199.

8. Blackman, B. R. K., Kinloch, A. J., Wang, Y., and Williams, J. G., "The Failure of Fibre Composites and Adhesively Bonded Fibre Composites Under High Rates of Test: Part II – Mode I Loading – Dynamic Effects", *Journal of Materials Science*, 31, 1996, pp. 4451-4466.
9. Williams, J. G., "Transient Effects During Rapid Crack Propagation", *International Journal of Fracture*, **93**, 1998, pp. 51-61.
10. Simón, J. C., "Response and Failure of Adhesively Bonded Automotive Composite Structures under Impact Loads", Master's Thesis, Virginia Tech, Blacksburg, VA, 2004.
11. Blackman, B. R. K., Dear, J. P., Kinloch, A. J., MacGillivray, H., Wang, Y., Williams, J. G., and Yayla, P., "The Failure of Fibre Composites and Adhesively Bonded Fibre Composites Under High Rates of Test: Part I – Mode I Loading – Experimental Studies", *Journal of Materials Science*, **30**, 1995, pp. 5885-5900.
12. ABAQUS Analysis User's Manual, Vol. 2: Analysis, Version 6.5, 2004.
13. Pohlit, D. J., Dillard, D. A., Jacob, G. C., Starbuck, J. M., and Kapania, R., "On the Use of a Driven Wedge Test to Acquire Dynamic Fracture Energies of Bonded Beam Specimens: Part II - Numerical Analysis", To be submitted (*Journal of Adhesion*).
14. Penado, F. E., "A Closed Form Solution for the Energy Release Rate of the Double Cantilever Beam Specimen with an Adhesive Layer", *Journal of Composite Materials*, **27** (4), 1993, pp. 383-407.

15. Kanninen, M. F., "An Augmented Double Cantilever Beam Model for Studying Crack Propagation and Arrest", *International Journal of Fracture*, **9** (1), 1973, pp. 83-91.
16. Dillard, D. A., Jacob, G. C., Pohlit, D. J., and Starbuck, J. M., "On the Use of a Driven Wedge Test to Acquire Dynamic Fracture Energies of Bonded Beam Specimens: Part I - Motivation and Experimental Implementation", To be submitted (*Journal of Adhesion*).
17. ASTM D-5045, "Standard Test Methods for Plane-Strain Fracture Toughness and Strain Energy Release Rate of Plastic Materials", in *Annual Book of ASTM Standards*, 2004, ASTM: West Conshohocken, PA.
18. Xiao, F., Hui, C. Y., and Kramer, E. J., "Analysis of a Mixed Mode Fracture Specimen: The Asymmetric Double Cantilever Beam", *Journal of Materials Science*, **28**, 1993, pp. 5620-5629.
19. Ducept, F., Gamby, D., and Davies, P., "A Mixed-Mode Failure Criterion Derived from Tests on Symmetric and Asymmetric Specimens", *Composites Science and Technology*, **59**, 1999, pp. 609-619.
20. Fernlund, G. and Spelt, J. K., "Mixed Mode Energy Release Rates for Adhesively Bonded Beam Specimens", *Journal of Composites Technology & Research*, *JCTRER*, **16** (3), 1994, pp. 234-243.
21. Guo, Y.-J. and Weitsman, Y. J., "A Modified DCB Specimen to Determine Mixed Mode Fracture Toughness of Adhesives", *Engineering Fracture Mechanics*, **68**, 2001, pp. 1647-1668.

22. Hutchinson, J. W. and Suo, Z., "Mixed Mode Cracking in Layered Materials", *Advances in Applied Mechanics*, **29**, 1992, pp. 63-191.

23. Maugis, D. (2000). *Contact, Adhesion, and Rupture of Elastic Solids*. New York: Springer.

24. Reeder, J. R. and Crews, J. H. J., "Redesign of the Mixed-Mode Bending Delamination Test to Reduce Nonlinear Effects", *Journal of Composites Technology and Research*, **14**, 1992, pp. 12-19.

25. ASTM D-6671/D 6671M-04, "Standard Test Method for Mixed Mode I-Mode II Interlaminar Fracture Toughness of Unidirectional Fiber Reinforced Polymer Matrix Composites", in *Annual Book of ASTM Standards*, 2004, ASTM: West Conshohocken, PA.

26. Kinloch, A. J., Wang, Y., Williams, J. G., and Yayla, P., "The Mixed-Mode Delamination of Fibre Composite Materials", *Composites Science and Technology*, **47**, 1993, pp. 225-237.

27. Bhashyam, S. and Davidson, B. D., "An Evaluation of Data Reduction Methods for the Mixed Mode Bending Test", *AIAA*, 1996, pp. 886-896.

28. Szekrényes, A. and József, U., "Over-Leg Bending Test for Mixed-Mode I/II Interlaminar Fracture in Composite Laminates", *International Journal of Damage Mechanics*, **16**, 2007, pp. 5-33.

29. Davidson, B. D. and Sundararaman, V., "A Single Leg Bending Test for Interfacial Fracture Toughness Determination", *International Journal of Fracture*, **78**, 1996, pp. 193-210.

30. Blackman, B. R. K., Kinloch, A. J., and Paraschi, M., "The Determination of the Mode II Adhesive Fracture Resistance, G_{IIc}, of Structural Adhesive Joints: An Effective Crack Length Approach", *Engineering Fracture Mechanics*, **72**, 2005, pp. 877-897.
31. Blackman, B. R. K., Brunner, A. J., and Williams, J. G., "Mode II Fracture Testing of Composites: A New Look at an Old Problem", *Engineering Fracture Mechanics*, **73**, 2006, pp. 2443-2455.
32. Becht, G. and Gillespie, J. W., "Design and Analysis of the Crack Rail Shear Specimen for Mode III Interlaminar Fracture", *Composites Science and Technology*, **31**, 1988, pp. 143-157.
33. Lee, S. M., "An Edge Crack Torsion Method for Mode III Delamination Fracture Testing", *Journal of Composites Technology & Research*, **15** (3), 1993, pp. 193-201.
34. Farshad, M. and Flüeler, P., "Investigation of Mode III Fracture Toughness Using an Anti-Clastic Plate Bending Method", *Engineering Fracture Mechanics*, **60**, 1998, pp. 597-603.
35. Yoshihara, H., "Examination of the 4-ENF Test for Measuring the Mode III *R*-Curve of Wood", *Engineering Fracture Mechanics*, **73**, 2006, pp. 42-63.
36. Donaldson, S. L., "Mode III Interlaminar Fracture Characterization of Composite Materials", *Composites Science and Technology*, **32**, 1988, pp. 225-249.
37. Martin, R. H., "Evaluation of the Split Cantilever Beam for Mode III Delamination Testing", in *Composite Materials: Fatigue and Fracture (Third Volume), ASTM STP 1110*, 1991, pp. 243-266.

38. Sharif, F., Kortschot, M. T., and Martin, R. H., "Mode III Delamination Using a Split Cantilever Beam", in *Composite Materials: Fatigue and Fracture (Fifth Volume), ASTM STP 1230*, 1995, pp. 85-99.

39. Cicci, D., Sharif, F., and Kortschot, M. T., "Data Reduction for the Split Cantilever Beam Mode III Delamination Test", *Proceedings of ICCM-10*, Whistler, B. C., Canada, August 1995.

Chapter 5: Results and Discussion

This chapter will provide detailed results obtained from both quasi-static and dynamic fracture tests with regards to mode I, mixed-mode I/II, mode II, and mode III fracture of bonded composite joints. However, for the mode III specimen geometry, only quasi-static data will be presented, as no dynamic tests were conducted on this particular mode of fracture. Initially, a variety of analysis methods were implemented in order to develop a means for comparison regarding results obtained for each of the different modes of fracture. Comparisons will be made in order to illustrate the differences among the various methods of analysis. However, for the purpose of this thesis, a work-based method has been utilized for reporting the final critical energy release rates. Additionally, results from dynamic fracture tests conducted on bulk adhesive compact tension (CT) specimens will be presented. A correlation between results obtained from the mode I bonded joint tests and the compact tension tests will also be established. Furthermore, dynamic mechanical analysis (DMA) data collected on the bulk adhesive will also be presented, and results related to the implementation of time-temperature superposition with regards to the adhesive studied herein will be examined.

5.1: Double Cantilever Beam

Testing conducted on all DCB specimens provided limited data points due to the stick-slip nature of the adhesive utilized for this study. In general, roughly three to four data points were collected per 300mm length specimen.

5.1.1: Static DCB

All static DCB tests were conducted according to BS 7991:2001 [1] at an applied loading rate of 1mm/min. Specimens were loaded up to a point that resulted in crack initiation, at which time they were unloaded approximately to the test origin in order to determine whether or not any permanent deformation had occurred within the specimen adherends. No permanent deformation was observed. Specimens were then reloaded and allowed to experience crack propagation along their full length until complete fracture had occurred, thus resulting in two separate adherends. Representative load-displacement traces for each specimen configuration tested under quasi-static loading conditions are provided in Figure 5.1.

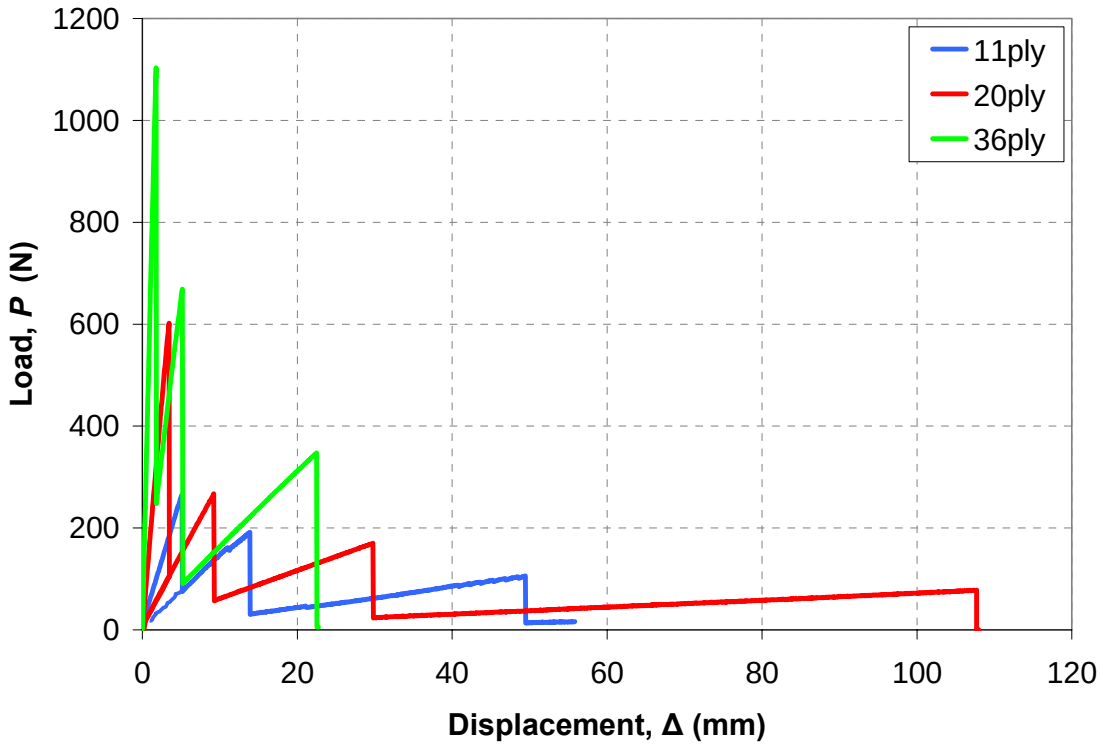

Figure 5.1. Typical load-displacement traces for 11, 20, and 36-ply DCB specimens.

While load-displacement data were continuously measured throughout the duration of the tests, only maximum and minimum values associated with crack initiation or arrest were used in calculating the resulting critical and arrest strain energy release rates, $\mathcal{G}_{Ic}$ and $\mathcal{G}_{Ia}$, respectively. Figure 5.2 illustrates the results gathered from these tests for 11, 20, and 36-ply bonded composite specimens with a 0.5mm bond-line thickness.

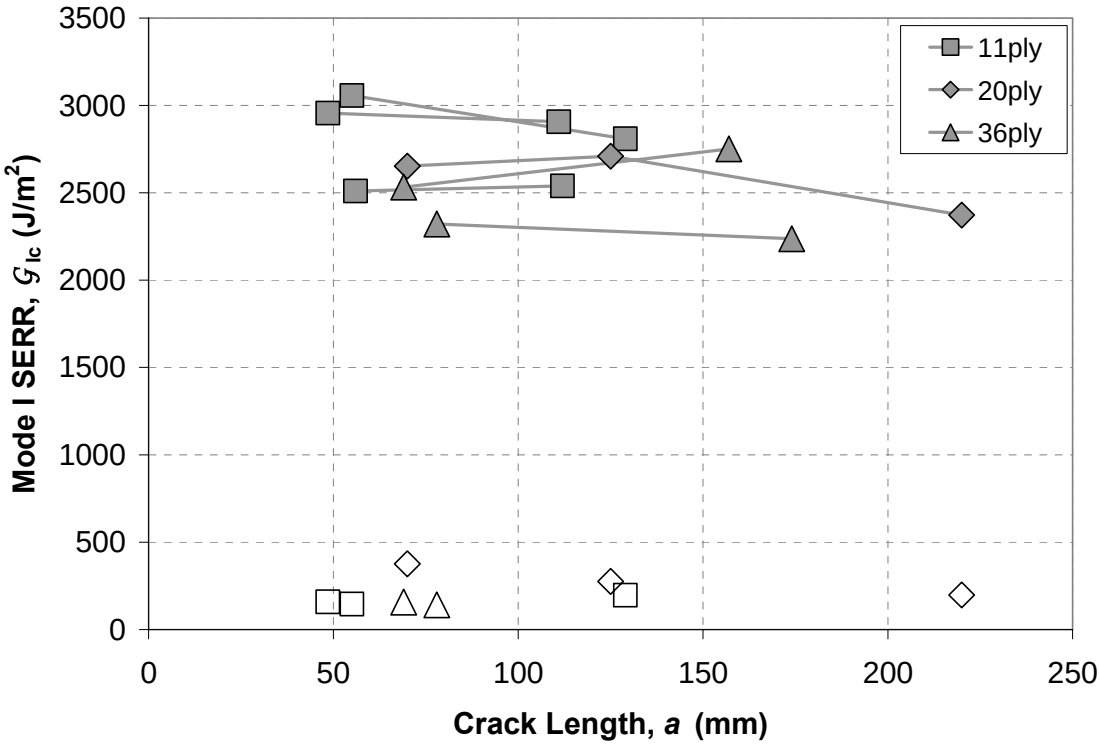

Figure 5.2. Mode I strain energy release rate, $\mathcal{G}_I$, vs. crack length, a, for 11, 20, and 36-ply bonded composite DCB specimens. Open symbols represent arrest values and shaded symbols represent critical values.

It should be noted that the connecting lines between the crack initiation data points in Figure 5.2 are included only to guide the reader's eye between data points for individual tests. All results presented in Figure 5.2 correspond to cohesive failure within the adhesive layer. Figure 5.3 shows the fracture surfaces of typical 11, 20, and 36-ply

bonded composite specimens resulting from quasi-static loading conditions. The stick slip nature of the fractures is evident from the pronounced thumbnail crack arrest fronts showing significant stress whitening.

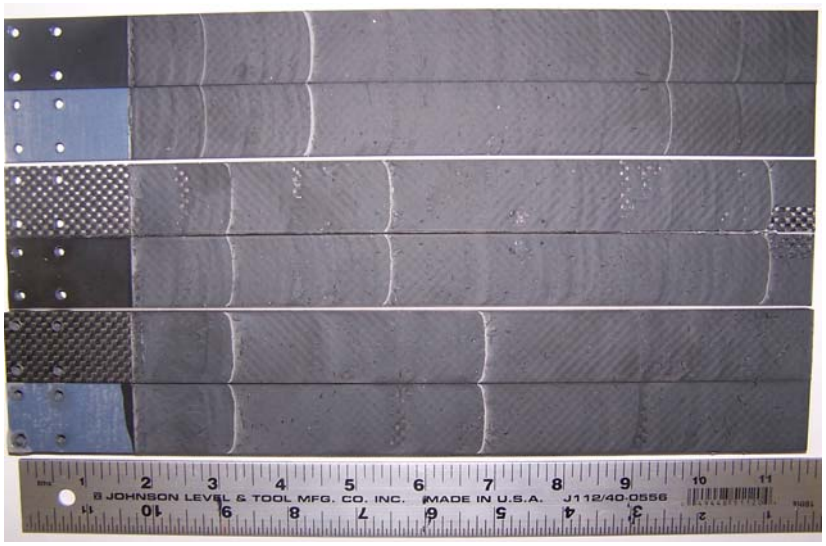

Figure 5.3. Fracture surfaces of 11 (top), 20 (middle), and 36-ply bonded composite specimens resulting from quasi-static loading conditions.

Mean quasi-static mode I fracture energy values determined using a work-based corrected beam theory analysis method were calculated to be $2800 \pm 205\ J/m^2$, $2580 \pm 150\ J/m^2$, and $2460 \pm 200\ J/m^2$ for the 11, 20, and 36-ply bonded composite specimens respectively. Additionally, the corresponding mean arrest values for the 11, 20, and 36-ply bonded composite specimens were calculated to be $167 \pm 22\ J/m^2$, $237 \pm 39\ J/m^2$, and $149 \pm 8\ J/m^2$ respectively. It should be noted that the results presented for the 20-ply bonded composite specimens are associated with one test specimen only, while the 11 and 36-ply results have been averaged over the results obtained from three different specimens. Although tests were conducted on several different 20-ply specimens, most resulted in interlaminar composite failure, thus preventing evaluation of adhesive fracture

behavior. Such behavior was observed in a variety of tests on the 20-ply specimens in several different test configurations; however, no reasoning has been determined for this behavior.

A significant aspect of the results is that the arrest fracture energy values are approximately six to nine percent of the corresponding critical fracture energy values. This is undoubtedly due to the unstable nature of the adhesive studied, often resulting in crack jumps in excess of 60mm, as well as the rate-dependent, or viscoelastic, nature of the adhesive, which will be discussed later in this thesis. Due to the lack of measured data points, an average critical energy release rate approach was incorporated [2] in an attempt to account for the possible dynamic effects resulting from the rapid crack propagation observed in these tests. This concept was used to describe the mode I quasi-static fracture behavior of the DCB specimens in an average sense and can be described using the following inequality:

$$\mathcal{G}_{Ic}^{(avg)} \leq \frac{U_2 - U_1}{A_2 - A_1} \leq \frac{\Delta\left(P_c - P_a\right)}{2b\left(a_a - a_c\right)} \tag{5.1}$$

where Δ is the fixed opening displacement, b is the specimen width, and P_c, P_a, a_c, and a_a are the load and crack length values associated with crack initiation and arrest respectively. In other words, this average fracture energy can be thought of as the change in stored energy divided by the change in crack length, and essentially fracture area, for a particular fracture event. This concept is better illustrated in Figure 5.4.

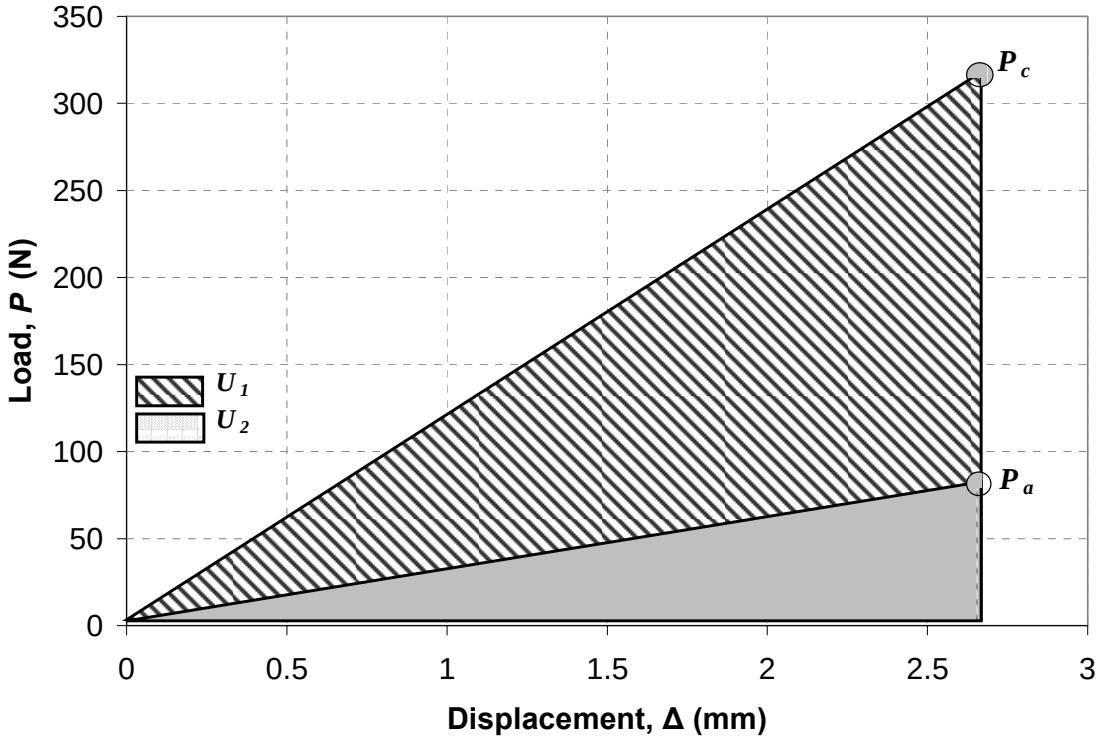

Figure 5.4. Load vs. displacement trace for DCB specimen illustrating energy method approach.

Average results reveal critical mode I energy release rate values of $780 \pm 30\ J/m^2$, $855 \pm 25\ J/m^2$, and $650 \pm 20\ J/m^2$ for the 11, 20, and 36-ply bonded specimens respectively. It is clear that these average values are only a small fraction (about 25%) of the critical mode I fracture energy values for each of the various specimen configurations, and that the average fracture energies lie between the critical values, $\mathcal{G}_{Ic}$, and arrest values, $\mathcal{G}_{Ia}$, as would be expected. Similarly, the results obtained indicate that there is a small statistical difference in $\mathcal{G}_{Ic}$ amongst the specimens tested for each of the respective adherend thicknesses. Results obtained using the energy method are illustrated in Figure 5.5.

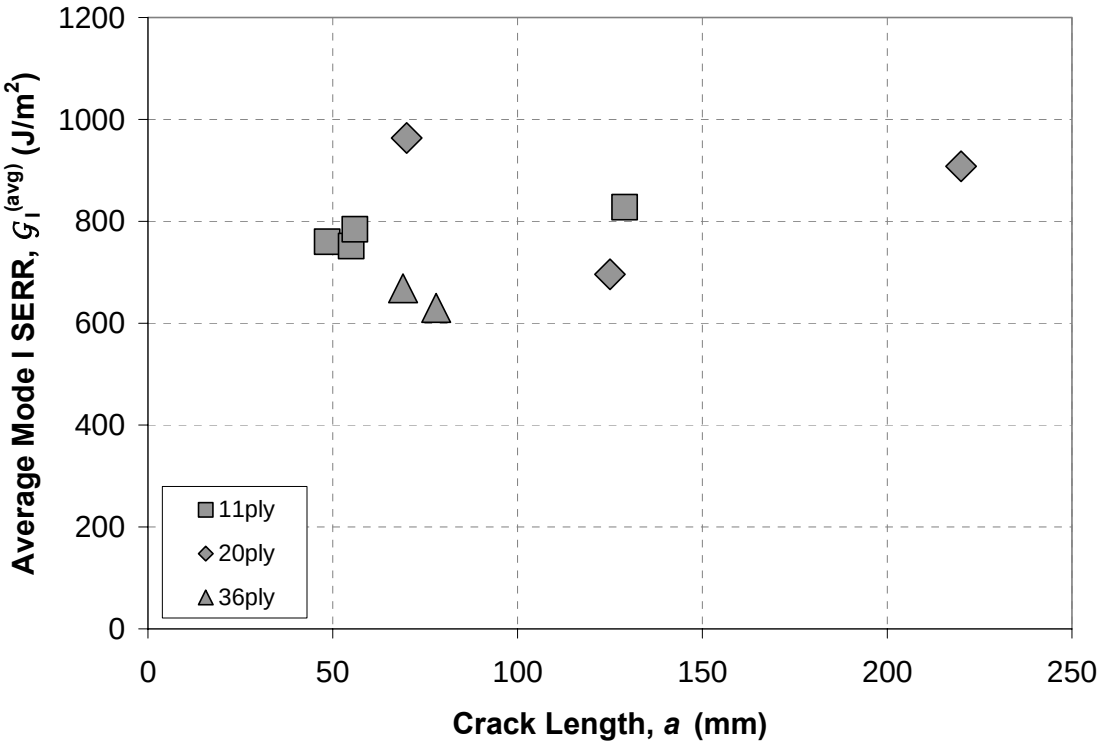

Figure 5.5. Average mode I strain energy release rate calculated using energy method for quasi-static DCB specimens.

One theory developed to explain the measured differences in $\mathcal{G}_{Ic}$ deals with the varying effective stiffness associated with the different specimen thicknesses [2]. The bending stiffness, *EI*, for the 11, 20, and 36-ply specimens were calculated to be *2.3* $N{\cdot}m^2$, *8.6* $N{\cdot}m^2$, and *48* $N{\cdot}m^2$ respectively. An explanation for the varying test results can be provided by considering the difference in local loading rates at the crack tip for the various specimens, which were subjected to the same globally applied loading rate, or specified test machine crosshead rate [3]. Due to the increased flexibility in the thinner (11-ply) specimens, a larger plastic zone is generated at the crack tip given the increased time duration in between fracture events, which corresponds to an increase in stored

energy, thus requiring more energy to initiate crack propagation [4]. Previous work conducted on the materials studied herein has shown that the more flexible specimens do indeed develop a larger plastic zone, thus resulting in higher measured energy release rate values [2].

5.1.2: Dynamic DCB

Dynamic DCB test videos were captured via a high-speed imaging system at 250, 3000, and 9000 frames per second for test velocities of 0.01, 0.1, and 1 m/s respectively. These videos were later correlated with load-displacement traces to establish crack lengths corresponding with crack propagation events. Figure 5.6 provides images obtained from this process, and Figure 5.7 provides a summary of the various load-displacement traces obtained for a range of applied loading rates.

Due to the viscoelastic nature of the adhesive studied herein, the measured strain energy release rate values show a large dependence on the applied loading rate. As such, results indicate a decrease in fracture energy as the globally applied loading rate is increased. Figure 5.8 illustrates the results from the dynamic DCB tests. Mean dynamic fracture energy values of the 11-ply bonded composite specimens calculated using a work-based analysis method for loading rates of 0.01, 0.1, and 1 m/s were calculated to be $1570 \pm 210\ J/m^2$, $1360 \pm 115\ J/m^2$, and $970 \pm 190\ J/m^2$, respectively. Additionally, values for the 20-ply specimens for the same applied loading rates were calculated to be $1040 \pm 205\ J/m^2$, $920 \pm 270\ J/m^2$, and $670 \pm 140\ J/m^2$, respectively. Finally, values for the 36-ply bonded composite specimens for the same applied loading rates were calculated to be $1400 \pm 95\ J/m^2$, $1015 \pm 50\ J/m^2$, and $740 \pm 55\ J/m^2$, respectively.

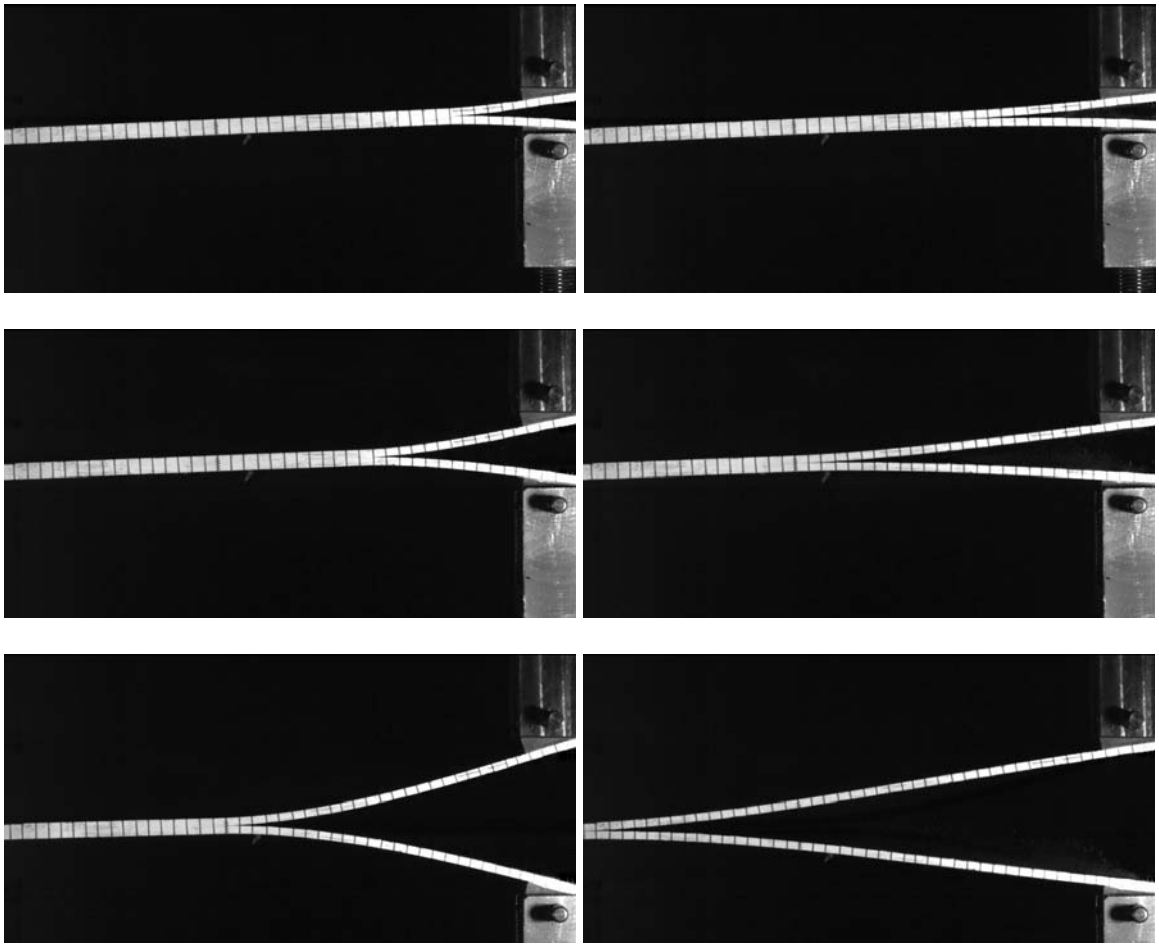

Figure 5.6. High-speed images of a 11-ply DCB specimen for a crosshead velocity of 0.1 m/s.

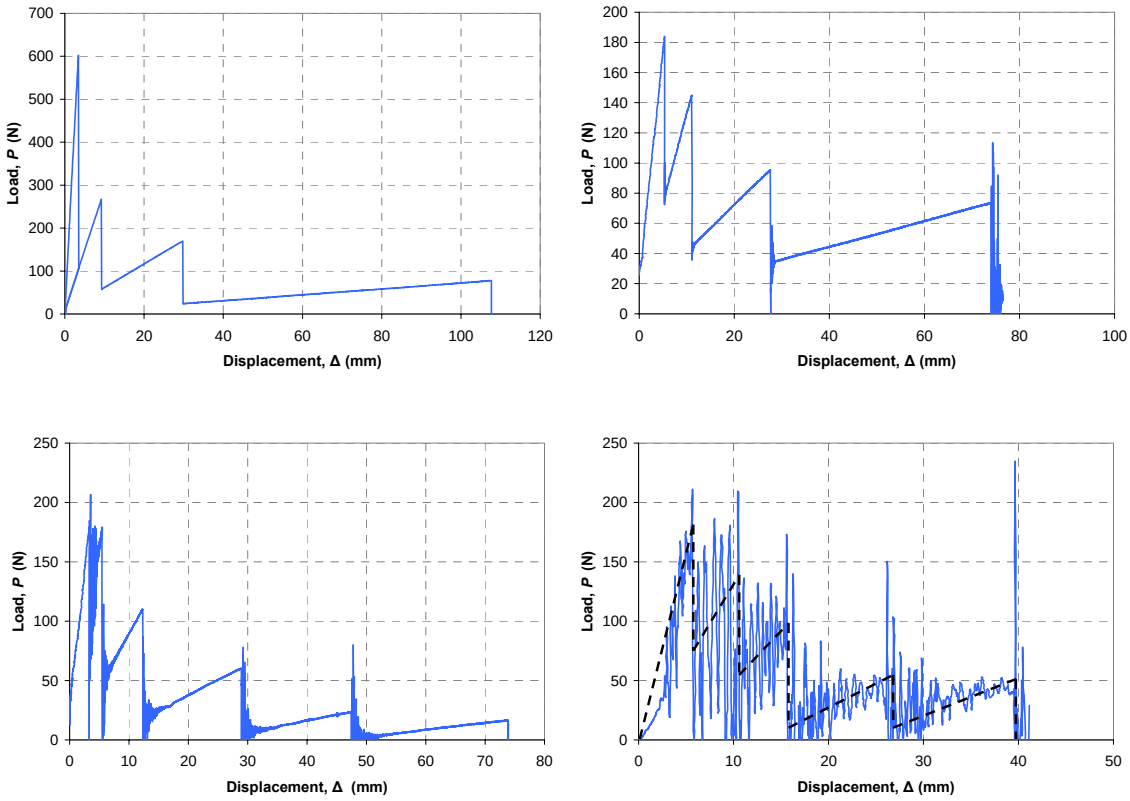

Figure 5.7. Load-displacement traces for DCB tests: 1.67×10^{-5} m/s (top-left), 0.01 m/s (top-right), 0.1 m/s (bottom-left), and 1 m/s (bottom-right).

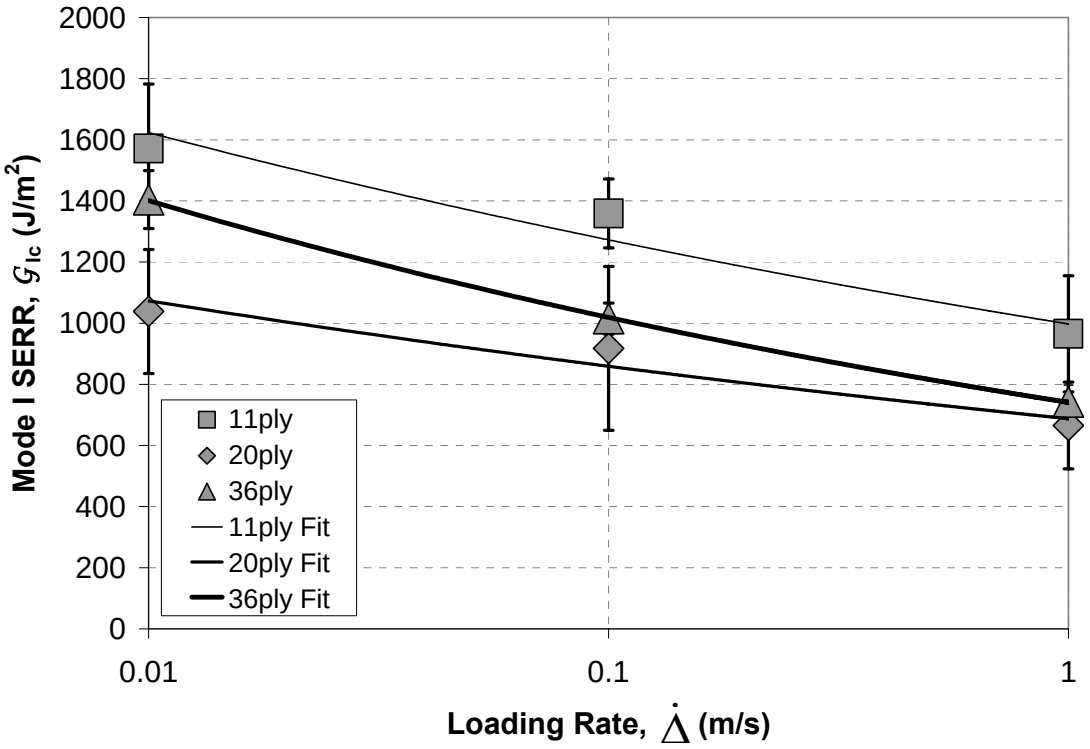

Figure 5.8. Dynamic DCB fracture energy results for 11, 20, and 36-ply bonded composites.

5.1.3: Loading Rate Effects

With mode I fracture tests conducted on 11, 20, and 36-ply bonded composite DCB specimens at a range of globally applied loading rates spanning several decades, a final results correlation can be made. Figure 5.9 illustrates the final results correlation between the quasi-static and dynamic DCB fracture tests for all of the different specimens tested. The resulting fit for all of the mode I DCB data produced using a power law relationship was determined to be $\mathcal{G}_{Ic} = 808\dot{\Delta}^{-0.107}$.

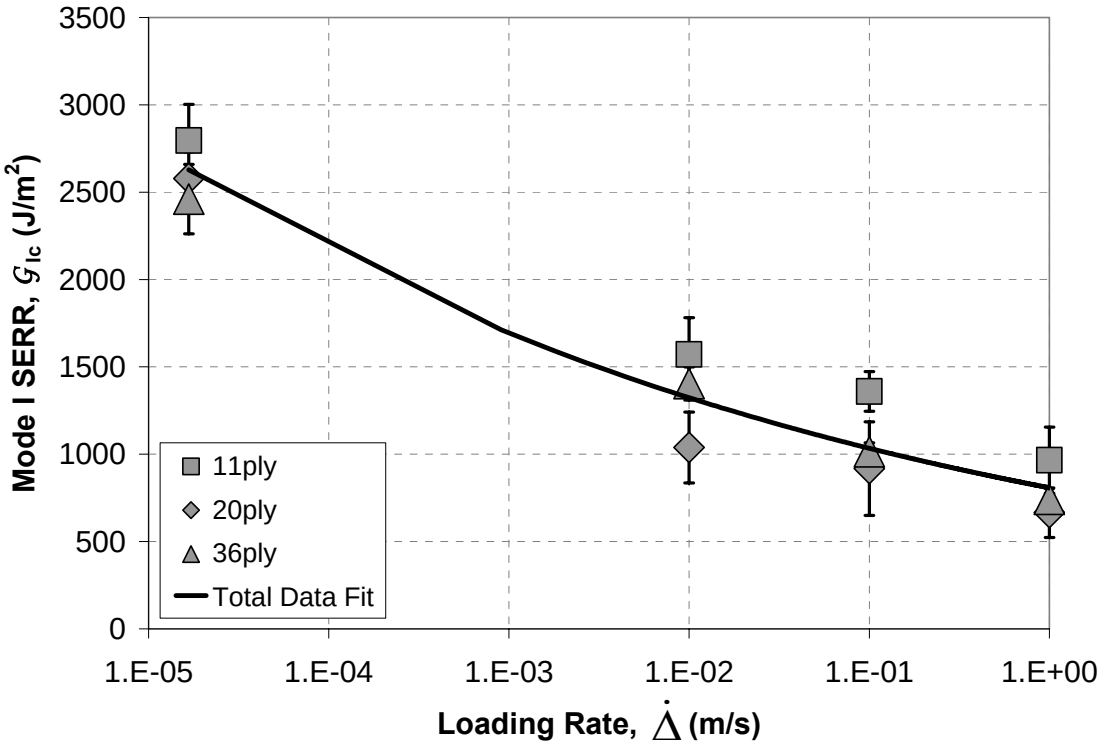

Figure 5.9. Results correlation for 11, 20, and 36-ply bonded composite DCB specimens.

Although the measured fracture energy values for the various bonded composite specimens do not completely agree with one another as a function of the globally applied loading rate, the resulting trend characterizing the total data is quite good. However, as mentioned earlier, variations in fracture energies amongst the different specimens are most likely due to the effective stiffness differences, thus affecting the local loading rate corresponding with each of the different specimens. In order to account for such discrepancies, an attempt has been made at comparing the different specimens via an effective crack tip loading rate. In fracture mechanics, the effective crack tip loading rate, dK/dt, is often used, where K is the stress intensity parameter. Since the strain energy release rate, $\mathcal{G}$, is a more common fracture parameter for adhesive joints involving

dissimilar materials, a similar comparison can be made by using $d\sqrt{\mathcal{G}}/dt$ instead. This relationship can be described as: $d\sqrt{\mathcal{G}}/dt = \left(\sqrt{\mathcal{G}_c} - \sqrt{\mathcal{G}_a}\right) / \left(t_c - t_a\right)$, where $\mathcal{G}_c$ and $\mathcal{G}_a$ are the critical and arrest energy release rates, respectively, and the quantity $t_c - t_a$ represents the total elapsed time between fracture events, or time to failure. Pohlit *et al.* [6] made use of such a parameter when comparing the same materials studied herein with those subjected to a mode I fracture condition via the use of a driven wedge specimen. By making use of a local crack tip loading rate, $d\sqrt{\mathcal{G}}/dt$, such a parameter could be used to account for the varying specimen geometries and stiffness.

Another way to interpret this concept would be to consider the mechanical testing processes implemented for the purpose of characterizing material behavior in order to aid in the automotive design process. When comparing test geometries from a coupon to sub-component level, such as compact tension specimens [5], bonded composite joints studied for the purpose of this thesis, and larger composite secondary structures used in the automotive industry, the local strain rate of such configurations varies due to several factors. Some of these factors include specimen geometry as well as debond location with respect to the globally applied loading condition. For example, CT specimens and DCB specimens are both subjected to a mode I fracture condition in order to characterize $\mathcal{G}_{Ic}$ for a given material. However, due to the high stiffness of a CT specimen and the relatively flexible adherends of the DCB specimens studied herein, the local crack tip loading rate is effectively different. Similarly, the performance of a DCB specimen will not necessarily be indicative of that which will be observed in a bonded tube

configuration due to this same reasoning. Figure 5.10 illustrates the results of this approach relative to the DCB specimens. The resulting fit for all of the mode I DCB data produced using a power law relationship was determined to be $\mathcal{G}_{Ic} = 1928\left(\frac{d\sqrt{\mathcal{G}}}{dt}\right)^{-0.104}$.

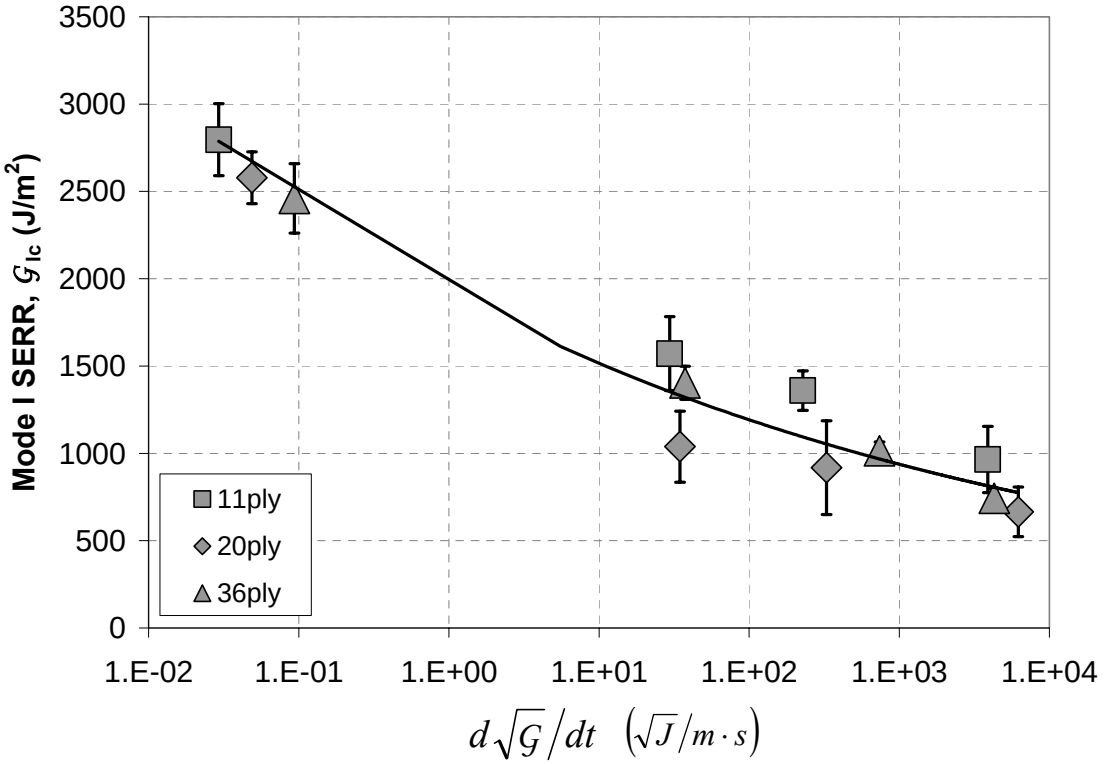

Figure 5.10. $\mathcal{G}_{Ic}$ vs. $d\sqrt{\mathcal{G}}/dt$ for 11, 20, and 36-ply bonded composite DCB specimens.

5.1.4. Comments

All double cantilever beam specimens tested illustrated a strong rate dependence, and as such, have mode I fracture energy values that decrease as a function of the applied loading rate. Results reported herein correspond with cohesive failures within the adhesive layer in order to properly characterize the fracture behavior of the adhesive in question. With static $\mathcal{G}_{Ic}$ values ranging between *2450* and *2800 J/m^2*, dynamic mode I

fracture energy values dropped steadily as a function of applied loading rate, resulting in dynamic $\mathcal{G}_{Ic}$ values ranging between *665* to *995 J/m*^{2}. Furthermore, all DCB specimens tested exhibited extreme instability in the form of stick-slip crack propagation. With crack jumps of over 50mm occurring in many of the specimens tested, the measurement of only two to four data points per specimen was possible. Additionally, such large crack jumps resulted in what are believed to be exceedingly low arrest values. While some researchers suggest that load data for dynamic tests is too erratic to be incorporated in dynamic fracture analyses [7-8], the use of a high-frequency response piezoelectric load cell combined with high-speed camera imaging has allowed for quite accurate load determinations to be used in a work-based analysis method.

5.2: Driven Wedge

Figures 5.11 *a*, *b*, and *c* show the variation of the fracture energy, $\mathcal{G}_c$, as a function of position along the crack front, which spans the width of each specimen for the 11, 20, and 36-ply specimens respectively for a specified crack length of 25mm. It should be noted that the assumption of a straight crack front was made. As such, significant drops in J are noticed near the specimen edges, which would not be the case if a more realistic geometric representation of the crack front had been utilized. A more realistic thumbnail-shape could certainly be studied; however, for simplicity, this has not been studied herein.

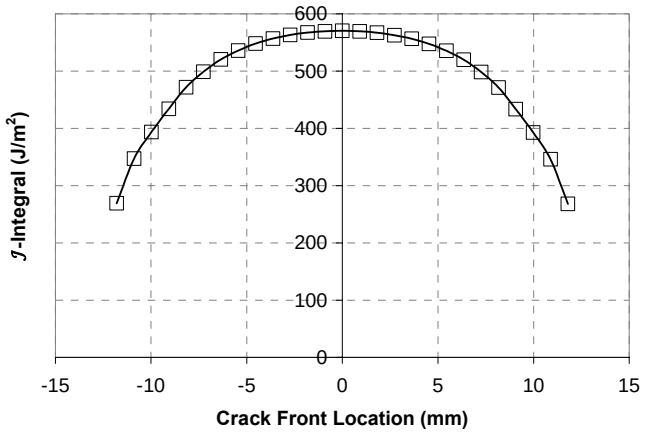

(*a*)

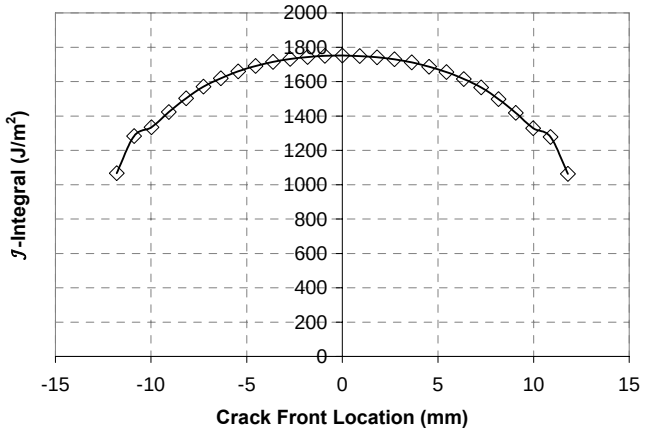

(*b*)

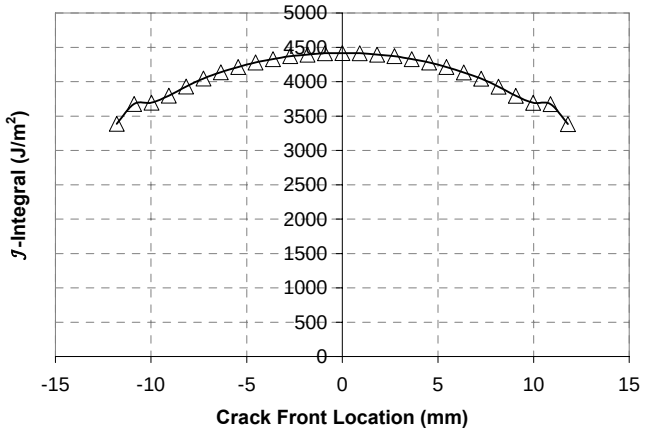

(*c*)

Figure 5.11. Crack front fracture energy profiles for (*a*) 11-ply, (*b*) 20-ply, and (*c*) 36-ply driven wedge test FEA specimens for a specified crack length, a = 25mm.

Although not shown in Figure 5.11 to more clearly illustrate the resulting thumbnail-shape distribution across the crack front, beam theory results were consistently higher than the mean values obtained via FEA, which is to be expected as corrections for shear and root rotation at the crack tip are not included in simple beam theory. For the illustrations depicted in Figure 5.11, ratios of the beam theory-to-FEA results, $\mathcal{G}_{SBT}/\mathcal{G}_{FEA}$, were determined to be about 1.7, 2.4, and 4.2 for the 11, 20, and 36-ply specimens respectively for a specified crack length of 25mm. These correction factors were obtained for each of the three different specimen geometries over a range of crack lengths by using the established $\mathcal{G}_{SBT}/\mathcal{G}_{FEA}$ ratio. It should be noted that a mean fracture energy, $\mathcal{G}_{FEA}$, was calculated due to the variations across the width of each specimen. The calculated average value was then used in the calculation of the associated correction factors.

As expected, this parameter decays to unity for longer crack lengths where the influence of shear and root rotation on the results becomes negligible. However, it should be noted that the crack lengths at which this occurs differ amongst specimens due to the variations in effective specimen stiffness. The resulting trends are illustrated in Figure 5.12, and a series of snap-shots for sequential time-step increments of displacement results in the out-of-plane direction obtained from the FEA simulation on an 11-ply specimen with a specified crack length of 20mm are provided in Figure 5.13.

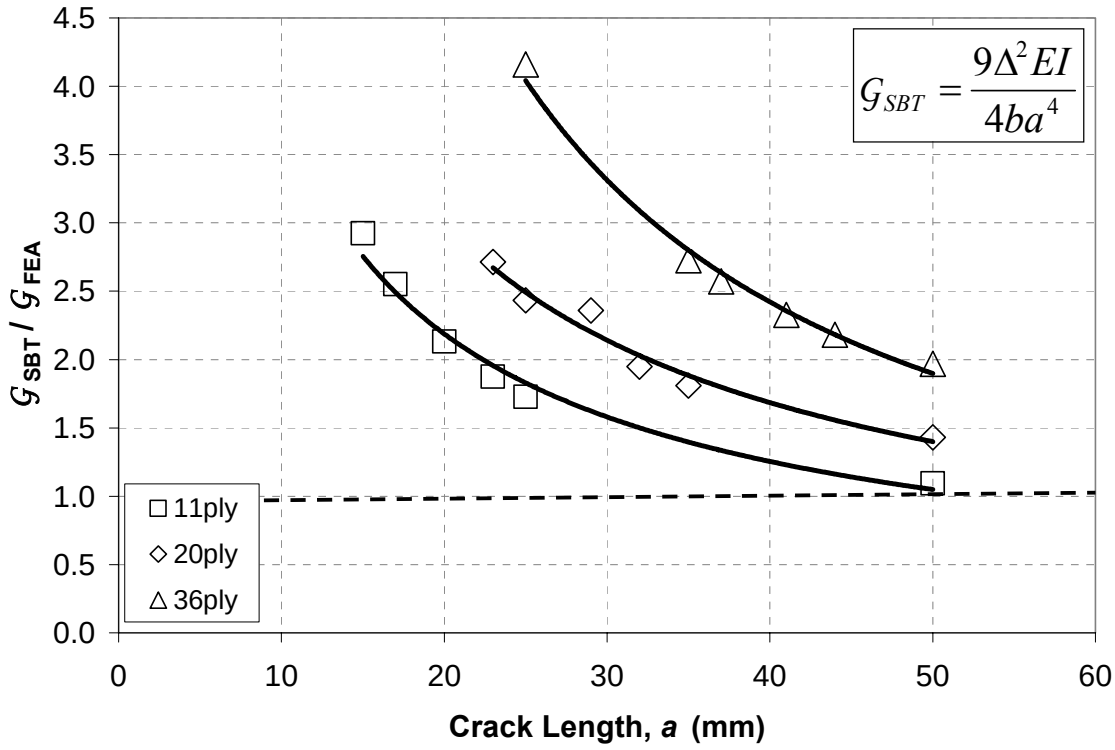

Figure 5.12. Fracture energy ratio, $\mathcal{G}_{SBT}/\mathcal{G}_{FEA}$, vs. crack length, a, for driven wedge specimens.

The established trends were then used to scale the previously collected experimental data. For a given crack length observed under experimental test conditions, a correction factor, $\mathcal{G}_{SBT}/\mathcal{G}_{FEA}$, could be calculated based on the trends depicted in Figure 5.12. This correction factor was then applied to the corresponding data point by dividing the experimentally measured fracture energy calculated using SBT by the associated value of $\mathcal{G}_{SBT}/\mathcal{G}_{FEA}$. The final scaled experimental results for the driven wedge experiments are illustrated in Figure 5.14.

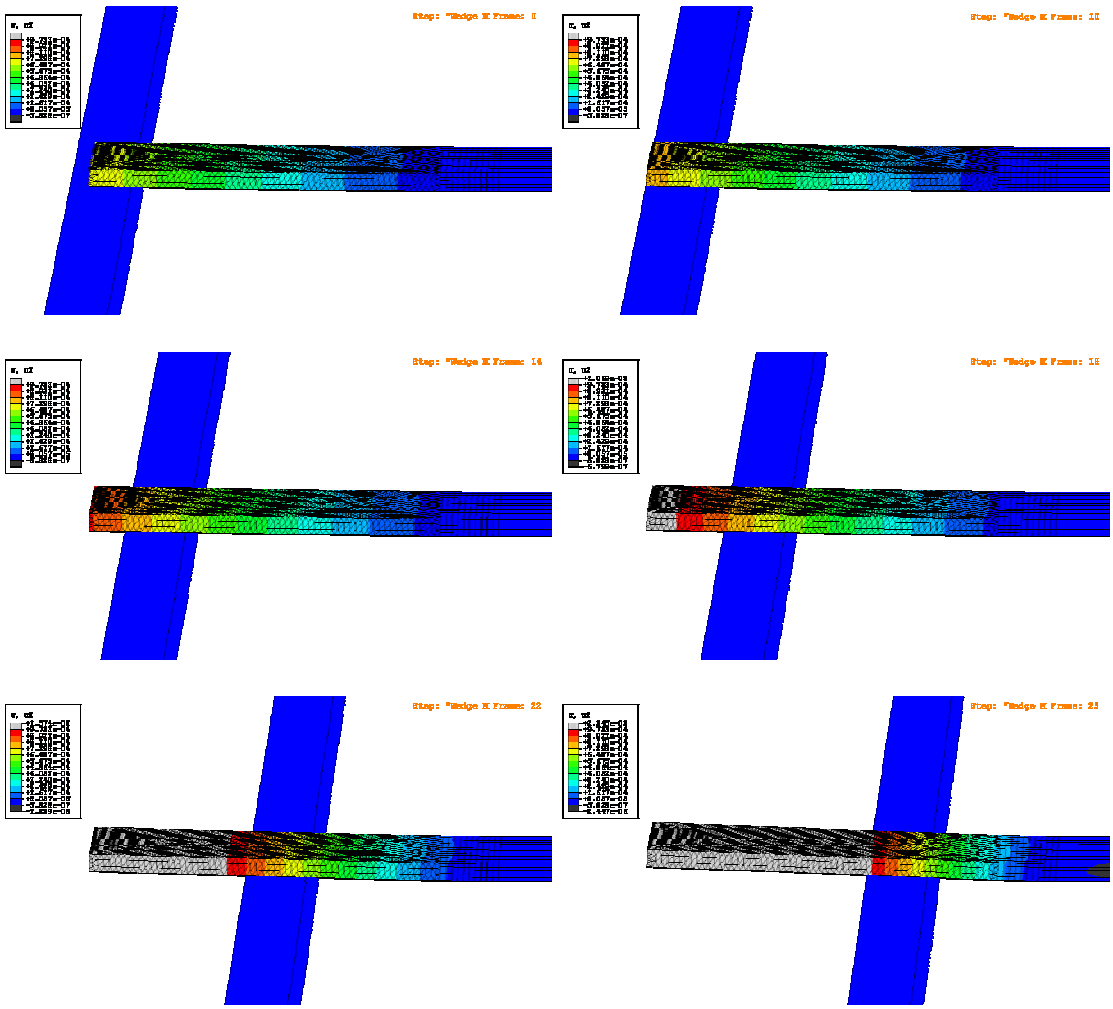

Figure 5.13. Sequential time-step incremental snap-shots of resulting FEA displacements for 11ply driven wedge specimen with a specified crack length of 20mm.

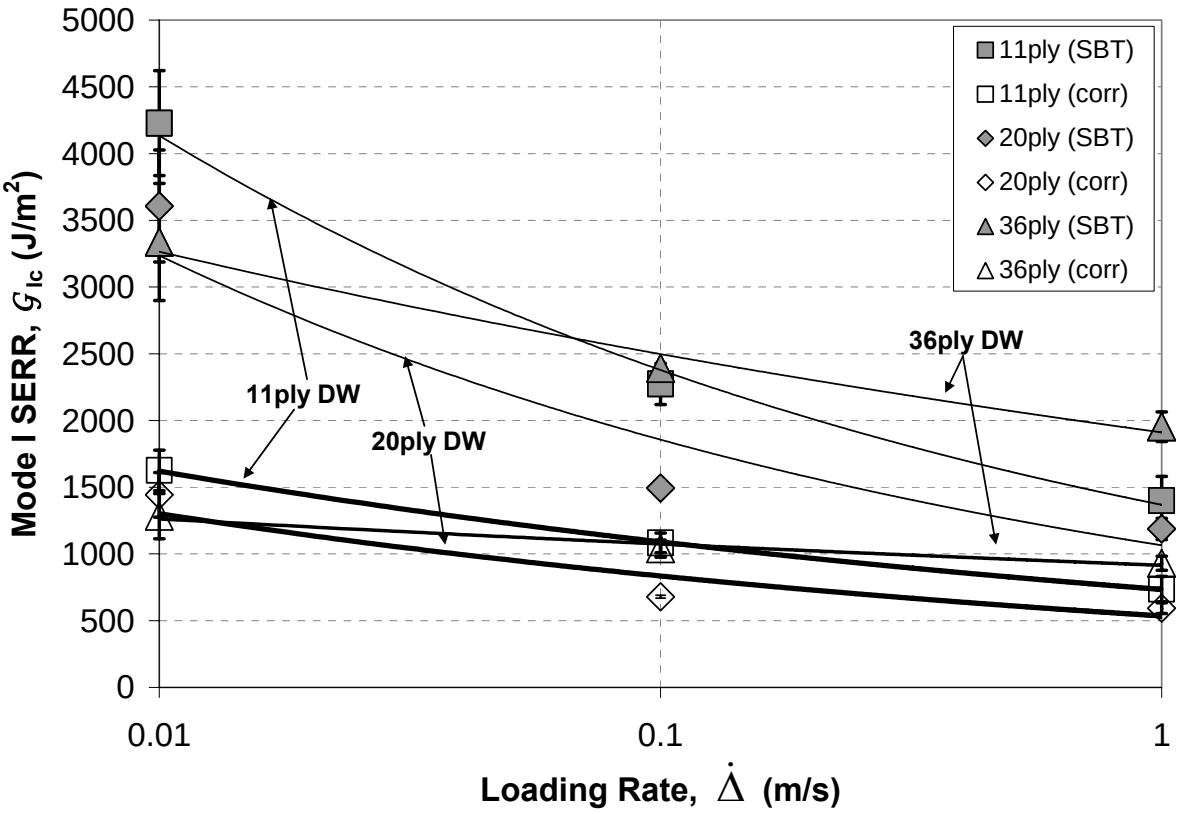

Figure 5.14. Uncorrected (shaded symbols) and corrected (open symbols) experimental fracture energy values as a function of applied loading rate for all driven wedge test specimens.

5.2.1: Driven Wedge & DCB Results Comparison

Because of the different loading kinetics, attempts to compare results from DCB and driven wedge tests must recognize the effective rate of loading at the crack tip. As mentioned earlier, in fracture mechanics, the effective fracture loading rate, dK/dt, is often used, where K is the stress intensity parameter. Since the strain energy release rate is a more common fracture parameter for adhesive joints, we have chosen to compare a similar quantity, $d\sqrt{\mathcal{G}}/dt$, as this quantity is linear with load just the same as dK/dt. Under constant crosshead rate $\left(\dot{\Delta} = \text{constant}\right)$ conditions, $d\sqrt{\mathcal{G}}/dt$ is time-independent for

a stationary crack in DCB specimens, although this quantity depends on crack length for subsequent crack arrest positions according to $d\sqrt{\mathcal{G}}/dt \propto 1/a^2$. On the other hand, for the driven wedge test, constant crosshead $(\dot{a} = \text{constant})$ testing for a stationary crack also results in $d\sqrt{\mathcal{G}}/dt \propto 1/a^2$, but now $\dot{a}$ is a constant, so $d\sqrt{\mathcal{G}}/dt$ is no longer independent of time during an individual loading event.

Full rate correlation of DCB and driven wedge tests might require a more complete analysis of the viscoelastic response of the materials under the specific loading conditions. Nonetheless, for the purposes of this thesis, comparison plots are made using the relationship previously described in section 5.1.3 of this thesis. From the experimental data, the dependence of crack jumps on the crosshead rate for the various specimens tested was established. Figure 5.15 further illustrates this concept of the need to account for the crack tip loading rate for a given specimen in both the DCB and driven wedge test configuration for a prescribed applied, or global, loading rate [9]. As a result, the fracture energies for the two different specimen configurations can now be compared using this method as illustrated in Figure 5.16. A fit for each of the two test geometries has been provided through the total data encompassing the results obtained for the 11, 20, and 36-ply specimens. Although not exact, it is shown that the driven wedge test does provide a good correlation with results obtained using the standardized double cantilever beam configuration. Similarly, by characterizing the fracture behavior using a local loading rate approach, $d\sqrt{\mathcal{G}}/dt$, instead of a global applied loading rate, $\dot{\Delta}$, the resulting data appears to provide a better correlation amongst the different tested specimens.

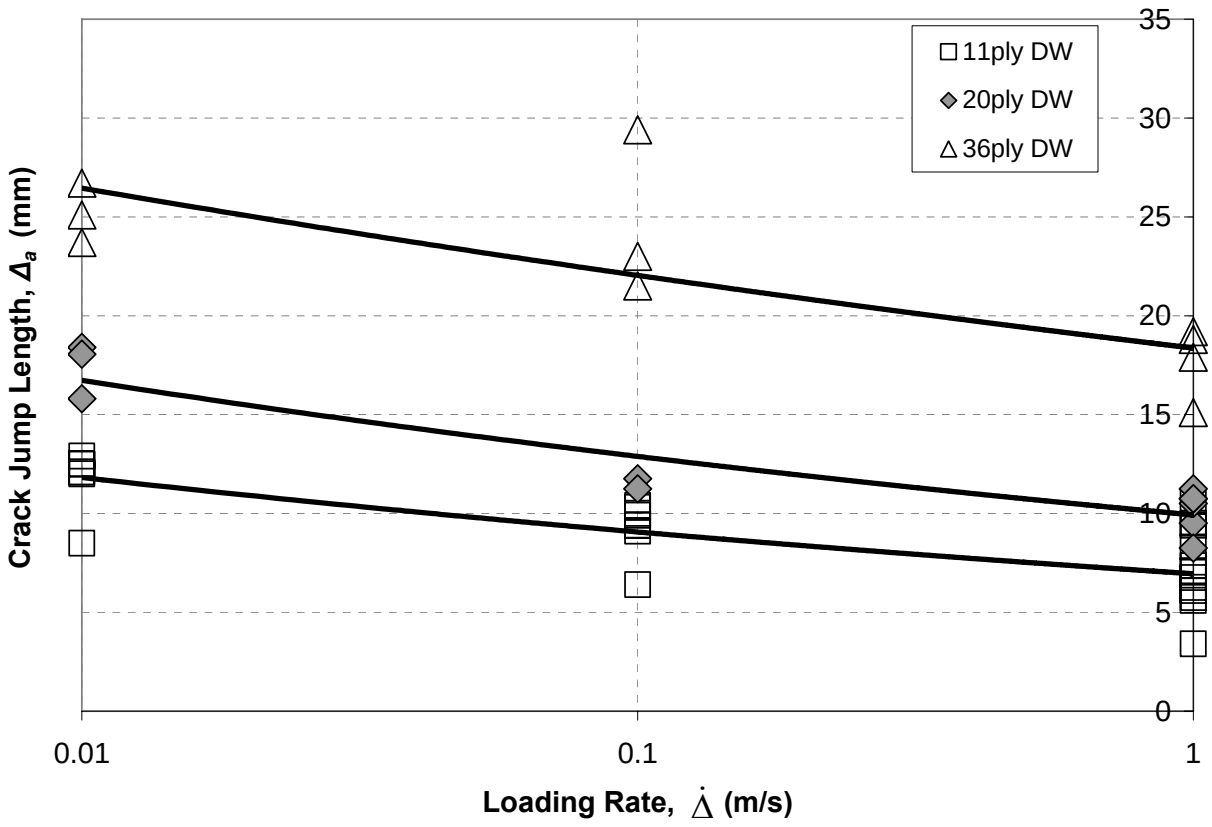

Figure 5.15. Crack jump length vs. crosshead rate for driven wedge specimens.

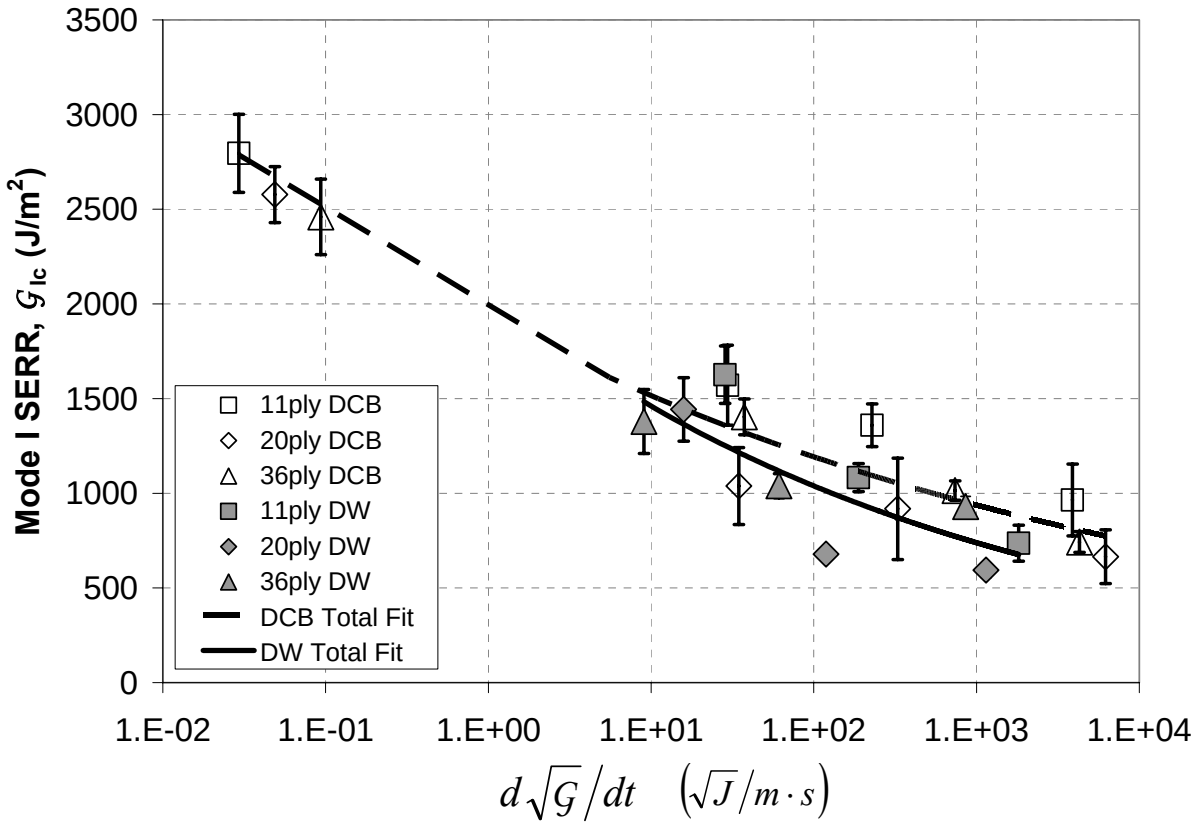

Figure 5.16. Fracture energy comparison for driven wedge and DCB specimens using $d\sqrt{\mathcal{G}}/dt$.

5.2.2. Comments

The driven wedge method is especially useful for systems exhibiting pronounced stick-slip behavior. In comparisons with specimens tested in standard DCB fashion, initiation values of fracture energy were found to compare reasonably well across the range of applied loading rates studied (up to 1m/s), with percentage differences ranging from as little as 1% up to 25% in some instances for a given specimen geometry and test velocity. In general, initiation values obtained from the driven wedge tests were slightly lower than those obtained via the standard DCB tests. Furthermore, arrest values obtained from the driven wedge tests were very consistent across the range of applied

loading rates studied, which is attributable to the consistency associated with the crack jump lengths observed in this experimental procedure. In addition, arrest values of fracture energy for the driven wedge test were found to be significantly greater than the DCB tests for a given test velocity due to the much more pronounced stick-slip behavior present in the traditional mode I DCB test specimen configuration. This can be attributed to the fact that there is more kinetic energy available to drive the crack beyond the point of arrest suggested by static analysis, a concept discussed previously in Chapter 2 of this thesis. Tests conducted over a range of five decades in crosshead rate showed a clear dependence of initiation fracture energies on rate, but an insignificant dependence of arrest values on crosshead rate.

5.3: Compact Tension

Due to the preliminary findings in the bonded joint experiments with regard to the cohesive failures within the adhesive layer illustrating dramatic stick-slip behavior, it was believed that the CT tests would exhibit a similar rate dependence, thus requiring tests to be conducted over a range of test velocities. Tests were conducted at room temperature; however, in a coordinated study [5], subambient test conditions were utilized to determine the validity of making use of the time-temperature-superposition principle.

Figure 5.17 illustrates the measured fracture toughness, K_{Ic}, which has been converted to fracture energy, $\mathcal{G}_{\mathrm{Ic}}$, using a plane strain criteria in order to allow for direct comparisons between bulk adhesive and bonded joint geometries later on, of the CT specimens conducted at room temperature. The plane strain relationship utilized for this conversion is characterized as:

$$\mathcal{G}_{Ic} = \frac{K_{Ic}^{\,2}\left(1-\nu^2\right)}{E} \tag{5.2}$$

where ν and E are the Poisson's ratio and elastic modulus of the adhesive.

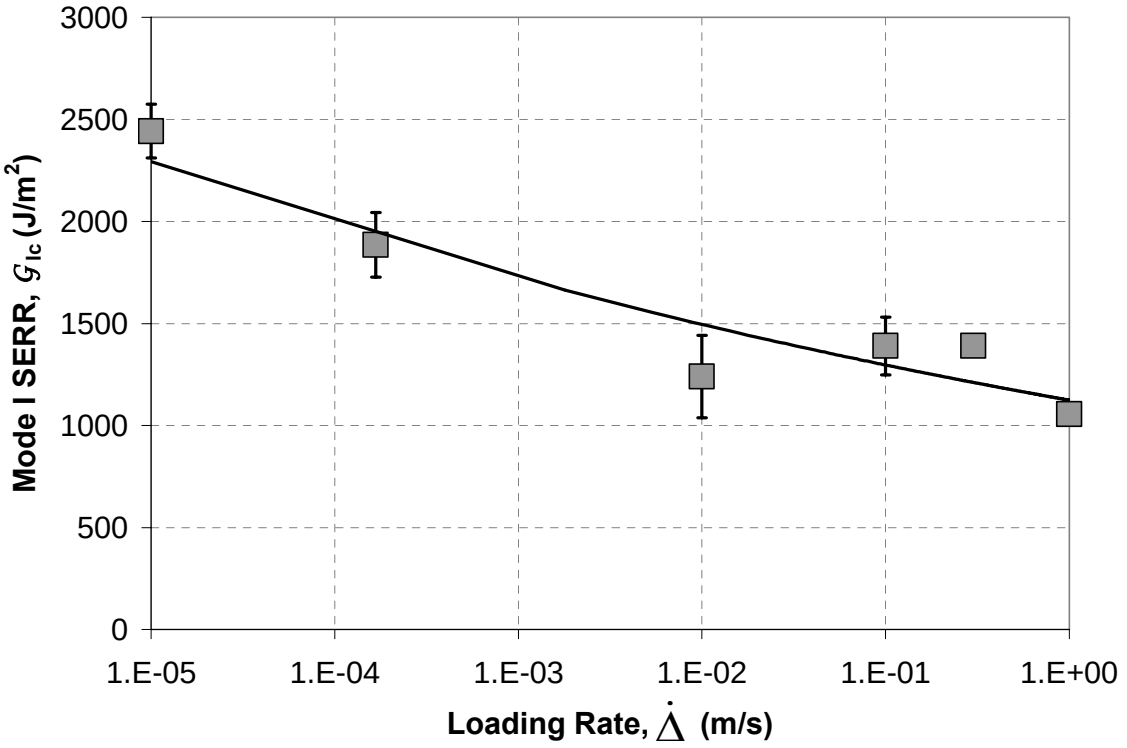

Figure 5.17. Average CT measured fracture energy values as a function of loading rate. Error bars for two highest rates (i.e. 0.3 and 1 m/s) are so small that they are hidden behind respective data points.

It should be noted that results for the three lowest rates (i.e. $1x10^{-5}$, $1.7x10^{-4}$, and 0.01 m/s) were obtained from a coordinated study [5]. A clear trend is observed in the drop in fracture toughness values in the range of 10^{-5} m/s to 1 m/s. The resulting trend developed using a standard power law relationship was determined to be $\mathcal{G}_{Ic} = 1124\dot{\Delta}^{-0.062}$.

At the three slower rates, extensive stress whitening was observed in the failed specimens [5], and the plane strain fracture toughness, K_{Ic}, was determined from the intercept of a 95% slope with the load trace [10]. Brittle failures were common at the higher loading rates, and the resulting fracture toughness and energy values were calculated using the peak load.

5.3.1. Dynamic Mechanical Analysis

Small single-cantilever beam specimens were cut from the cured adhesive plaques and were examined using the DMA method to determine the glass transition temperature of the adhesive. The glass transition temperature, T_g, was determined to be about 100˚C and 125°C, based on the peak of the *E"* and tan δ curves, respectively, at a frequency of 1 Hz. The DMA results for a typical sample are shown in Figure 5.18.

The dynamic moduli results obtained over a range of temperatures and at frequencies of 0.1, 0.2, 0.5, 1, 2, 5, 10, and 20 Hz were shifted, thus establishing the corresponding shift factors to be used in the generation of a master curves for the DMA measured properties. Figure 5.19 illustrates the resulting shift factor plot for the dynamic moduli. Some differences were seen in the shift factors, with the values obtained from the loss moduli showing more erratic behavior. A linear relationship, $\log(a_T) = -0.1863T + 5.65$, was used to fit the data for subsequent use. Figure 5.20 provides the resulting master curves for both dynamic moduli, as well as the tan δ results.

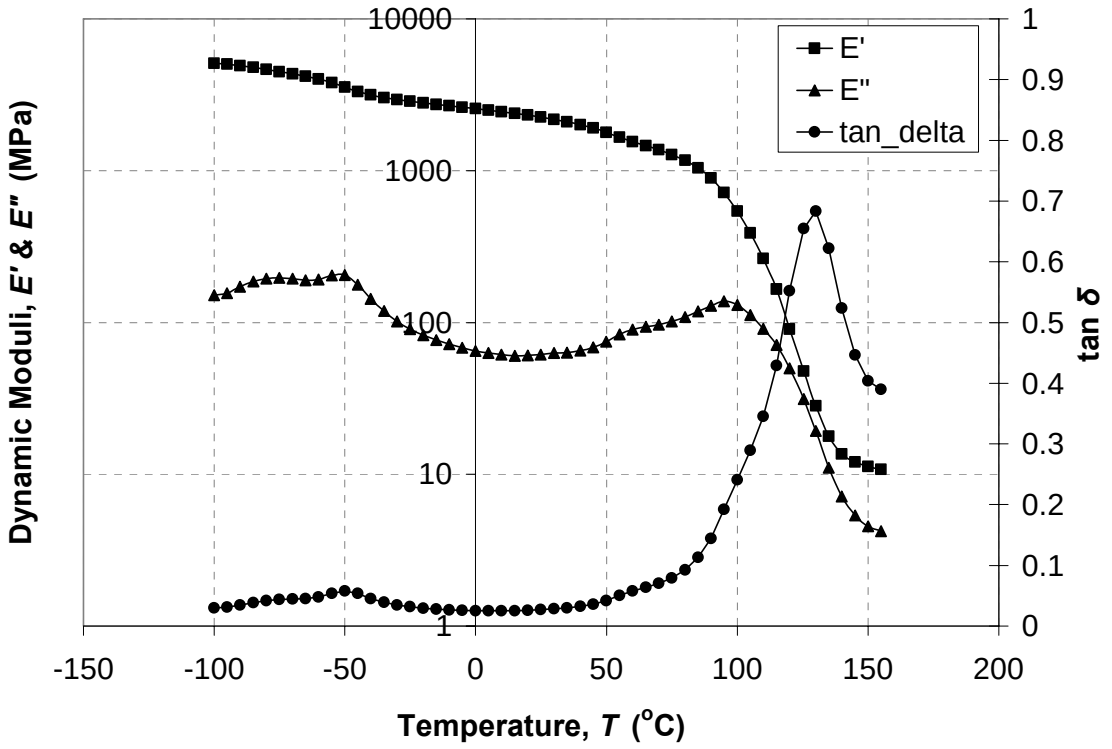

Figure 5.18. DMA results at 1 Hz for bulk adhesive sample measured with a temperature sweep.

Figure 5.21 illustrates a fracture energy master curve (T_{ref} = 25˚C) obtained by combining the room temperature and sub-ambient temperature test results. The sub-ambient temperature data were collected in a coordinated study [5] as previously mentioned, and the results have been shifted to their corresponding test rates by using the shift factors developed according to Figures 5.19 and 5.20. In short, these results have been shifted by a factor of 5°C/decade rate of test. Tests conducted at slower rates at temperatures as low as -115°C showed slightly lower fracture energy values than obtained at room temperature, but based on these limited results, a glassy plateau appears to be developing. These tests conducted at temperatures of -115°C to -40°C and at several displacement rates showed no specific trends and averaged about 730 J/m^2, which

is less than results produced from the high rate tests conducted at room temperature. Finally, according to Figure 5.21, the trends observed at sub-ambient temperatures for relatively low applied loading rates appear to be consistent with the use of TTSP, implying that this may be a useful method for characterizing this material. The data for the fracture energy master curve were fit using a standard power law, and the resulting relationship was determined to be $\mathcal{G}_{Ic} = 1281\dot{\Delta}^{-0.0365}$.

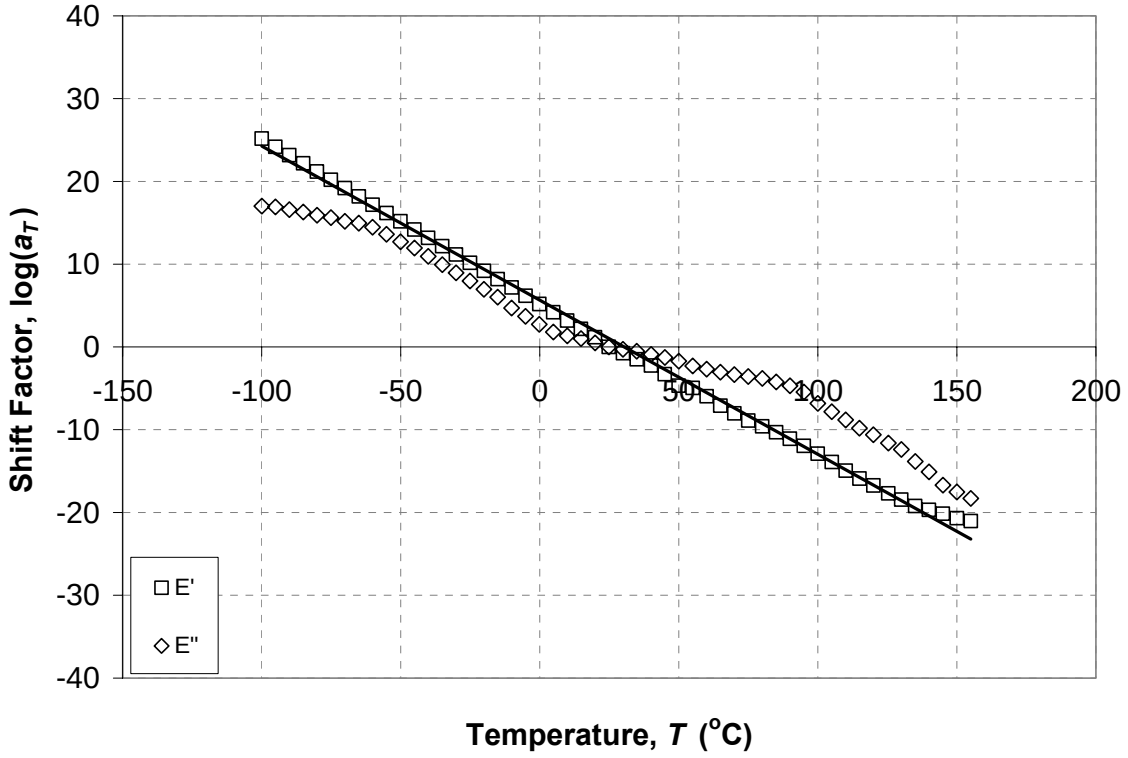

Figure 5.19. Shift factor plot for dynamic moduli results for DMA test on bulk adhesive.

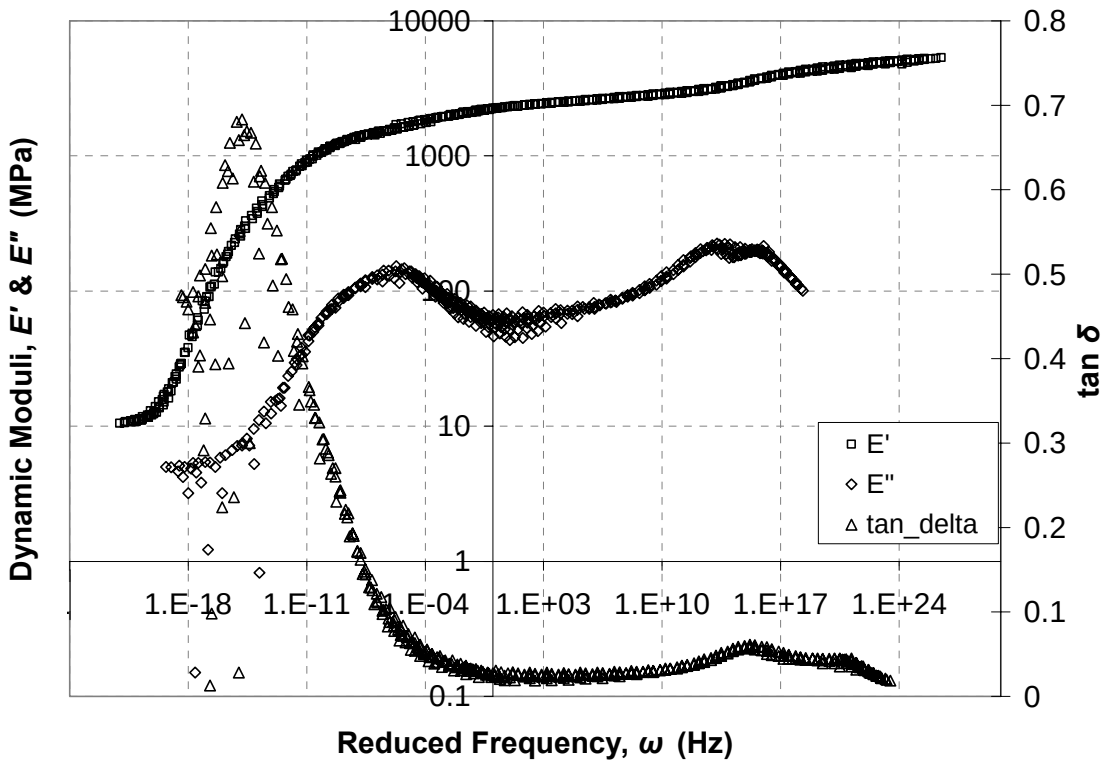

Figure 5.20. Master curves generated from DMA test results on bulk adhesive (T_{ref} = 25°C).

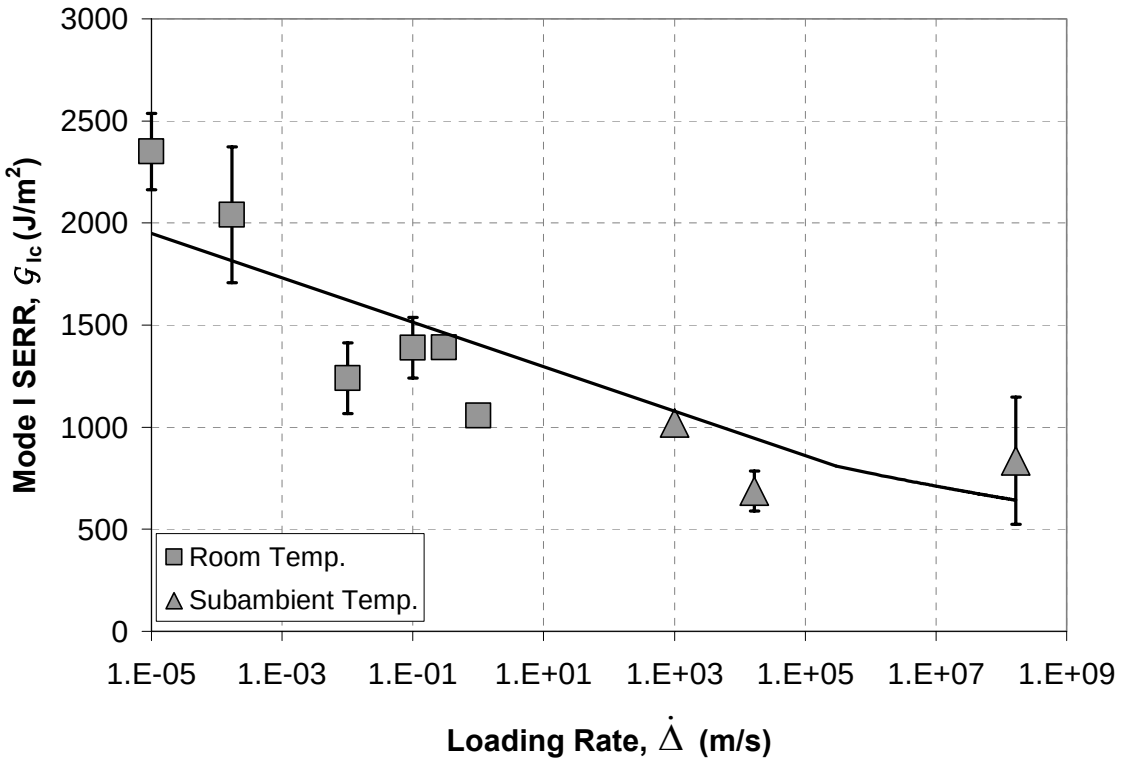

Figure 5.21. Fracture energy master curve obtained from various test velocity data collected at room and subambient [5] temperatures. Error bars for several rates (i.e. 0.3, 1, and 1000 m/s) are not shown for the respective data points because they are hidden.

5.3.2. Correlation with DCB Tests

As mentioned earlier, a correlation has been made between the fracture results obtained from bulk adhesive CT tests and bonded DCB specimens. Instead of analyzing the fracture toughness, K_{Ic}, which is the common parameter measured for CT specimens, the strain energy release rate, $\mathcal{G}_{Ic}$, has been utilized as this is a more common fracture parameter for adhesive joints. Therefore, the fracture toughness results obtained from the CT tests presented herein have been converted to strain energy release rate, as previously mentioned, using the plane strain fracture criteria discussed previously in section 5.3.4 of this thesis. As such, results obtained from both bulk adhesive and bonded joint

geometries have proven to yield similar trends as a function of applied loading rate. Figure 5.22 provides a summary of all CT and DCB test data as a function of applied loading rate.

Similar to the driven wedge specimen geometry, the CT specimen exhibits different loading kinetics than that of the standard DCB specimen. As such, attempts to compare results from CT and DCB tests must recognize the effective rate of loading at the crack tip. When considering the nature of each type of test specimen, it is clear that the CT specimens experience a very short time to failure due to the high relative stiffness of such a test specimen. In contrast, the bonded beam specimens experience rather large deformations and thus undergo a much larger period of loading due to their relative flexibility. Therefore, the concept of characterizing the fracture performance as a function of $d\sqrt{\mathcal{G}}/dt$ may provide a more accurate means of comparison amongst the bulk adhesive CT and bonded joint DCB specimen geometries. Therefore, the same data illustrated in Figure 5.22, but now plotted in terms of $d\sqrt{\mathcal{G}}/dt$, are shown in Figure 5.23. Additionally, a rate-dependent modulus has been utilized to correct for the viscoelastic nature of the bulk adhesive specimens subjected to the large range of applied loading rates. In doing so, there appears to be a slightly better agreement between the bulk adhesive CT results and those obtained from the bonded joint DCB tests, in particular with regard to the slope of the two best-fit curves. Overall, the rate-dependent modulus changes from 2.21 to 2.56 GPa across a range of loading rates of $1\text{x}10^{-5}$ to 1 m/s respectively. It should also be noted that both the fracture energy, $\mathcal{G}_{Ic}$, and the crack-tip

loading rate, $d\sqrt{\mathcal{G}}/dt$, have been corrected using rate dependent elastic moduli for the adhesive in question.

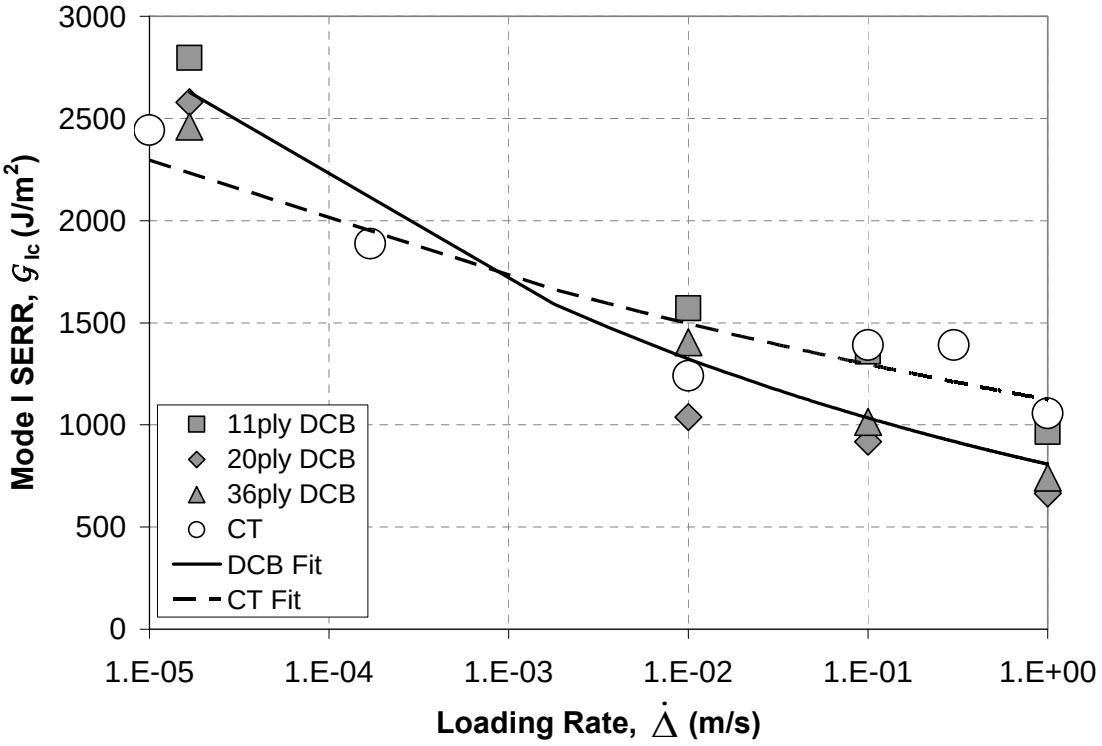

Figure 5.22. Average measured fracture energy values as a function of applied loading rate for CT and DCB tests. Error bars have been eliminated for clarity, but can be seen in figures previously included in this thesis.

The trend resulting from Figure 5.23 for the CT specimens incorporating a rate-dependent modulus was produced using a standard power law relationship and was determined to be $\mathcal{G}_{Ic} = 2317\left(\frac{d\sqrt{\mathcal{G}}}{dt}\right)^{-0.0733}$, while that for the DCB specimens was

previously provided in section 5.1.3 of this thesis, which was determined to be $\mathcal{G}_{Ic} = 1928\left(\frac{d\sqrt{\mathcal{G}}}{dt}\right)^{-0.104}$.

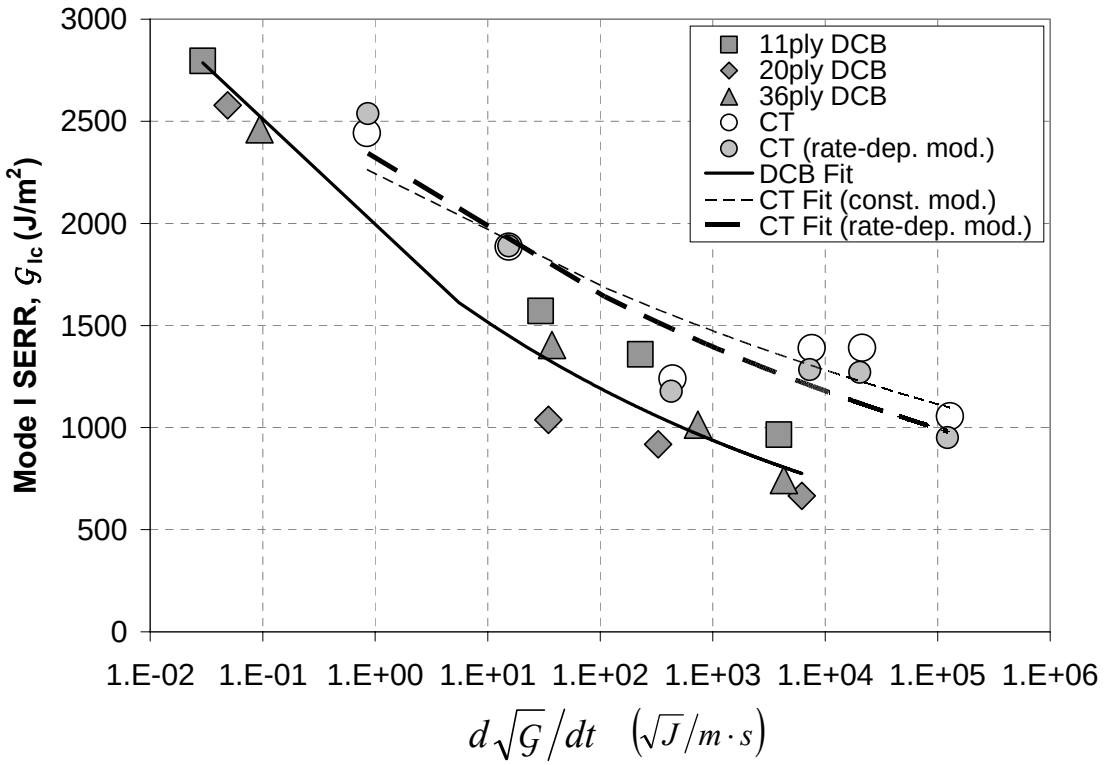

Figure 5.23. Average measured fracture energy values as a function of $\frac{d\sqrt{\mathcal{G}}}{dt}$ for CT and DCB tests. Error bars have been eliminated for clarity, but can be seen in figures previously included in this thesis.

5.3.3. Correlation with tan δ

It has been shown that viscoelastic energy may play an important role in the fracture behavior of adhesives, and the loss factor, tan δ, can sometimes be a good indicator of an adhesive's ability to withstand impact loading [11]. Relationships between tan δ and fracture energy can often be established since mechanisms responsible

for energy dissipation in the linear viscoelastic regime are expected to play a role under fracture conditions. Occasionally, this agreement can be quantified, which is somewhat surprising given the large differences in strains that occur in small-scale DMA tests when compared with common fracture experiments. In Figure 5.24, the average measured fracture energy from all CT and DCB tests conducted at room temperature is plotted as a function of tan δ for each corresponding applied loading rate. These loading rates have been used to determine the equivalent DMA test frequency, and the time to failure has been taken to be equivalent to $\pi/4$ of a cycle in an attempt to account for loading rate effects present in both types of fracture tests. The resulting relationships for the CT and DCB tests were determined to be $\mathcal{G}_{Ic} = 3660\ln(\tan\delta)+15005$ and $\mathcal{G}_{Ic} = 3075\ln(\tan\delta)+12415$ respectively.

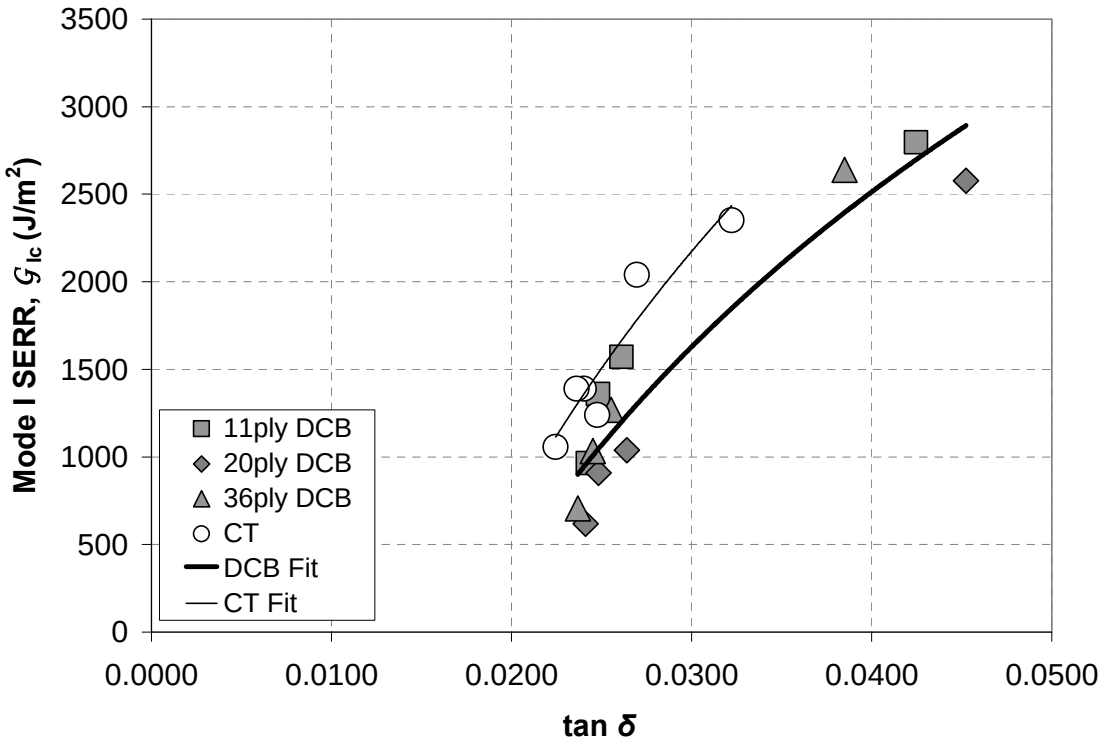

Figure 5.24. Variation of fracture energy with tan δ for CT and DCB tests.

5.3.4. Comments

The fracture properties of bulk adhesive compact tension specimens have been characterized over a range of applied loading rates to better understand how this material may behave under impact loading conditions. The measured fracture energy dropped steadily across a range of applied loading rates (up to 1 m/s), and fracture energy values were measured to drop by approximately 65% across this range. Resulting plastic zones, in the form of stress-whitened zones, were clearly present in all compact tension specimens. It is clear that these zones of fracture were reduced in size as test speeds were increased. Similarly, according to [5], this same behavior was exhibited under decreasing temperature. Upon crack propagation, smooth failure surfaces were observed, which suggests that a reduction of plastic deformation occurred as a result of the rapid crack advancement. Such results are consistent with the significant stick-slip behavior observed in fracture tests of bonded joints, as previously discussed.

Furthermore, the resulting correlation between $\mathcal{G}_c$ and tan δ for both bonded joint and bulk adhesive fracture tests is encouraging. Although standard fracture specimens such as the double cantilever beam are the norm, DMA tests are considerably easier to conduct and provide a large amount of data over a range of test frequencies and temperatures using a single specimen. While the established correlation is encouraging related to the adhesive studied herein, as well as the possibility of others, additional studies are needed to determine whether or not simpler tests, such as the use of DMA, may be substituted for traditional fracture experiments, yet still provide the insights necessary to fully characterize the fracture behavior of a particular material system.

5.4. Mixed-Mode I/II Fracture Results

Testing conducted on both the asymmetric double cantilever beam and single leg bend specimens yielded many more data points per specimen compared with the standard mode I DCB geometry, although stick-slip behavior was still observed, thus resulting in unstable crack growth. Although a limited number of tests were conducted under dynamic loading conditions due to material availability, the mixed-mode fracture characterization has been sufficiently characterized by making use of both the ADCB and SLB specimen geometries.

5.4.1 Asymmetric Double Cantilever Beam - Static

All static ADCB specimens were subjected to an applied loading rate of 1 mm/min, just as in the case of the static DCB testing. Specimens were loaded up to a point that resulted in crack initiation, at which time they were unloaded approximately to the test origin in order to determine whether or not any permanent deformation had occurred within the specimen adherends. No such deformation was observed. Specimens were then reloaded and allowed to experience crack propagation along their full length until complete fracture had occurred, thus resulting in two separate adherends. Visual crack length measurements were taken throughout the test at each crack initiation and arrest event. Sample load-displacement traces for all specimen configurations under quasi-static loading conditions are provided in Figure 5.25. Unfortunately no usable data was collected on the 20x36 specimens as these specimens typically produced interlaminar failure, which was not conducive to the fracture characterization of the adhesive in question. Although useful information regarding the mixed-mode behavior of the composite material utilized in this study can be obtained from these results, they have not

been considered with regard to the behavior of cohesive failures within the adhesive layer.

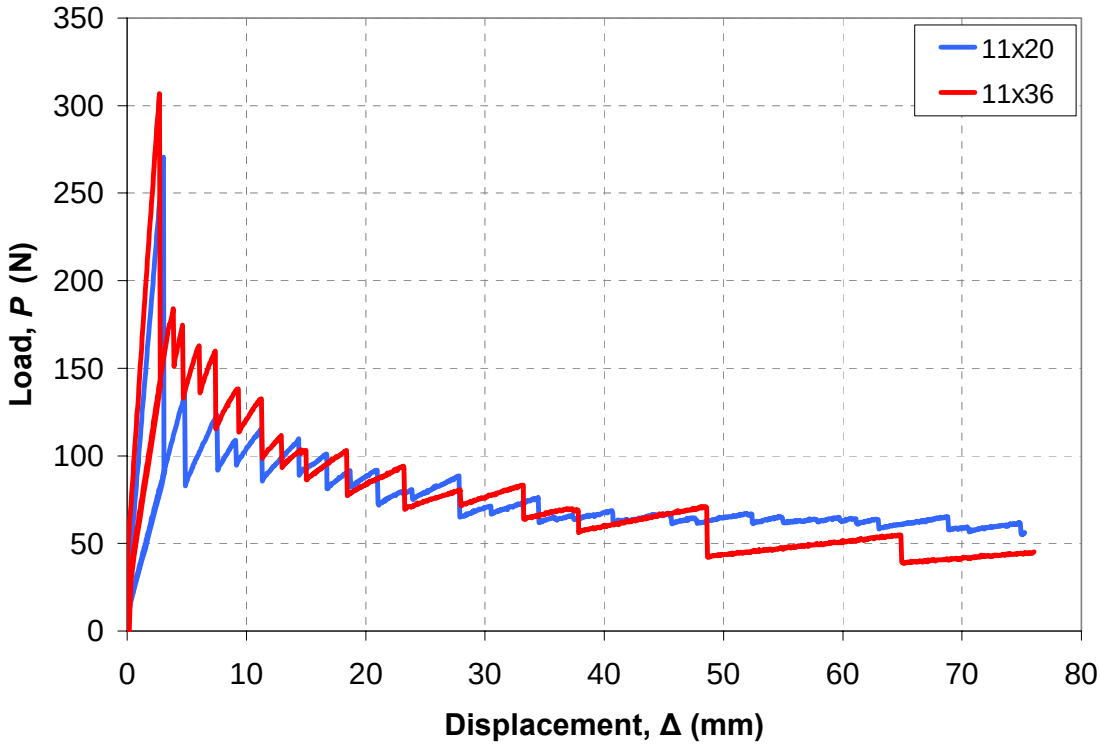

Figure 5.25. Typical load-displacement traces for 11x20 and 11x36 ADCB specimens.

As with the DCB tests, only maximum and minimum load-displacement values associated with crack initiation and arrest were recorded and used in calculating the critical and arrest strain energy release rates, $\mathcal{G}_{I/IIc}$ and $\mathcal{G}_{I/IIa}$ respectively, due to the pronounced stick-slip behavior of the adhesive studied. It was observed that the cracks were typically driven along the interface of the least stiff adherend, which resulted in lower total fracture energy values when compared with those measured under pure mode I loading conditions. Figure 5.26 illustrates the results obtained from all static ADCB tests. It should be noted that square axes have not been implemented to better help the

reader visualize the data. Additionally, it should be noted that it is no coincidence that all of the data fall along the same line, as the ADCB test is specifically targeted to a fixed-ratio of mode-mixity given the constant adherend thicknesses, albeit mismatched.

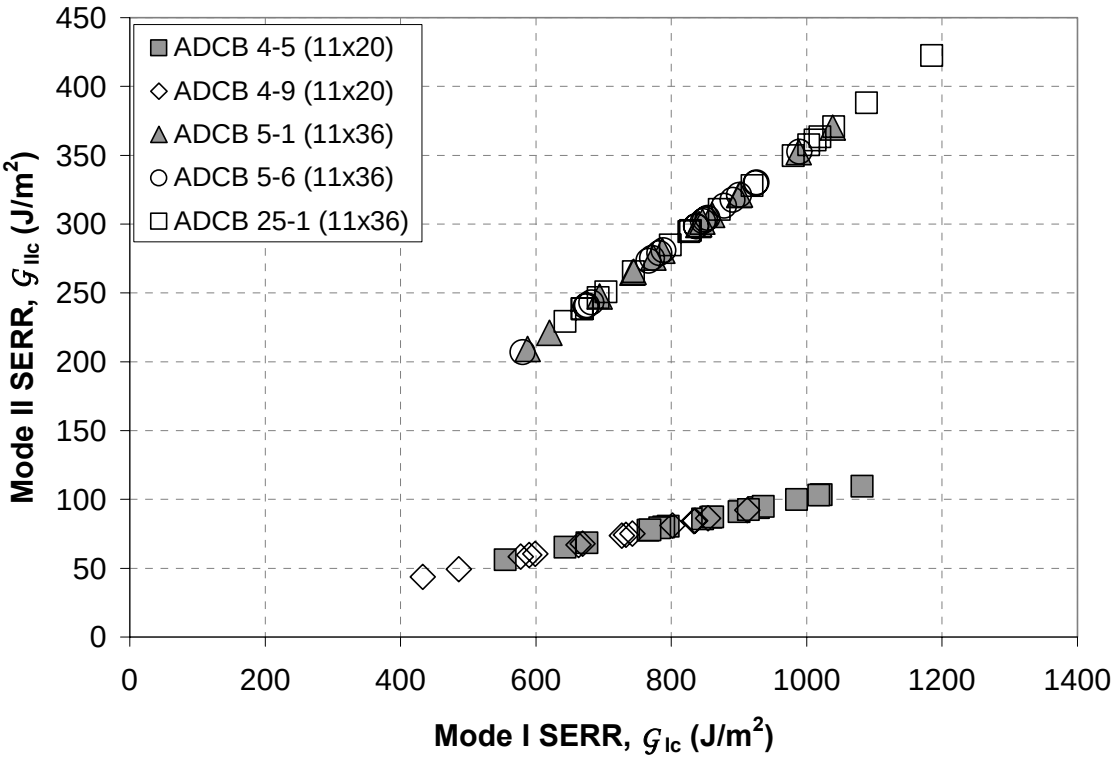

Figure 5.26. $\mathcal{G}_{IIc}$ vs. $\mathcal{G}_{Ic}$ for 11x20 and 11x36 quasi-static ADCB fracture tests.

Mean quasi-static mode I fracture energy values calculated using a work-based corrected beam theory analysis method were calculated to be *780 ± 155 J/m^2* and *810 ± 290 J/m^2* for the 11x20 and 11x36 bonded composite specimens respectively. The corresponding mode I components of the mean arrest values for the 11x20 and 11x36 bonded composite specimens were calculated to be *590 ± 60 J/m^2* and *600 ± 210 J/m^2* respectively. Additionally, mean quasi-static mode II critical fracture energy components were calculated to be *80 ± 15 J/m^2* and *290 ± 40 J/m^2* for the 11x20 and 11x36 specimens

respectively. The corresponding mode II mean arrest value components for the 11x20 and 11x36 ADCB specimens were calculated to be *60 ± 20 J/m²* and *210 ± 35 J/m²* respectively.

Additionally, just as with the DCB specimens and described in section 5.1.1 of this thesis, an energy method approach has been employed for calculating the total average mixed-mode fracture energy of the ADCB specimens. Spatially averaged values for the 11x20 and 11x36 ADCB specimens were calculated to be *935 ± 170 J/m²* and *850 ± 150 J/m²* respectively. When compared with total mixed-mode fracture energy values calculated by summing the $\mathcal{G}_{Ic}$ and $\mathcal{G}_{IIc}$ components obtained using beam theory, the average values calculated using the energy method are approximately 8% and 23% lower for the 11x20 and 11x36 specimens respectively. Figure 5.27 provides the complete results for the fracture behavior of the ADCB specimens determined using the energy method approach.

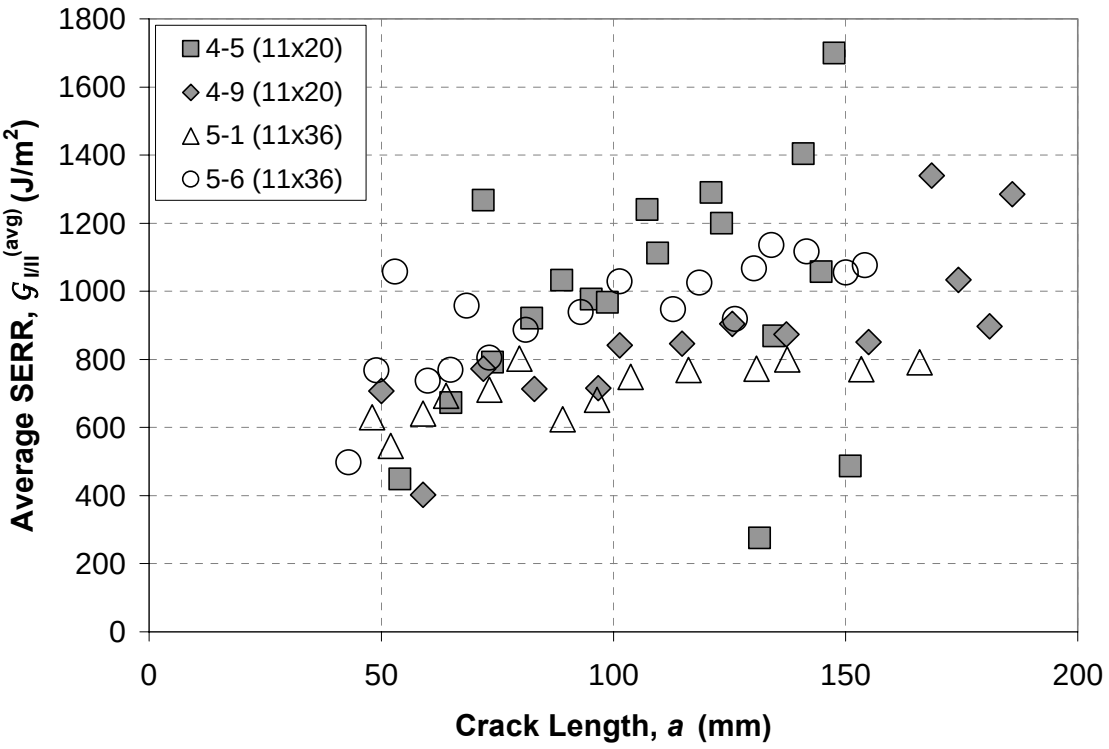

Figure 5.27. Average mixed-mode I/II fracture energies for 11x20 and 11x36 ADCB specimens calculated using energy method.

5.4.2. Asymmetric Double Cantilever Beam - Dynamic

Fracture events for the dynamic ADCB tests were captured with a high-speed imaging system at frame rates comparable to those used for the high-rate DCB fracture tests, as described in section 5.1.2 of this thesis, for test velocities of 0.01, 0.1, and 1 m/s respectively. The videos acquired during this process were correlated with the associated load-displacement traces in order to establish crack lengths corresponding with crack propagation events, which were in turn used in the data analysis procedure. Figure 5.28 shows a series of images obtained from this process.

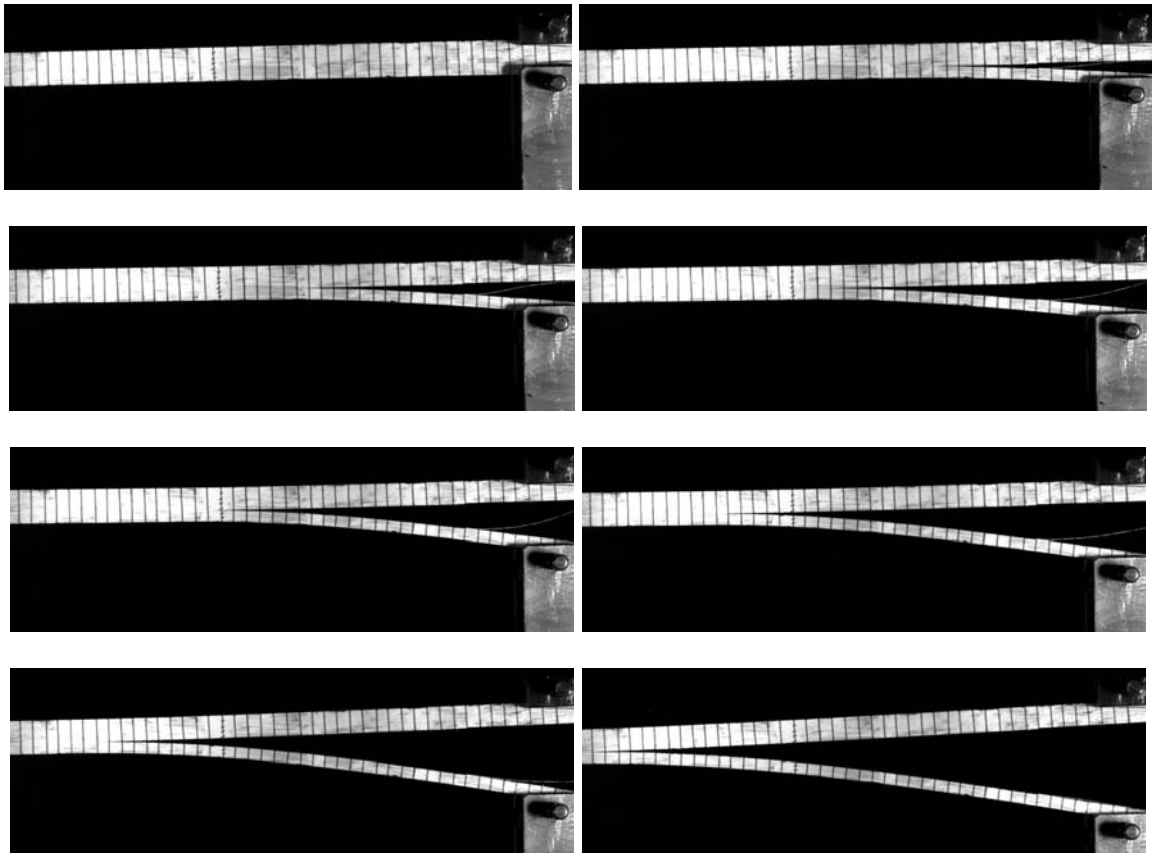

Figure 5.28. High-Speed images of a 11x36 ADCB specimen at a test velocity of 1 m/s.

As observed from the static tests conducted on ADCB specimens, the fracture surfaces of those specimens subjected to dynamic loading rates indicated crack growth along the interface of the stiffer adherend, which is illustrated in Figure 5.29. Faint stress whitened zones can be seen on both the 20-ply and 36-ply adherends, while most of the adhesive has been removed from the 11-ply adherends. Although many more data points were collected per specimen for the ADCB geometry when compared with the DCB geometry, stick-slip behavior was still observed. As such, average dynamic fracture energy values of the 11x20 ADCB specimens calculated using a work-based analysis method for loading rates of 0.01, 0.1, and 1 m/s were determined to be $748 \pm 117\ J/m^2$, $635 \pm 100\ J/m^2$, and $560 \pm 88\ J/m^2$ respectively. Additionally, values for the 11x36

specimens for the same applied loading rates were calculated to be *880 ± 130 J/m²*, *748 ± 111 J/m²*, and *660 ± 98 J/m²* respectively. Figure 5.30 provides a summary of the quasi-static and dynamic fracture energy values obtained using the ADCB specimen geometry.

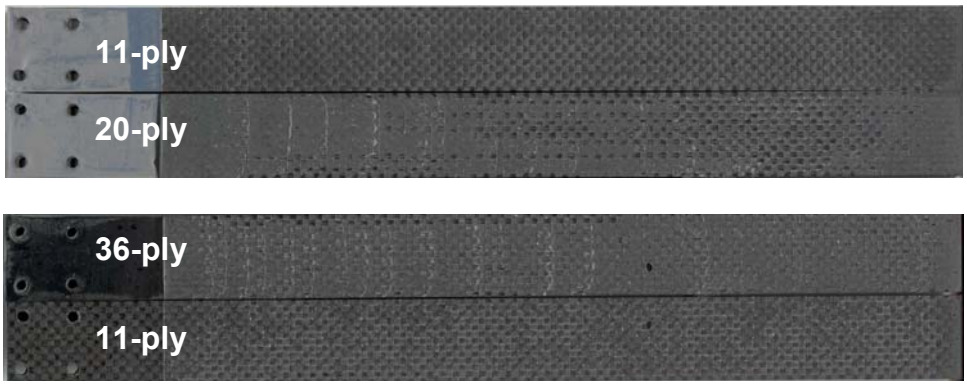

Figure 5.29. Fracture surface images for 11x20 (top) and 11x36 (bottom) ADCB specimens.

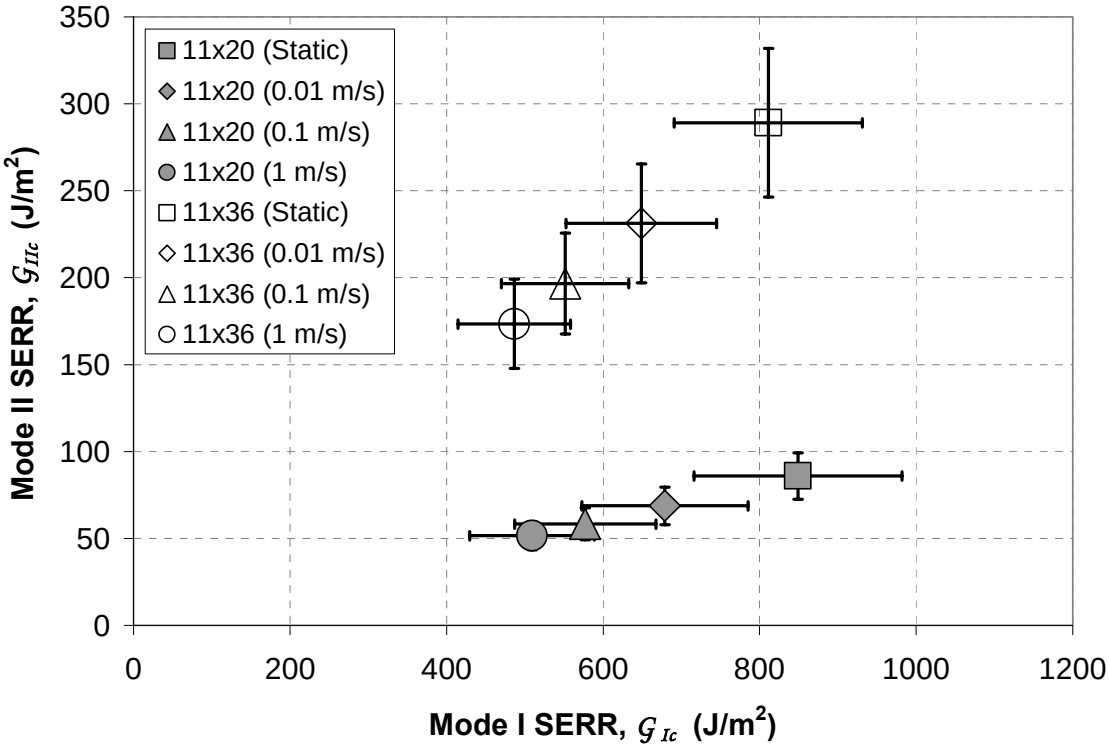

Figure 5.30. Summary of $\mathcal{G}_{IIc}$ vs. $\mathcal{G}_{Ic}$ for all 11x20 and 11x36 ADCB fracture tests.

5.4.3. Single Leg Bend - Static

All single leg bend tests were conducted on symmetric 11x11 and 20x20 bonded composite specimens, producing a constant mode I to mode II fracture ratio of 1.33. No tests were conducted on 36-ply specimens due to a lack of material availability. Visual crack length measurements were taken throughout each static test at crack initiation and arrest events to be used in subsequent data analysis. Several data points were obtained from each test; however, the number of measurable data points was somewhat limited given the need to both clamp the specimen in a fixture as well as induce a large pre-crack for stability purposes [12-13]. Sample load-displacement traces for all specimen configurations under quasi-static loading conditions are provided in Figure 5.31.

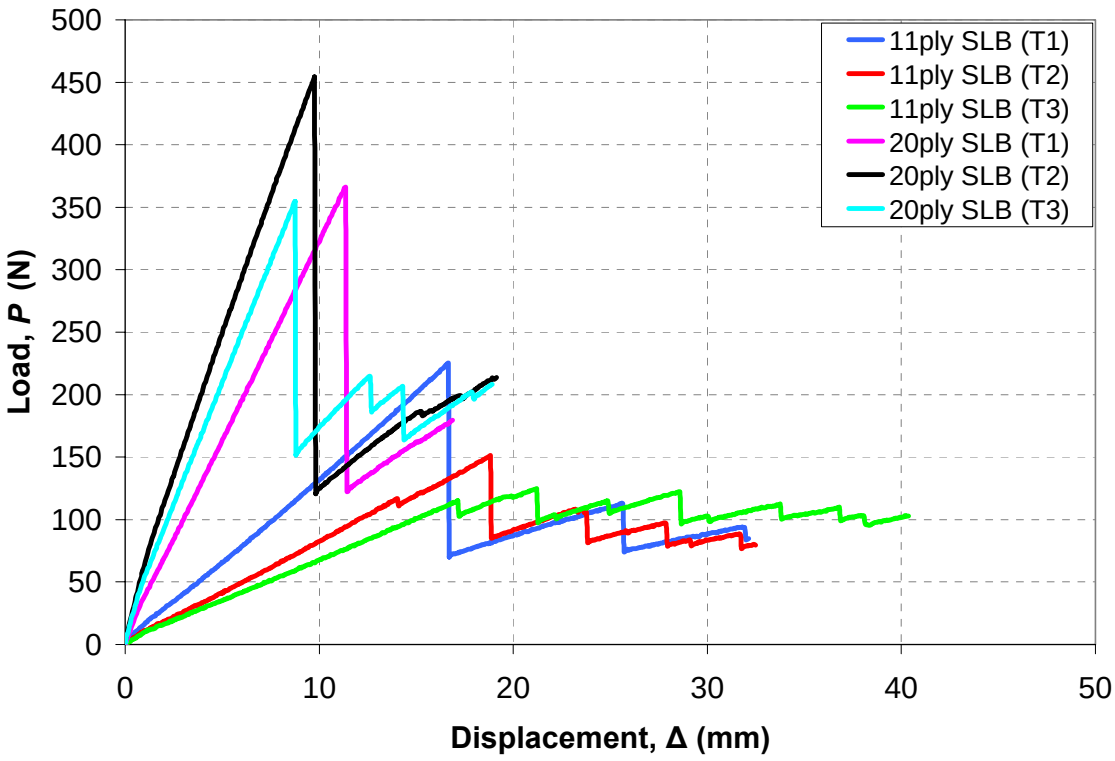

Figure 5.31. Load vs. displacement curves for all quasi-static SLB fracture tests.

Mean quasi-static mode I fracture energy values calculated using a work-based corrected beam theory analysis method were calculated to be *777 ± 160 J/m²* and *882 ± 141 J/m²* for the 11-ply and 20-ply bonded composite specimens respectively. The corresponding mode I mean arrest value for the 11-ply specimens was calculated to be *557 ± 160 J/m²*, as no usable arrest data was obtained for the 20-ply specimens due to a propensity of the propagating cracks to result in delamination of the composite adherends upon initial crack initiation. Additionally, mean quasi-static mode II critical fracture energy values were calculated to be *583 ± 119 J/m²* and *661 ± 106 J/m²* for the 11-ply and 20-ply specimens respectively. The corresponding mode II mean arrest value for the 11-ply specimens was calculated to be *418 ± 120 J/m²*. A summary of all static SLB results is provided in Figure 5.32.

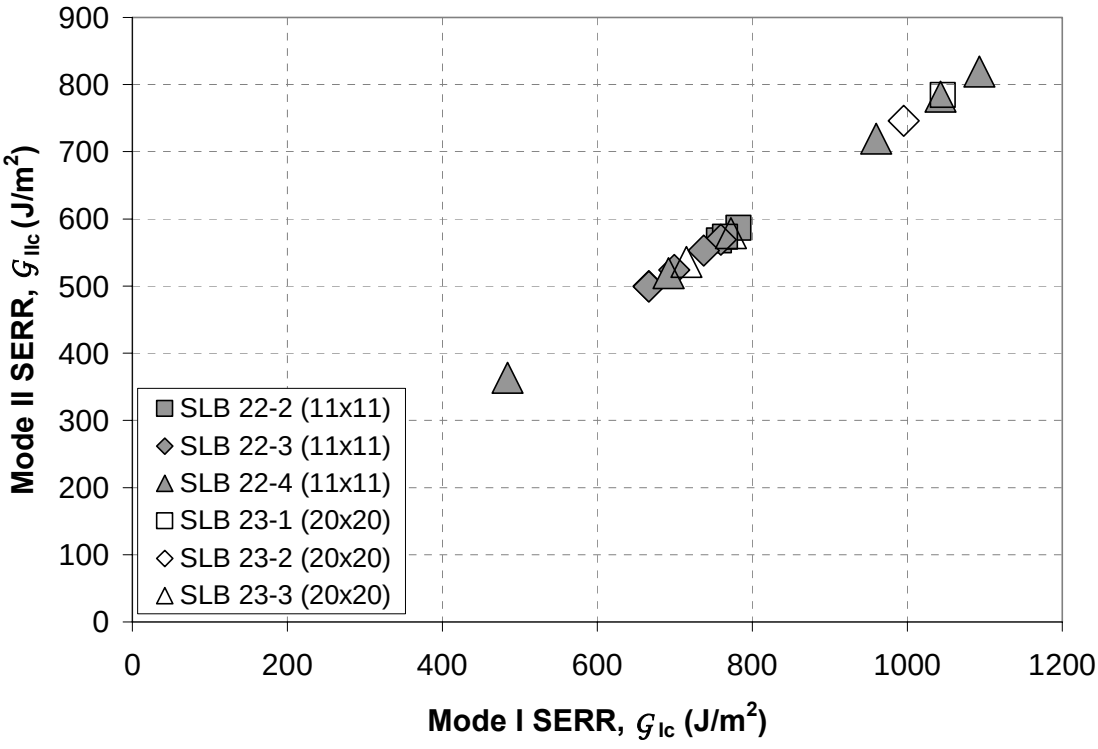

Figure 5.32. $\mathcal{G}_{IIc}$ vs. $\mathcal{G}_{Ic}$ for 11-ply and 20-ply quasi-static SLB fracture tests.

Additionally, the energy method approach has been employed for calculating the spatially averaged total mixed-mode fracture energy of the SLB specimens. An average value of $934 \pm 168\ J/m^2$ was calculated for the 11-ply specimen. No average values were calculated for the 20-ply specimens due to the limited number of data points obtained during those tests. When compared with total mixed-mode fracture energy value calculated by summing the $\mathcal{G}_{Ic}$ and $\mathcal{G}_{IIc}$ components obtained using beam theory, the average value calculated using the energy method is approximately 30% lower for the 11-ply specimens. Figure 5.33 provides the complete results for the fracture behavior of the SLB specimens determined using the energy method approach.

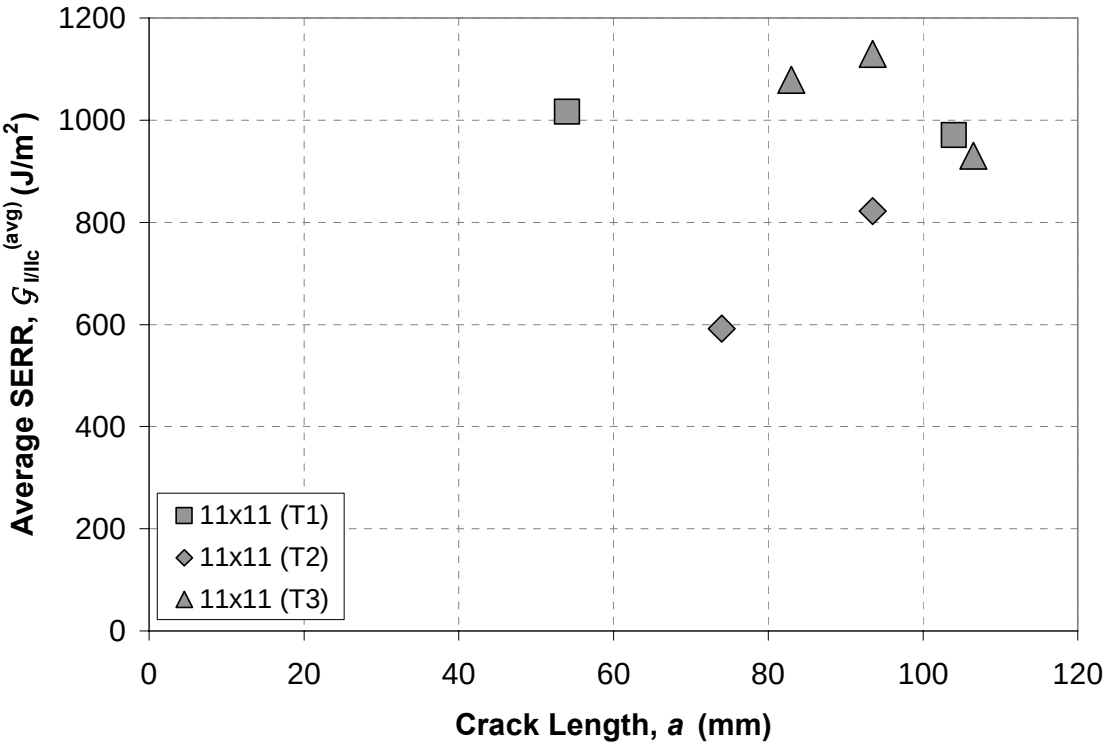

Figure 5.33. Average mixed-mode I/II fracture energies for 11-ply SLB specimens calculated using energy method.

5.4.4. Single Leg Bend - Dynamic

Fracture events for the dynamic SLB tests were captured with a high-speed imaging system at frame rates of 3000 and 9000 frames per second for test velocities of 0.1 and 1 m/s respectively. The videos acquired during this process were correlated with the associated load-displacement traces in order to establish crack lengths corresponding with crack propagation events, which were in turn used in the data analysis procedure. Figure 5.34 provides a series of images obtained from this process.

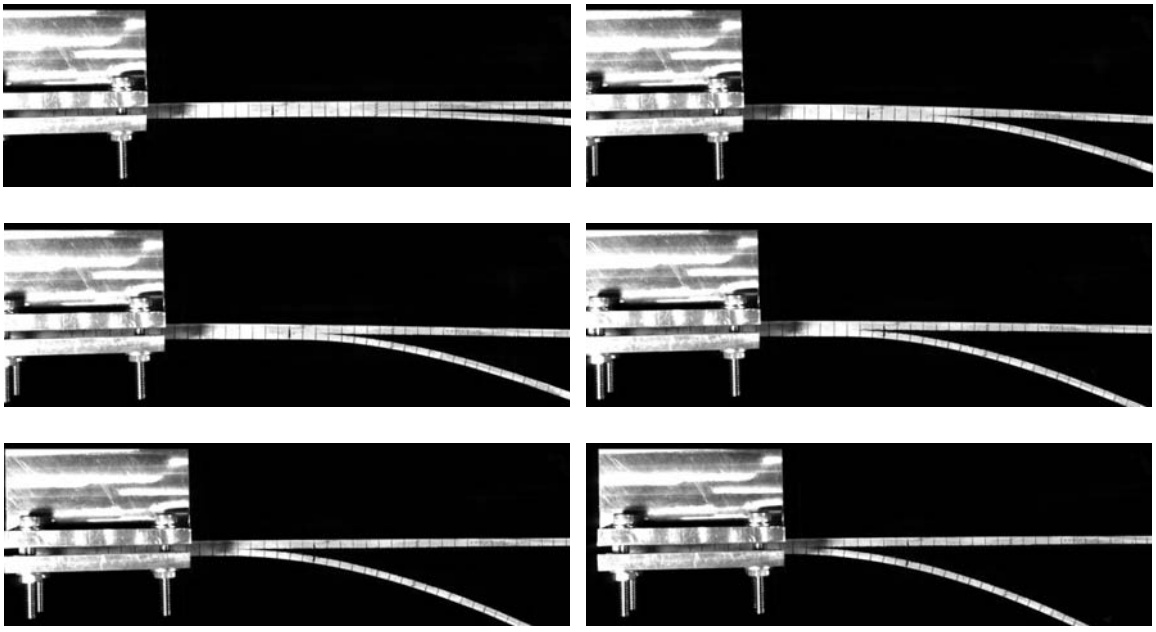

Figure 5.34. High-Speed images of a 11-ply SLB specimen at a test velocity of 1 m/s.

As observed from the static tests conducted on SLB specimens, the fracture surfaces of those specimens subjected to dynamic loading rates indicated crack growth along the interface of the adherend onto which the load was applied. Figure 5.35 provides images of the resulting fracture surfaces of both 11-ply and 20-ply SLB specimens. Faint stress whitened zones can be seen on the specimen fracture surfaces; however, they are rather difficult to see as displayed in Figure 5.35.

Figure 5.35. Fracture surface images for 11-ply (top) and 20-ply (bottom) SLB specimens.

Although five to six data points were collected on average for most 11-ply SLB specimens, only two or three data points were collected on average for the 20-ply specimens under dynamic loading conditions, as stick-slip behavior was still prominent. As such, an mean mixed-mode dynamic fracture energy, $G_{I/IIc}$, for the 11-ply SLB specimens calculated using a work-based analysis method for a loading rate of 1 m/s was determined to be $1024 \pm 264\ J/m^2$. The mode I and mode II components of the total fracture energy, $G_{I/IIc}$, were calculated to be $585 \pm 151\ J/m^2$ and $439 \pm 113\ J/m^2$ respectively. No tests were conducted on 11-ply specimens at loading rates of 0.01 or 0.1 m/s due to a combination of a lack of test specimens and time for experimentation. Additionally, mean mixed-mode fracture energy values for the 20-ply specimens for applied loading rates of 0.1 and 1 m/s were calculated to be $861 \pm 106\ J/m^2$ and $816 \pm 251\ J/m^2$ respectively.

Figure 5.36 provides a summary of the rate dependence observed using the SLB specimen geometry. Just as in all of the results presented thus far, there is a strong rate

dependence of the adhesive in question when utilized in the SLB configuration, which results in decreasing fracture energy values as loading rate is increased. The 20-ply data was fit using a power law relationship, and the resulting trend was determined to be $\mathcal{G}_{I/IIc}^{(20\,ply)} = 786\dot{\Delta}^{-0.0604}$. Additionally, no relationship was established for the 11-ply specimens as there was insufficient data to do so.

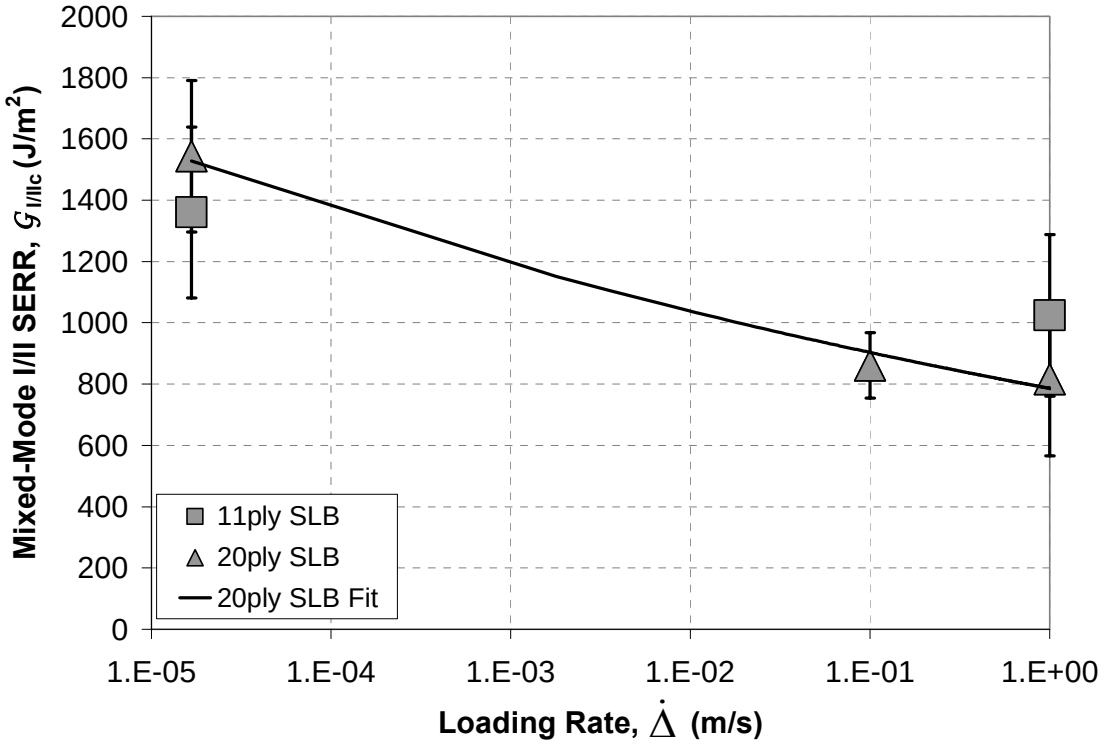

Figure 5.36. Summary of rate dependence for 11-ply and 20-ply SLB fracture specimens.

5.4.5. Comments

Both the asymmetric double cantilever beam and the single leg bend specimen geometries provide easily implemented test configurations for characterizing the mixed-mode I/II fracture behavior of bonded joints. The study of 11x20 and 11x36 specimens in the ADCB configuration provided mode-mixity ratios of 9.88:1 and 2.8:1 ($\mathcal{G}_{Ic}$ to $\mathcal{G}_{IIc}$)

respectively, while the study of 11-ply and 20-ply symmetric SLB specimens provided a fixed mode-mixity ratio of 1.33:1 ($\mathcal{G}_{Ic}$ to $\mathcal{G}_{IIc}$). Failure loci on all specimens suggest an interfacial failure, which in turn resulted in lower total fracture energy values when compared to mode I loading conditions. As with the DCB tests, both types of mixed-mode tests suggest a strong rate dependence, as total fracture energy values decreased with increasing applied loading rate. However, for the SLB configuration in particular, it is suggested that additional tests be conducted to more thoroughly characterize the mixed-mode fracture behavior of the adhesive in question, as only a limited number of tests were conducted at the higher rates of tests.

5.5. End-Loaded Split

Fracture testing conducted on the end-loaded split specimen geometry yielded one usable data point per 300mm long specimen. The crack propagation behavior observed was extremely unstable for both quasi-static and dynamic loading conditions. Upon initiation, the crack typically propagated into the composite adherends resulting in interlaminar failure, which was not conducive to characterizing the fracture behavior of the adhesive in question. On a rare occasion, the crack would propagate cohesively through the adhesive layer; however, only two usable data points per specimen would be acquired during such events as erratic stick-slip behavior resulted in large crack jumps between fracture initiation. A limited number of tests were conducted under both static and dynamic loading conditions as several iterations of test fixturing was utilized prior to achieving an effective apparatus, thus resulting in the testing of multiple specimens before acquiring usable data.

5.5.1 Static ELS

All static ELS specimens were subjected to an applied loading rate of 1 mm/min. Specimens were loaded up to a point that resulted in crack initiation, at which time the tests would typically be concluded as there was a propensity for the cracks to steer out of the adhesive layer and propagate into the composite adherends. Visual crack length measurements were made prior to each test, as such measurements were not possible post experimentation due to the absence of stress whitened zones. Sample load-displacement traces for all specimen configurations under quasi-static loading conditions are provided in Figure 5.37. No data was collected on the 36-ply specimens due to a lack of material availability.

Average quasi-static mode II fracture energy values, G_{IIc}, calculated using a work-based corrected beam theory analysis method were calculated to be $5827 \pm 509\ J/m^2$ and $6713 \pm 298\ J/m^2$ for the 11-ply and 20-ply bonded composite specimens respectively. These results reflect one of the multiple work-based analysis methods presented in the literature [14-15] for the ELS geometry, where the mode II crack length correction factor, Δ_{II}, is approximated as $0.42\Delta_I$, where Δ_I is the mode I crack length correction factor determined from a standard DCB test. It has been suggested that the implementation of an experimentally determined clamp correction be utilized for more accurate analysis [14-15]; however, due to time constraints, the corresponding clamp calibration procedure could not be completed.

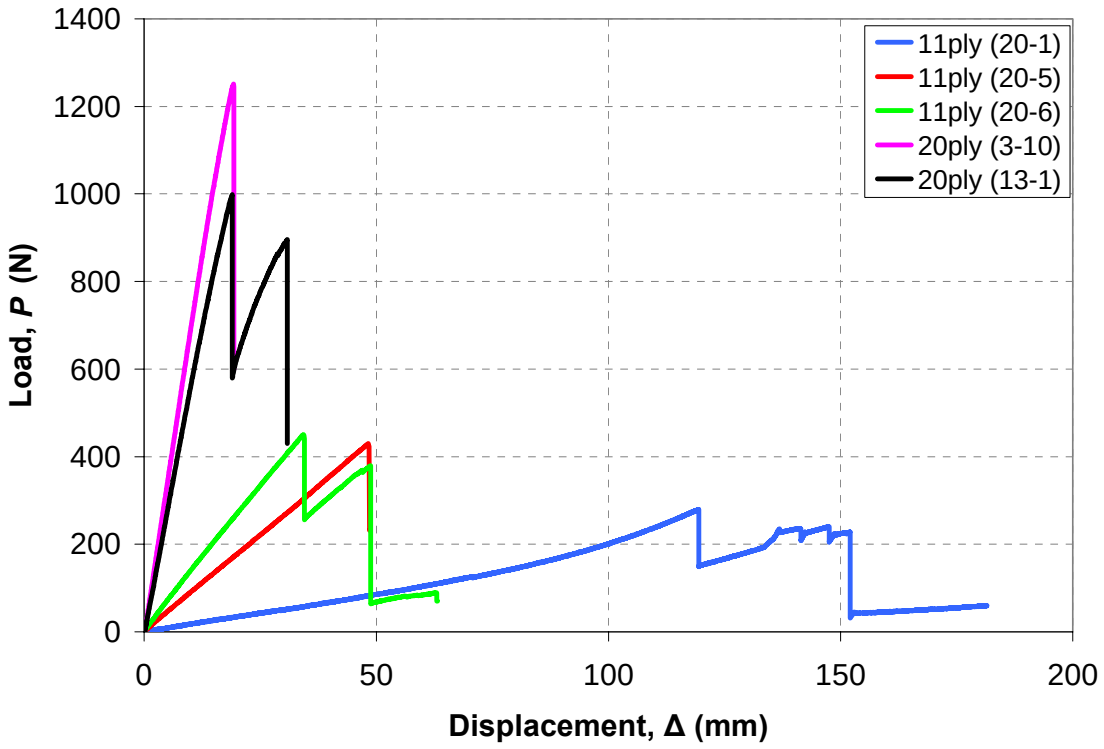

Figure 5.37. Load vs. displacement curves for all quasi-static ELS fracture tests.

Unlike the previously discussed fracture specimen geometries, no usable arrest data was obtained for any of the ELS specimens due to the propensity for cracks to propagate into the composite adherends. Furthermore, the energy method could not be employed to obtain average fracture energy values for the same reasoning. Figure 5.38 provides a complete summary of the quasi-static fracture energy values calculated for the ELS geometry.

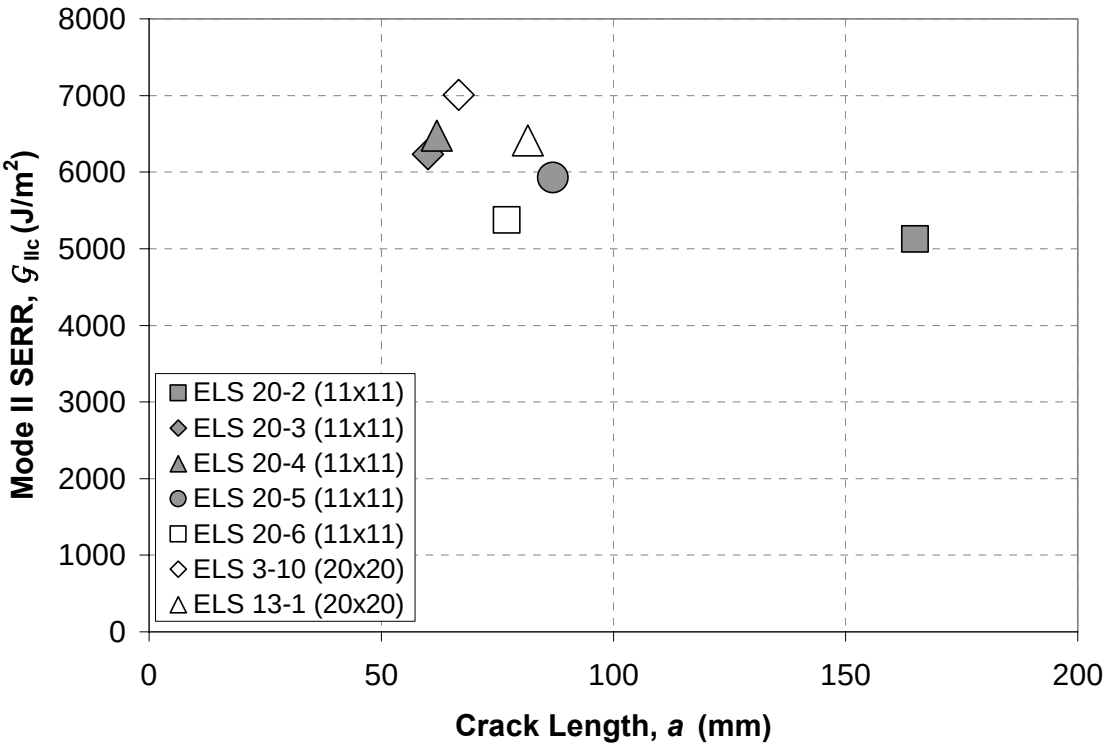

Figure 5.38. Mode II fracture energy, G_{IIc}, vs. crack length, a, for 11-ply and 20-ply bonded composite ELS specimens.

5.5.2. Dynamic ELS

Fracture events for the dynamic ELS tests were captured with a high-speed imaging system at frame rates of 3000 and 9000 frames per second for test velocities of 0.1 and 1 m/s respectively. The videos acquired during this process were correlated with the associated load-displacement traces in order to establish crack lengths corresponding with crack propagation events, which were in turn used in the data analysis procedure. Figure 5.39 provides a series of images obtained from this process.

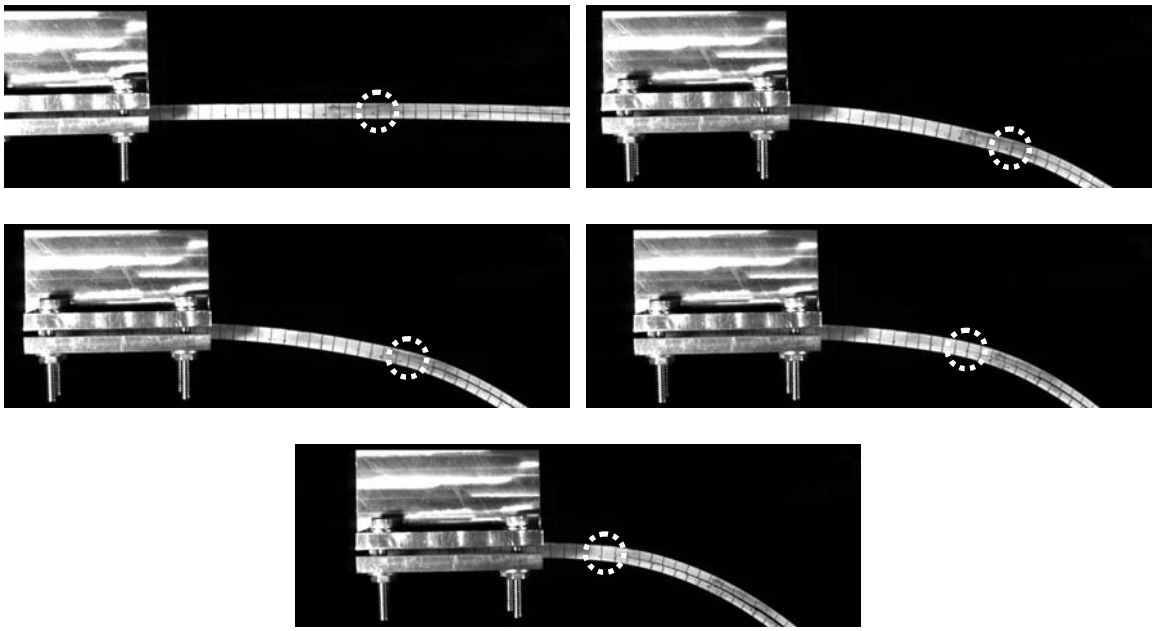

Figure 5.39. High-Speed images of a 11-ply ELS specimen at a test velocity of 1 m/s. Crack tips have been highlighted with a dashed circle.

As observed from the static tests conducted on ELS specimens, the fracture surfaces of those specimens subjected to dynamic loading rates indicated crack propagation into the composite adherends in most cases; however, on occasion, more than one fracture event was observed to occur cohesively within the adhesive layer. Figure 5.40 provides images of the resulting fracture surfaces of both 11-ply and 20-ply ELS specimens.

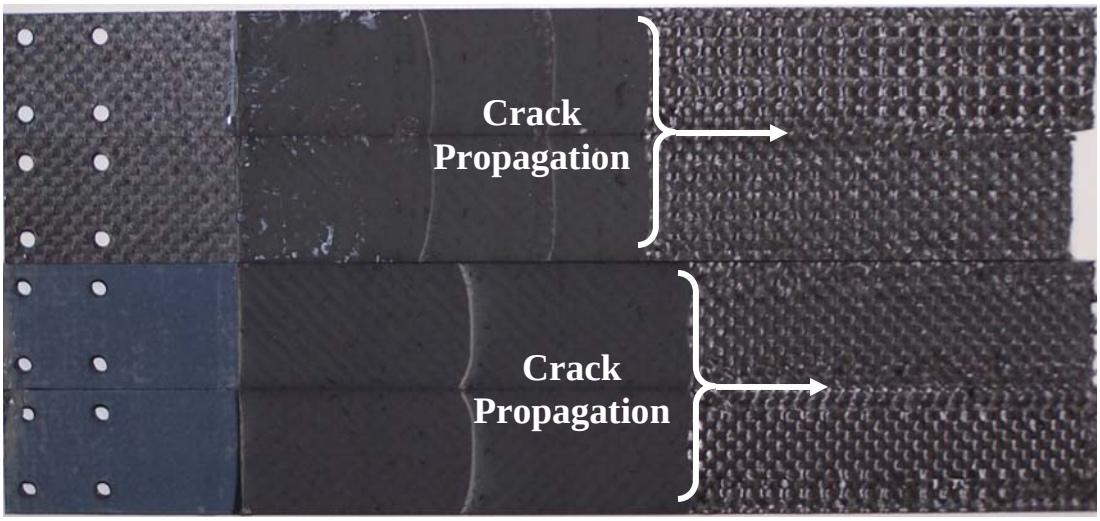

Figure 5.40. Fracture surface images for 11-ply (top) and 20-ply (bottom) ELS specimens.

Stick-slip behavior was observed to be very prominent in all ELS specimens as the fracture behavior of these specimens was highly unstable. As such, a mean mode II fracture energy value, $\mathcal{G}_{IIc}$, for the 11-ply ELS specimens was calculated to be *4700 ± 286 J/m²* for an applied loading rate of 1 m/s. No additional mode II dynamic tests were conducted on the 11-ply specimens due to a lack of material availability. Similarly, average mode II fracture energies for the 20-ply ELS specimens calculated using a work-based analysis method for loading rates of 0.1 and 1 m/s were determined to be *4813 ± 553 J/m²* and *3184 ± 576 J/m²* respectively. Figure 5.41 provides a summary of the rate dependence observed using the ELS specimen geometry. It is clear that the rate dependence observed thus far remains present in the mode II configuration, which again results in decreasing fracture energy values as loading rate is increased. The 20-ply data was fit using a power law relationship, and the resulting trend was determined to be $\mathcal{G}_{IIc}^{(20\,ply)} = 3597\dot{\Delta}^{-0.0597}$. Additionally, no relationship was established for the 11-ply specimens as there was insufficient data to do so.

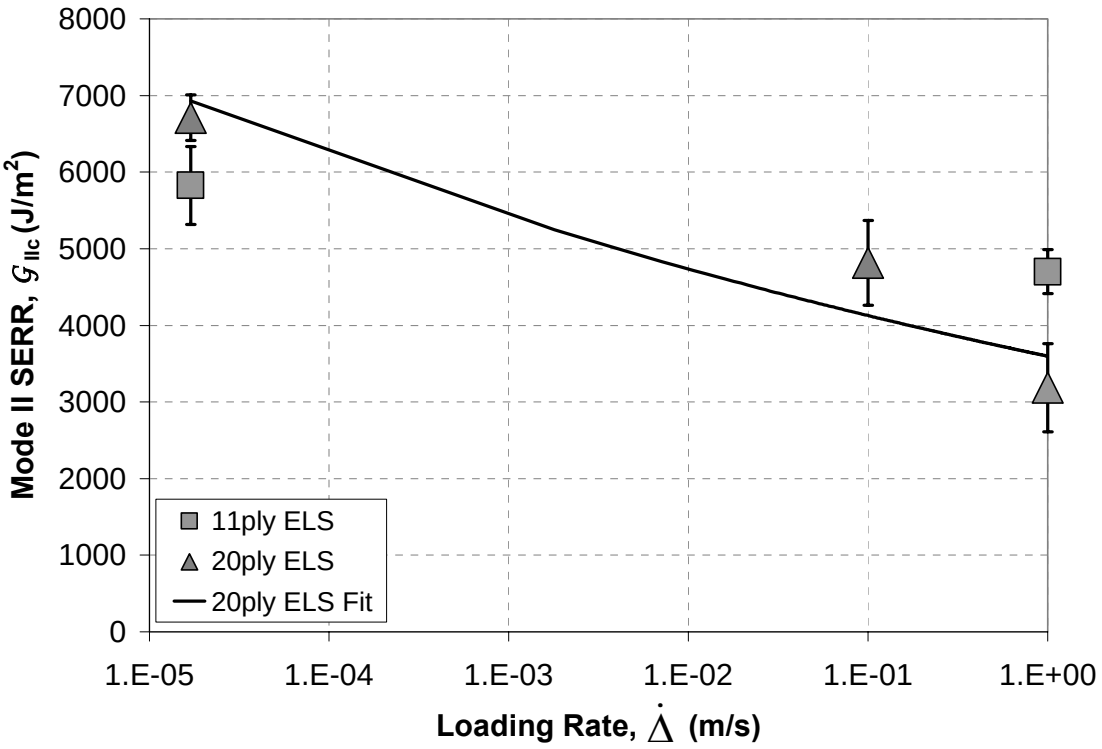

Figure 5.41. Summary of rate dependence for 11-ply and 20-ply ELS fracture specimens.

5.5.3. Comments

Considering the initiation values of $\mathcal{G}_{IIc}$, the adhesive used in the manufacture of the bonded composite joints studied have a mode II critical fracture energy twice that of the mode I critical fracture energy. All specimens tested illustrated a strong rate dependence, and as such, have mode II fracture energy values that decrease as a function of the applied loading rate. Furthermore, all end loaded split specimens tested exhibited extreme instability, which resulted in the measure of only one to two data points per specimen as there was a propensity for cracks to propagate into the composite adherends. Although crack length corrections have been implemented in the calculation of $\mathcal{G}_{IIc}$, it is suggested that alternative techniques, such as an experimentally determined clamp

correction or effective crack length approach, may provide more accurate results. Such corrections can be easily incorporated given the success of the current test apparatus; however, due to time constraints and material availability, these corrections are not reflected in the results presented in this thesis. Additionally, it is suggested that additional tests be conducted on ELS specimens to more completely characterize the mode II fracture behavior of the adhesive in question as only a limited number of tests were conducted at higher rates of test.

5.6. Split Cantilever Beam

The split cantilever beam test was originally thought to represent a simple method for examining the mode III fracture behavior of bonded joints, as this test configuration is simple to manufacture and easily implemented experimentally. However, upon further investigation, it has been observed that there is a significant mode II contribution to fracture using the SCB geometry, thus making this test not suitable for characterizing pure mode III behavior. Both experimental and numerical techniques have been used to verify this, which will be presented hereafter.

5.6.1. Results - Experimental

Initial testing on the SCB specimens revealed a lateral instability that resulted in a crack opening behavior conducive to a mixed-mode loading condition instead of the intended mode III loading. For the thinner specimens tested (i.e. 11-ply), this phenomena was believed to have occurred due to lateral buckling instability. This concept is better illustrated in Figure 5.42. Although such results could provide another usable data point

on an eventual fracture envelope, initial tests did not yield results portraying pure mode III fracture conditions.

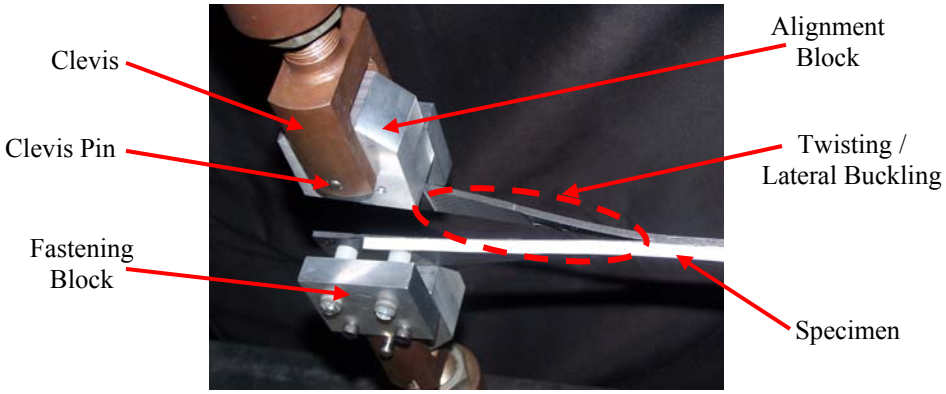

Figure 5.42. Mode III test set-up with observed lateral buckling for 11-ply SCB specimen.

An attempt to correct this problem was made by conducting additional experiments on the thicker specimens (i.e. 20-ply and 36-ply bonded composite joints). Due to their increased thicknesses and stiffness, it was believed that these specimens would be more resistant to lateral buckling and twisting under mode III loading conditions. Although the 20-ply specimens did offer an increase in lateral stability, they too exhibited an opening mode of fracture as the crack length was increased. However, the 36-ply specimens exhibited almost no opening as the crack length was increased, as lateral buckling was much less of an issue with this geometry. Figure 5.43 provides a comparison of the varying levels of lateral instability for the three different specimen thicknesses. The lateral buckling and specimen opening have been highlighted.

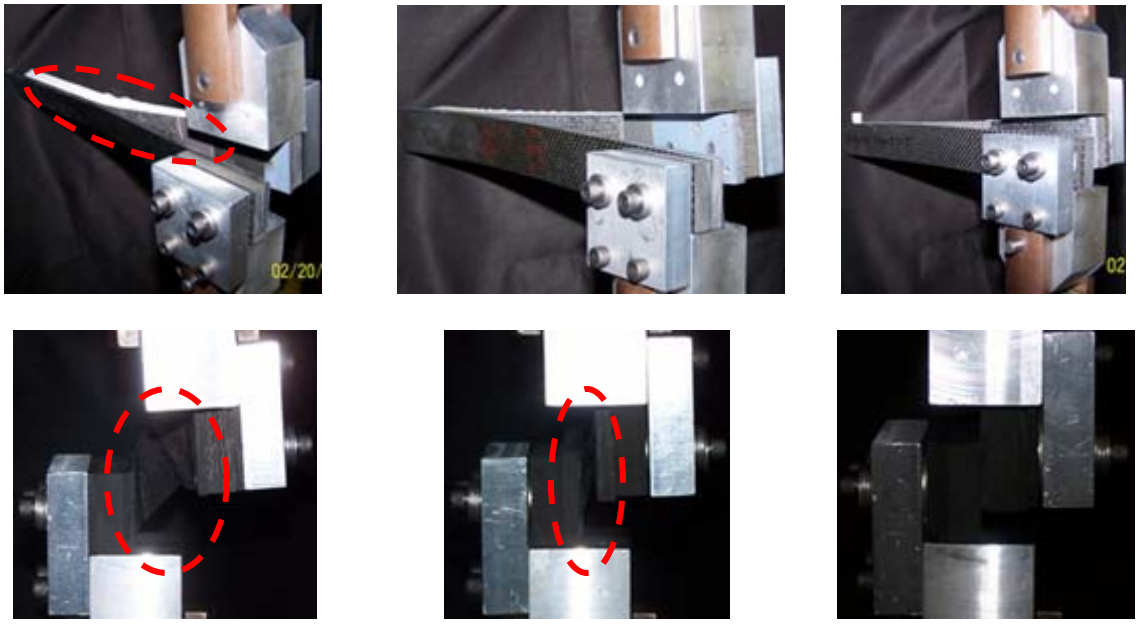

Figure 5.43. Comparison of specimen behavior under mode III loading conditions for 11-ply (left), 20-ply (middle), and 36-ply (right) bonded composite joints.

Based on the preliminary results, only the 36-ply bonded specimens would be considered for further experimentation as these specimens provided close to pure mode III loading conditions. All of the data gathered on this specimen configuration was quite consistent, as can be seen in the load-displacement traces and compliance plots provided in Figures 5.44 and 5.45 respectively. The resulting trend for the compliance curve illustrated in Figure 5.45 was determined to be $\log(C) = 1.898\log(a) - 3.51$.

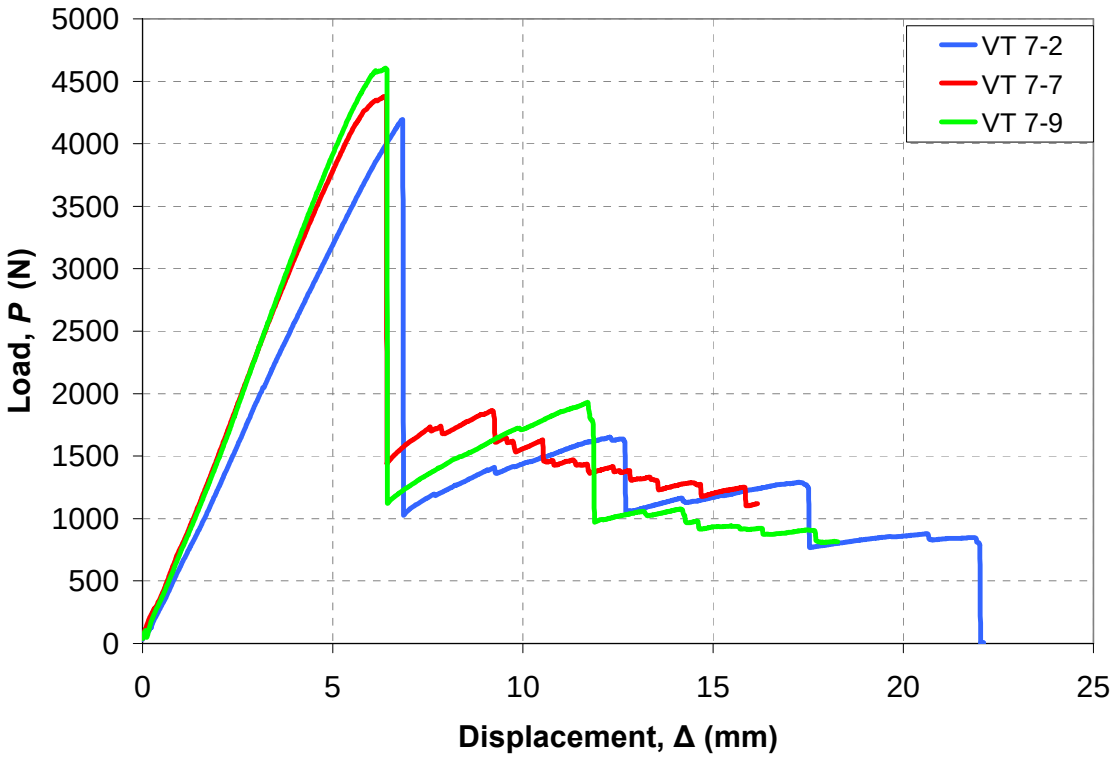

Figure 5.44. Load vs. displacement curves for 36-ply bonded composite SCB fracture tests.

Additionally, the fracture energy values calculated using an experimental compliance method were also quite consistent as a function of crack length amongst the results obtained from three different specimens as shown in Figure 5.46. The resulting relationship between the mode III fracture energy, $\mathcal{G}_{IIIc}$, and crack length, a, was established using a power law fit, and was determined to be $\mathcal{G}_{IIIc} = 5e^{6}a^{-1.3976}$. The results indicate a very large peak in $\mathcal{G}_{IIIc}$ for the initial point of crack propagation (i.e. for initial crack lengths of 50-60mm for all three tests). However, based on further review of the resulting fracture surfaces, it was observed that once past this initial point, cracks propagated out of the adhesive layer and into the composite adherends resulting in a stepped fracture surface along the length of each SCB specimen. A schematic of this

phenomenon was presented in Chapter 4 of this thesis, and photographs taken post experimentation are provided in Figure 5.47.

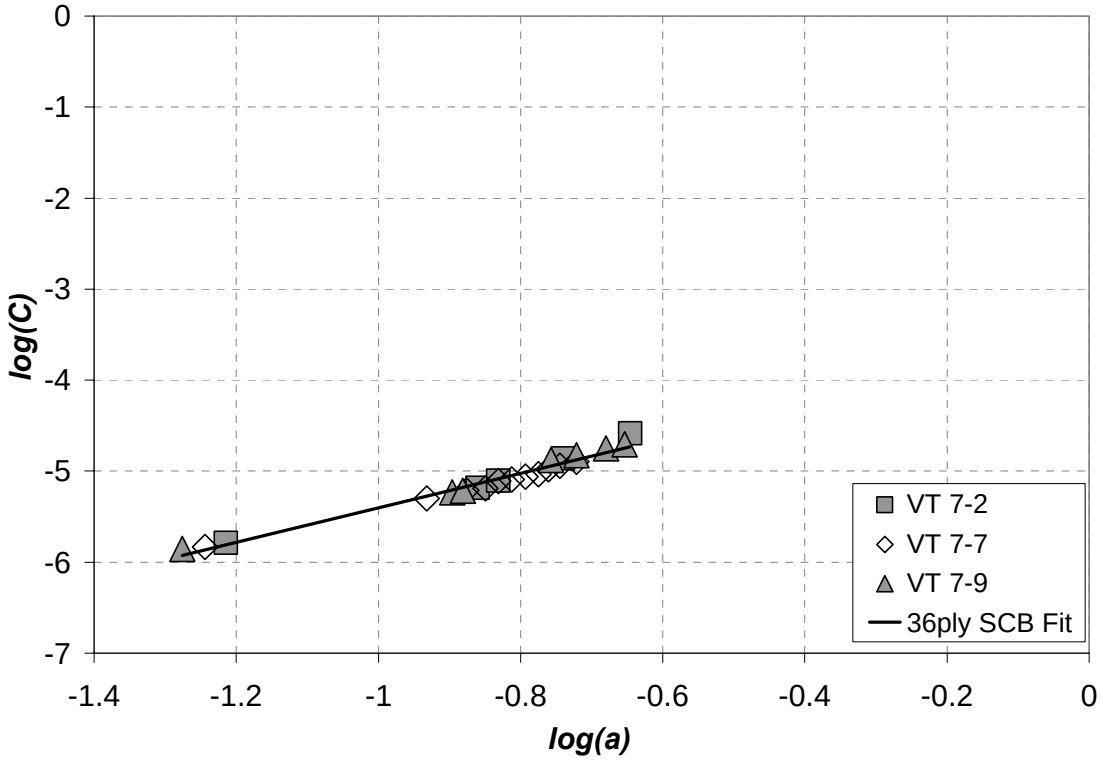

Figure 5.45. Compliance curve for 36-ply bonded composite SCB fracture tests.

Upon further examination of the resulting fracture surfaces, it is evident that there is a concentration of tangled and/or bridged fibers present along the centerline of each SCB specimen, as shown in Figure 5.47, which are directly related to the scissor-like shearing associated with mode III failures. Given that these phenomena occurred outside of the adhesive layer, fracture energy values obtained from points other than the initial crack front must be considered invalid for the purposes of this thesis, as only the initial crack front provided a crack initiation point within the adhesive layer. Furthermore, it is believed that the fracture energies obtained for very short crack lengths are also

inaccurate, as the measured values are much too high. There are several possible sources for error, such as inaccurate crack length measurements or stiffening effects caused by the test apparatus proximity to the pre-crack. Additionally, no dynamic fracture experiments were conducted on the SCB geometry due to time and material availability constraints.

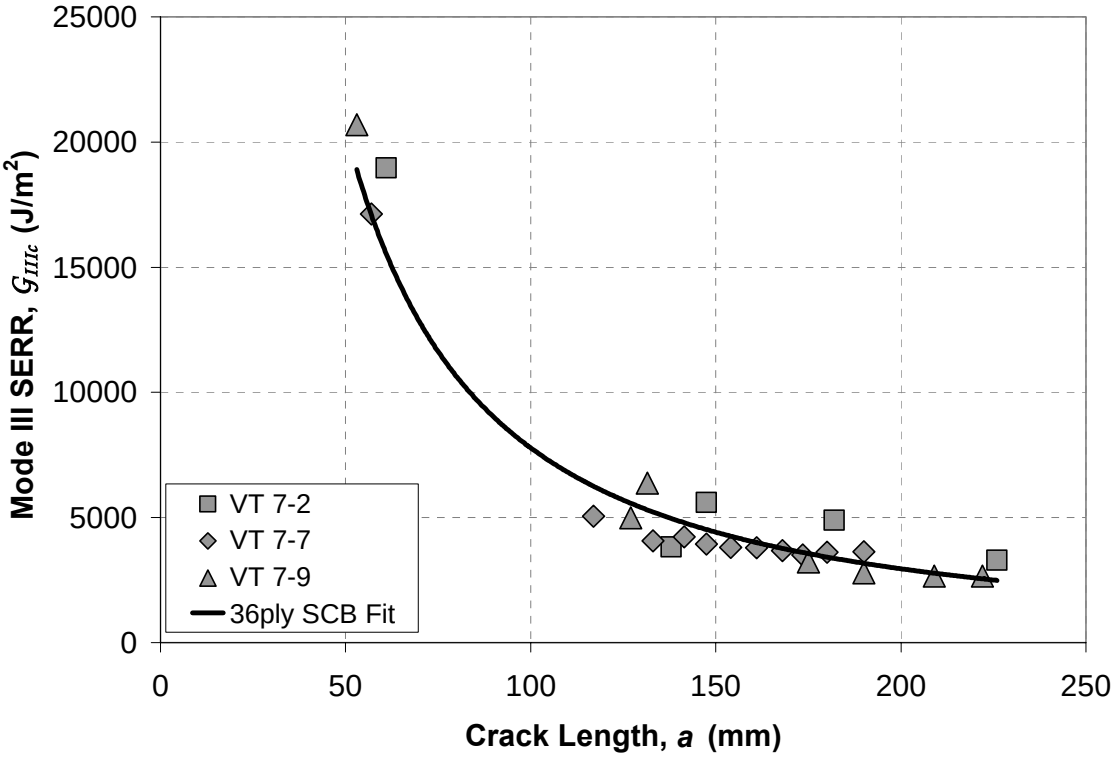

Figure 5.46. $\mathcal{G}_{IIIc}$ vs. crack length for 36-ply SCB fracture tests.

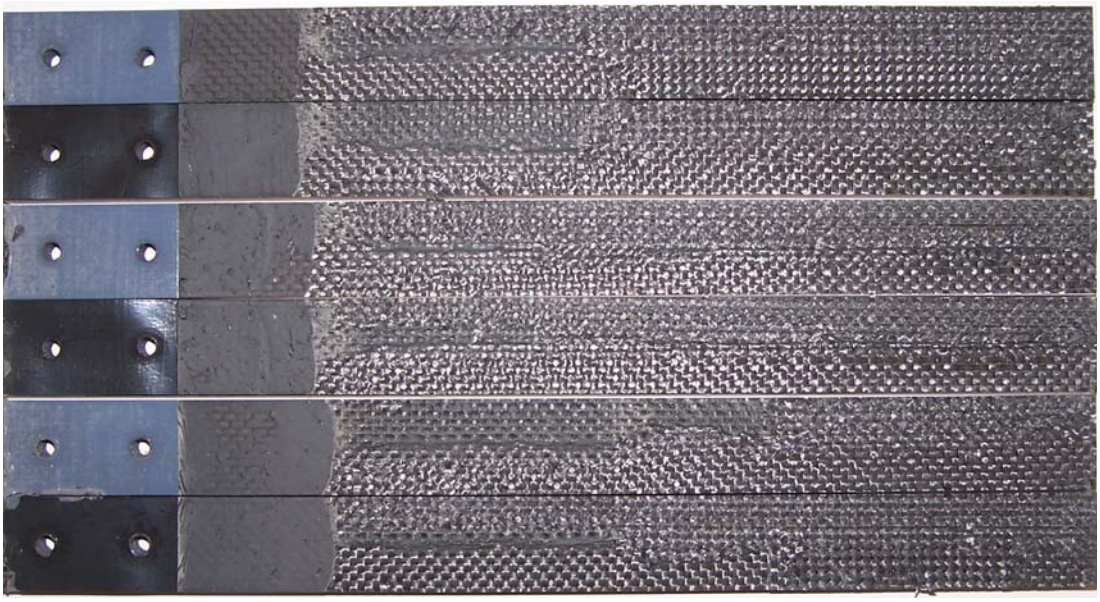

Figure 5.47. Fracture surface images for 36-ply SCB specimens.

5.6.2. Results - FEA

Figures 5.48 and 5.49 show the variation of the $\mathcal{G}_{IIc}/\mathcal{G}_{IIIc}$ as a function of crack front position, *d*, for bond widths of 25.4mm and 12.7mm respectively. It can be seen for both cases that the ratio of the mode II fracture energy to that of mode III is largest for shorter crack lengths for crack front positions located at the extreme edges of the specimen. However, it can also be seen that for a bond width of 12.7mm, that ratio is on the order of one magnitude lower than that obtained for bond widths of 25.4mm (or the full width of the specimen) for a given crack length.

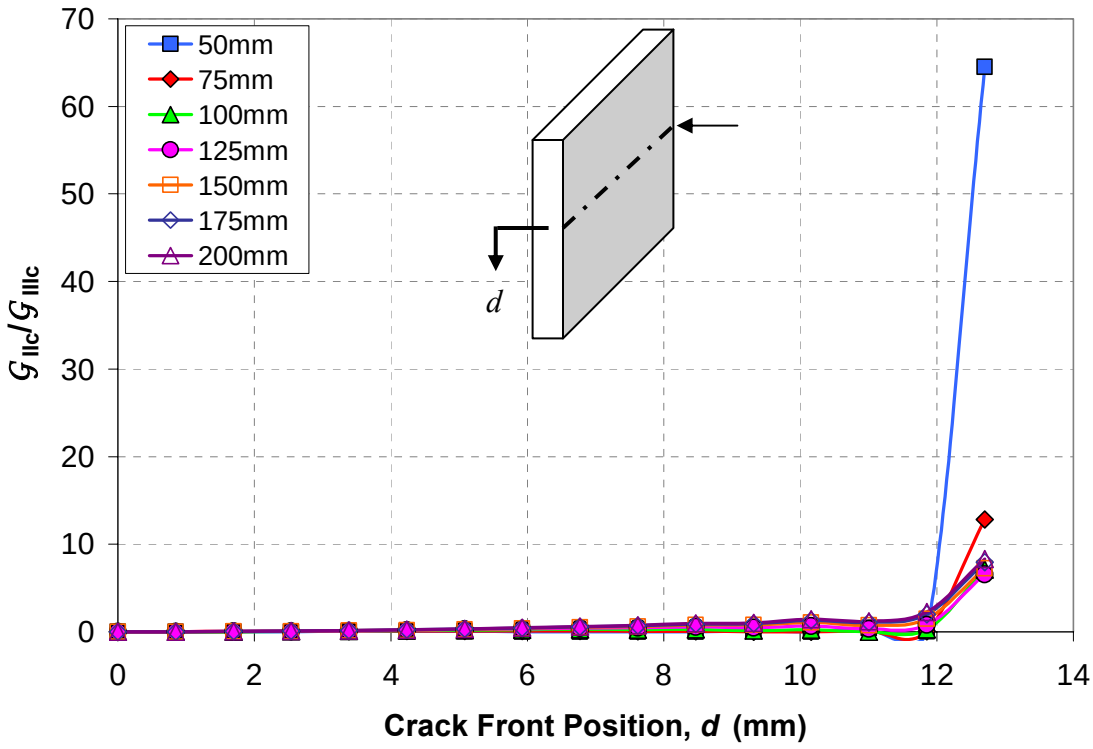

Figure 5.48. Variation of $\mathcal{G}_{IIc}/\mathcal{G}_{IIIc}$ as a function of position for mode III SCB specimen with a full bond width of 25.4mm. The crack front position, d = 0, corresponds with the centerline running along the length of the specimen.

Additionally, all three fracture energy components, $\mathcal{G}_{Ic}$, $\mathcal{G}_{IIc}$, and $\mathcal{G}_{IIIc}$, were averaged across the specimen width for each of the specified crack lengths to determine the overall contribution of each component as a function of crack length. As shown in Figure 5.50, it is clear that a specimen with a bond width equal to half of the overall specimen width provides much more consistent results with regard to the mode III fracture characterization; however, this was never tested experimentally as previously mentioned. For the specified crack lengths implanted in the finite element procedure, as

well as those typically encountered in the experimental aspect of this study, the $\mathcal{G}_{III}$ contribution for a specimen with a bond width of 12.7mm never falls below 80%.

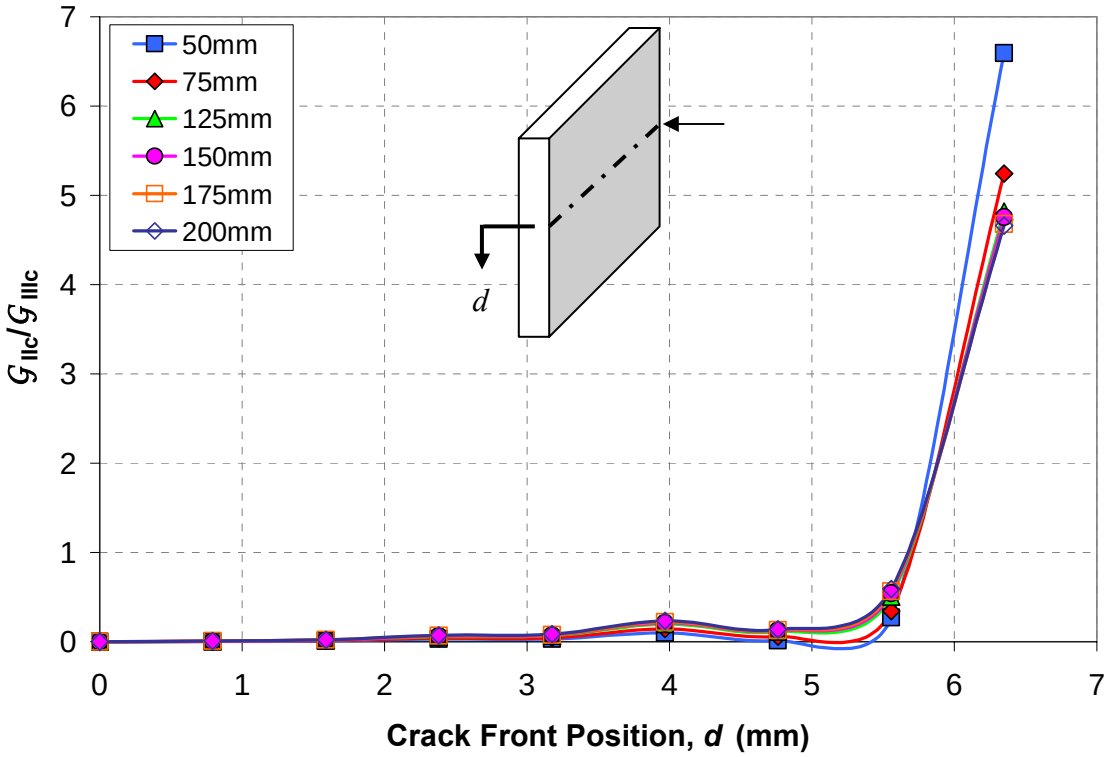

Figure 5.49. Variation of $\mathcal{G}_{IIc}/\mathcal{G}_{IIIc}$ as a function of position for mode III SCB specimen with a half bond width of 12.7mm. The crack front position, d = 0, corresponds with the centerline running along the length of the specimen.

However, for a specimen with a bond width equal to that of the overall specimen width, the $\mathcal{G}_{III}$ contribution declines rapidly with increasing crack length, allowing for a greater mode II contribution. It should be noted that mode I contributions were also considered; however, an average mode I contribution of less than 5% was observed and thus have not been included in Figure 5.50. The resulting trends for the mode II contributions for both the full and half bond width specimens were determined to be

$\left(\mathcal{G}_{IIc}/\mathcal{G}_{total}\right)^{(full)} = 3e^{-4}a^{1.359}$ and $\left(\mathcal{G}_{IIc}/\mathcal{G}_{total}\right)^{(half)} = 0.0324a^{0.344}$ respectively. Additionally, the resulting trends for the mode III contributions for both the full and half bond width specimens were determined to be $\left(\mathcal{G}_{IIIc}/\mathcal{G}_{total}\right)^{(full)} = 2.728a^{-0.273}$ and $\left(\mathcal{G}_{IIIc}/\mathcal{G}_{total}\right)^{(half)} = 0.976a^{-0.0364}$ respectively.

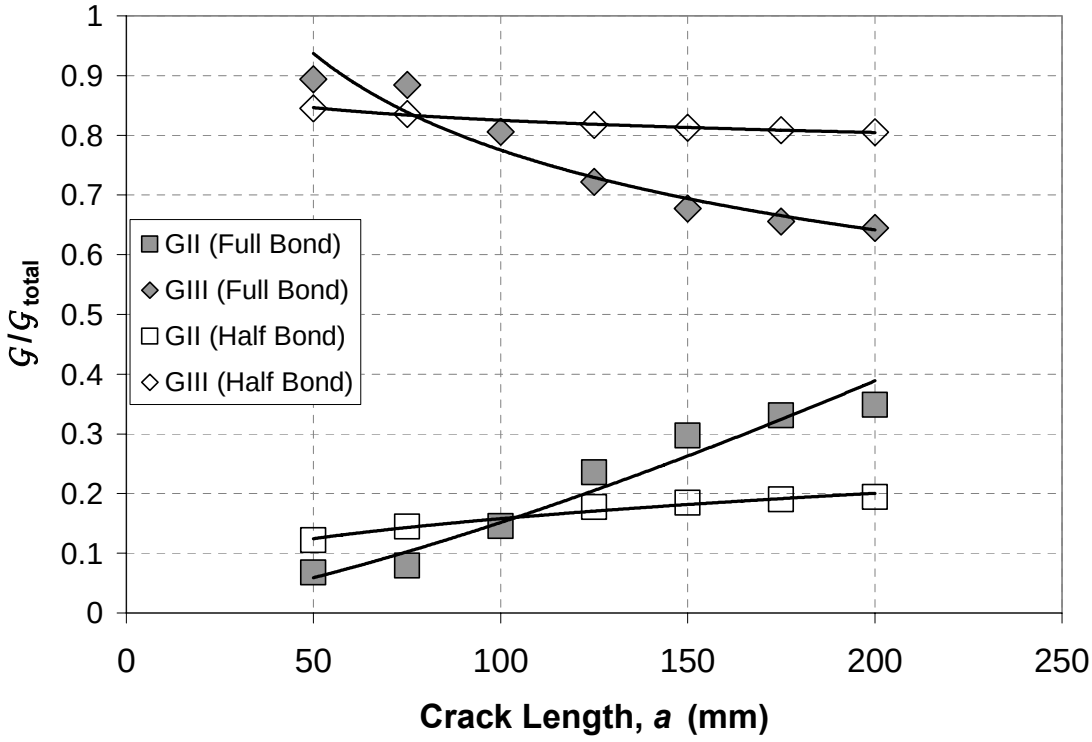

Figure 5.50. $\mathcal{G}/\mathcal{G}_{\text{total}}$ vs. crack length, a, for full and half bond width mode III SCB specimens.

5.6.3. Comments

In an attempt to characterize the mode III fracture behavior of adhesively bonded composite joints, the split cantilever beam would have represented a simple test method. However, given the significant mode II contribution to failure at the specimen edges, the geometry, as tested herein, should not be used. Several studies have been conducted in an attempt to utilize this geometry for characterizing mode III fracture [14-16], but

limited success has been achieved. Additionally, the SCB geometry does provide a valid test configuration for examining fracture behavior of adhesively bonded joints, although results obtained indicate that pure mode III failure does not occur. Based on results obtained in this study, one may speculate that very short crack lengths may be used to characterize pure mode III behavior; however, further studies are needed to verify this. Given the simplicity of the SCB specimen geometry, combined with the limited success of various other proposed geometries [17-19], one might speculate that further analysis and refinement of this test method could prove quite successful in characterizing mode III fracture.

References

1. BSI. *BS-7991*: "Determination of the Mode I Adhesive Fracture Energy, G_{Ic}, of Structural Adhesives Using the Double Cantilever Beam (DCB) and Tapered Double Cantilever Beam (TDCB) Specimens", 2001.
2. Simón, J. C., "Response and Failure of Adhesively Bonded Automotive Composite Structures under Impact Loads", Master's Thesis, Virginia Tech, Blacksburg, VA, 2004.
3. Gagliano, J. M., "An Improved Method for the Fracture Cleavage Testing of Adhesively Bonded Wood", Master's Thesis, Virginia Tech, Blacksburg, VA, 2004.
4. Yamini, S. and Young, R. J., "The Mechanical Properties of Epoxy Resins: Part II – Effect of Plastic Deformation Upon Crack Propagation", *Journal of Materials Science,* **15**, 1980, pp. 1823-1831.
5. Jacob, G. C., Starbuck, J. M., Pohlit, D. J., and Dillard, D. A., "Evaluating the Rate-Dependent Fracture Toughness of an Automotive Adhesive", To be submitted (*Journal of Adhesion*).
6. Pohlit, D. J., Dillard, D. A., Jacob, G. C., Starbuck, J. M., and Kapania, R., "On the Use of a Driven Wedge Test to Acquire Dynamic Fracture Energies of Bonded Beam Specimens: Part II – Numerical Analysis", To be submitted (*Journal of Adhesion*).
7. Blackman, B. R. K., Dear, J. P., Kinloch, A. J., MacGillivray, H., Wang, Y., Williams, J. G., and Yayla, P., "The Failure of Fibre Composites and Adhesively

Bonded Fibre Composites Under High Rates of Test: Part I - Mode I Loading - Experimental Studies", *Journal of Materials Science*, **30**, 1995, pp. 5885-5900.

8. Blackman, B. R. K., Kinloch, A. J., Wang, Y., and Williams, J. G., "The Failure of Fibre Composites and Adhesively Bonded Fibre Composites Under High Rates of Test: Part II - Mode I Loading - Dynamic Effects", *Journal of Materials Science*, **31**, 1996, pp. 4451-4466.
9. Dillard, D. A., Jacob, G. C., Pohlit, D. J., and Starbuck, J. M., "On the Use of a Driven Wedge Test to Acquire Dynamic Fracture Energies of Bonded Beam Specimens: Part I – Motivation and Experimental Implementation", To be submitted (*Journal of Adhesion*).
10. ASTM D-5045, "Standard Test Methods for Plane-Strain Fracture Toughness and Strain Energy Release Rate of Plastic Materials", in *Annual Book of ASTM Standards*, 2004, West Conshohocken, PA.
11. Xu, S. and Dillard, D. A., "Determining the Impact Resistance of Electrically Conductive Adhesives Using a Falling Wedge Test", *IEEE Transactions on Components and Packaging Technologies*, **26** (3), 2003, pp. 554-562.
12. Hashemi, S., Kinloch, A. J., and Williams, J. G., "The Analysis of Interlaminar Fracture in Uniaxial Fibre-Polymer Composites", in *Proceedings of the Royal Society of London. Series A, Mathematical and Physical Sciences*, **427** (1872), 1990, pp. 173-199.
13. Kinloch, A. J., Wang, Y., Williams, J. G., and Yayla, P., "The Mixed-Mode Delamination of Fibre Composite Materials", *Composites Science and Technology*, **47**, 1993, pp. 225-237.

14. Donaldson, S. L., Mall, S., and Lingg, C., "The Split Cantilever Beam Test for Characterizing Mode III Interlaminar Fracture Toughness", *Journal of Composites Technology and Research*, **13**, 1991, pp. 41-47.
15. Martin, R. H., "Evaluation of the Split Cantilever Beam for Mode III Delamination Testing", in *Composite Materials: Fatigue and Fracture (Third Volume), ASTM STP 1110*, 1991, pp. 243-266.
16. Sharif, F., Kortschot, M. T., and Martin, R. H., "Mode III Delamination Using a Split Cantilever Beam", in *Composite Materials: Fatigue and Fracture (Fifth Volume), ASTM STP 1230*, 1995, pp. 85-99.
17. Becht, G. and Gillespie, J. W., "Design and Analysis of the Crack Rail Shear Specimen for Mode III Interlaminar Fracture", *Composites Science and Technology*, **31**, 1988, pp. 143-157.
18. Lee, S. M., "An Edge Crack Torsion Method for Mode III Delamination Fracture Testing", *Journal of Composites Technology & Research*, **15** (3), 1993, pp. 193-201.
19. Farshad, M. and Flüeler, P., "Investigation of Mode III Fracture Toughness Using an Anti-Clastic Plate Bending Method", *Engineering Fracture Mechanics*, **60**, 1998, pp. 597-603.

Chapter 6: Summary

6.1: Observations

Various tests and analysis methods have been presented in this thesis for characterizing the fracture behavior of adhesively bonded composite joints. A large amount of data has been collected on the mode I, mixed-mode I/II, mode II, and mode III fracture of a commercially available epoxy system when adhesively bonded to composite adherends in a bonded joint configuration. Unstable crack growth was observed in all tests in the form of stick-slip crack propagation behavior, thus limiting the number of measurable data points per specimen. Additionally, an increase in the globally applied loading rate resulted in decreasing fracture energies for all of the different specimen configurations and loading conditions, suggesting a strong rate dependence. Although more tests are recommended for several of the test configurations examined, sufficient data has been provided to characterize the behavior of the adhesive system in question in response to impact loading conditions. Table 6.1 provides a summary of the average initiation values calculated for each of the tested configurations as a function of applied loading rate, while Figures 6.1 and 6.2 illustrate the fracture envelopes developed based on the results.

Mode I fracture tests were conducted in both bonded composite joint and bulk adhesive configurations. Due to the stick-slip nature of the adhesive studied, a maximum of four data points per specimen were obtained when testing standard double cantilever beam specimens. However, numerical analyses combined with results obtained in a related experimental study [1-2] suggest an alterative bonded joint specimen geometry in the form of a driven wedge specimen that resulted in an increase in the number of obtainable data points per specimen on the order of one magnitude. Finite element

analyses conducted on this alternative specimen geometry provide corrections for beam shear and root rotation present at the crack tip not accounted for in traditional beam theory analyses, resulting in a good correlation with experimental results obtained using the standard DCB configuration.

Table 6.1. Average critical fracture energies for all test configurations.

Specimen Type	Test Type	Critical SERR, $\mathcal{G}_c$ (J/m^2)			
		Static	0.01 m/s	0.1 m/s	1 m/s
11x11	Mode I DCB	2796	1571	1359	965
	Mode I DW	N/A	1626	1083	737
	Mixed-Mode I/II SLB	1360	N/A	N/A	1024
	Mode II ELS	5827	N/A	N/A	4700
20x20	Mode I DCB	2578	1038	918	665
	Mode I DW	N/A	1443	679	594
	Mixed-Mode I/II SLB	1544	N/A	861	806
	Mode II ELS	6713	N/A	4813	3184
36x36	Mode I DCB	2460	1404	1015	743
	Mode I DW	N/A	1379	1040	930
11x20	Mixed-Mode I/II ADCB	935	748	636	561
11x36	Mixed-Mode I/II ADCB	811	649	551	487
Bulk Adhesive	Mode I CT	2442	1240	1390	1056

Additionally, results obtained on bulk adhesive compact tension specimens also correlate well with bonded joint results as a function of applied loading rate. Furthermore, DMA results combined with CT results obtained in a related study at both ambient and sub-ambient temperatures [3] suggest that time temperature superposition may be used to characterize the dynamic fracture behavior of the adhesive in question. Such findings would suggest a much easier means for characterizing the fracture response of adhesives over a large range of measurable frequencies, and thus test velocities, unattainable by modern test equipment.

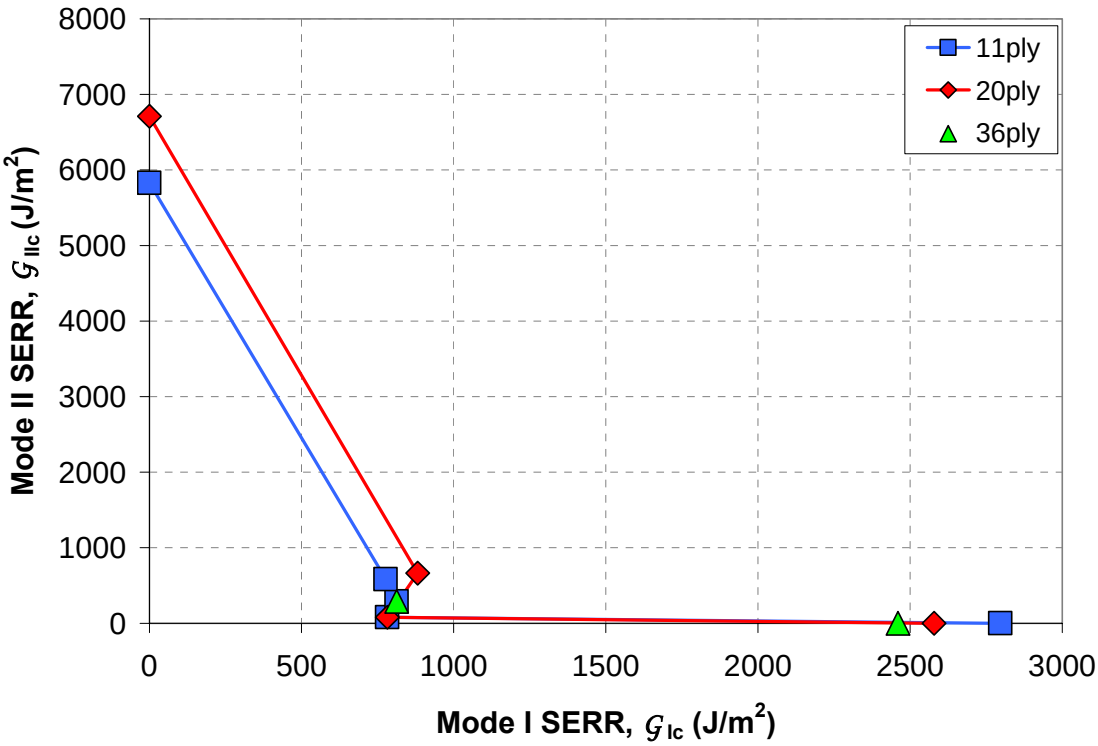

Figure 6.1. Static mixed-mode I/II fracture envelope.

Mixed-mode fracture tests conducted on asymmetric double cantilever beam and single leg bend specimens consistently resulted in interfacial failures, thus lowering the total measured fracture energy values when compared with mode I test results. Both specimen configurations result in a fixed-ratio mode-mixity level, although the ADCB specimens were manufactured in two different configurations providing two different levels of mode-mixity, thus allowing for a greater range of fracture characterization. Although stick-slip behavior was still present in both the ADCB and SLB specimen configurations, an increase in the number of measurable data points was observed due to the overall reduction in size of the observed crack jumps between crack arrest points.

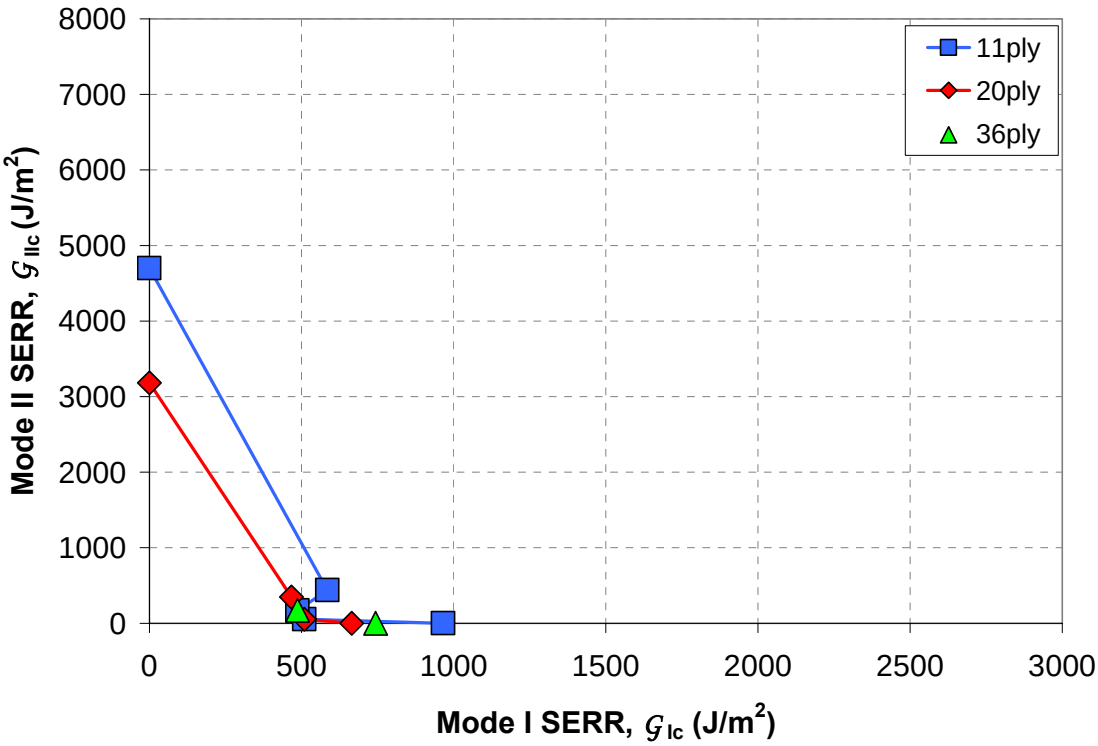

Figure 6.2. Dynamic mixed-mode I/II fracture envelope.

The design and development of a simple test apparatus provided an effective means for characterizing both mixed-mode I/II and mode II fracture behavior of adhesively bonded joints. Comprised mostly of off-the-shelf components, this test fixture is easily adaptable to both static and dynamic fracture testing, as well as various pieces of test equipment. To account for the axial force introduced into the mode II end loaded split test specimen due to the shortening moment arm occurring with increasing displacement, the entire fixture was designed to slide with lateral motion. With regard to measured mode II behavior, the ELS specimen was the most unstable specimen utilized in this study. With cracks typically propagating into the composite adherends upon initiation, only one data point was obtained for most ELS specimens, although, on

occasion, two data points were obtained. Additionally, mode II fracture energy values measured were approximately twice as large as those for mode I loading conditions. However, further data analysis should be conducted on the measured results, as additional analysis techniques not utilized in this thesis due to time constraints have been suggested to provide more accurate results [4-5]. Furthermore, Figure 6.3 illustrates the ratio of the measured fracture energy for a given rate, $\mathcal{G}_c$, to the baseline static fracture energy, $\mathcal{G}_{static}$, measured for each of the different specimen geometries tested.

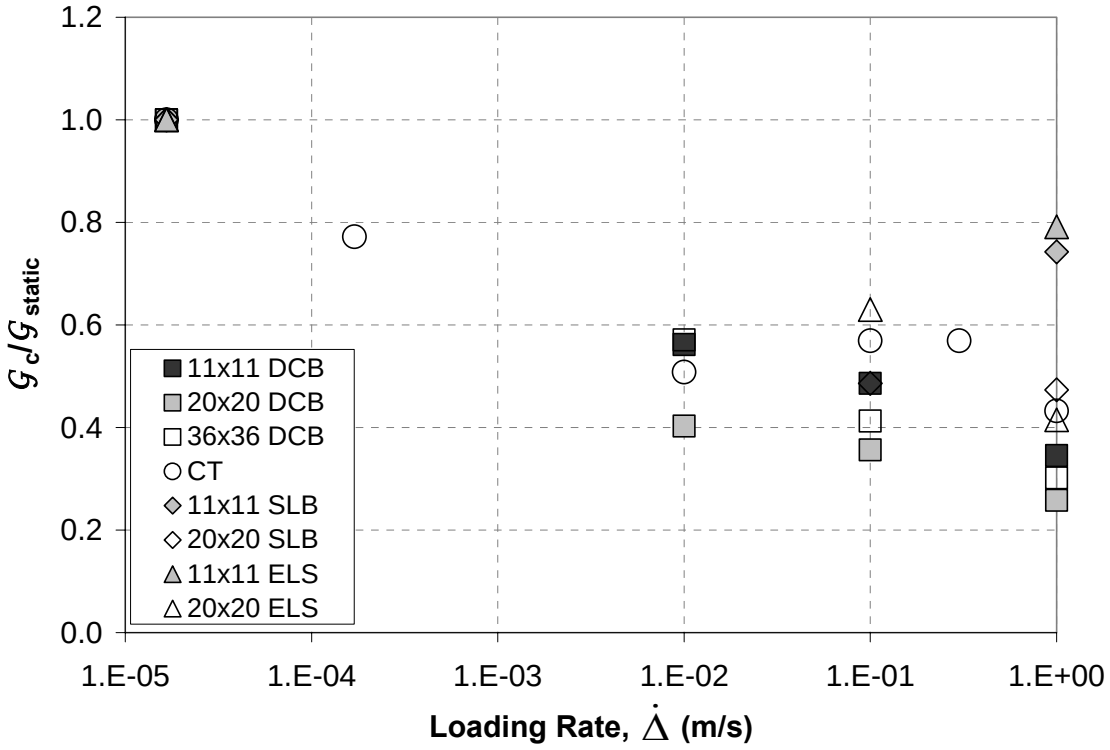

Figure 6.3. $\mathcal{G}_c/\mathcal{G}_{static}$ as a function of loading rate for various fracture specimens.

Of all of the different specimen geometries and loading conditions studied, mode III fracture behavior proved to be the most difficult to characterize. With no accepted standard for characterizing mode III fracture, the split cantilever beam specimen was

utilized for this thesis as it was of simple geometry and could be easily tested with the need for only small fixturing components. However, as suggested in the literature, and confirmed via finite element analysis conducted for this thesis, a strong mode II component dominant at the specimen edges of the SCB specimen did not allow for pure mode III fracture characterization. Numerical analyses suggest that a reduction in bond width, while maintaining the overall specimen width, may provide a means for a more effective mode III specimen geometry; however, this too does not provide a pure mode III loading condition. Although no dynamic tests were conducted using the SCB geometry, the simplicity of the specimen and test fixturing configurations would lend themselves quite well to such testing. However, an effective means for monitoring crack length via high-speed video would need to be deduced, as the test set-up is not overly conducive to obtaining visual crack length measurements.

6.2: Automotive Design Implications

Adhesively bonded primary automotive structures have the potential to provide significant weight and cost savings over current designs that make use of traditional fastening techniques, such as bolting, welding, or riveting. As such, the implementation of structural adhesives into today's automotive technology provides tangible benefits to both the manufacturer and consumer. Additionally, given the drive to implement light-weight primary composite structures into the cars of tomorrow, the need for adhesives is even more substantial. However, before the implementation of adhesives in load-bearing automotive structures can be achieved on a large scale, many factors must be considered before such a deviation from conventional practice can take place. One such factor

involves the complete understanding of the failure mechanisms responsible for energy absorption in adhesively bonded automotive structures through the combined use of refined experimental and numerical modeling techniques.

The research conducted herein provides a look at some of the experimental tools necessary for characterizing the fracture behavior of adhesively bonded composites. While the work presented in this thesis focuses on coupon-type test specimens, results obtained in combination with experimental observations are certainly transferable to larger scale component-type analyses. By measuring critical fracture energies of bonded specimens under various loading conditions, as well as determining failure loci corresponding with each of the different modes of failure, numerical analysis techniques can be developed for the purpose of simulating such structures subjected to impact loading conditions. In doing so, models can be developed for the study of bonded automotive structures, which will aid in the design process of today's automotive engineers. This characterization of a particular adhesive system will allow for the establishment of design criteria, including failure tolerance levels, which can be extended to the design floor of today's automotive industry.

Furthermore, the experimental test configurations utilized for this study provide valuable insight into both the pros and cons of some of today's fracture testing techniques. While some of the techniques utilized have achieved wide acceptance in modern experimentation, others have yet to achieve such status, which is further reason to push for wide-scale testing to better develop those techniques that may need improvement.

6.3: Future Work

Although much data has been provided, a few additional items may provide even more insight into the response and fracture behavior of the adhesive in question. Additional tests are needed on the ADCB and SLB specimens to more completely characterize the mixed-mode fracture behavior of the adhesive studied. Furthermore, the testing of asymmetric SLB specimens would also provide even more insight into the mixed-mode fracture behavior of the adhesive in question, as these specimens would provide varying degrees of mode-mixity unobtainable with symmetric SLB specimens. Additional tests on the ELS specimens are also recommended to further characterize the mode II fracture behavior of the adhesive studied. Along those same lines, asymmetric ELS specimens could also provide additional points on the fracture envelope, as these specimens too would result in additional levels of mode-mixity. Figure 6.4 illustrates the mode-mixity combinations possible with the materials utilized in this study. Also recommended for the ELS specimen geometry is the implementation of an alternative analysis technique to more accurately characterize the mode II fracture behavior. By performing a clamp calibration, a more accurate mode II correction factor can be obtained for each of the specimen configurations, which can be implemented in either an experimentally determined clamp correction technique or an effective crack length approach [4-5].

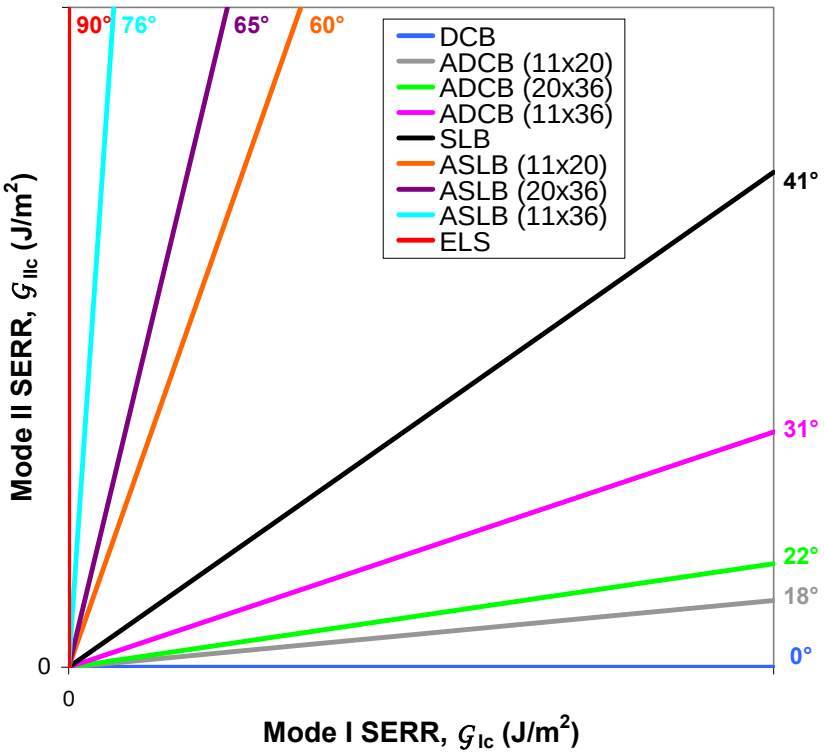

Figure 6.4. Possible mode mixities obtainable using symmetric and asymmetric specimens.

References

1. Dillard, D. A., Jacob, G. C., Pohlit, D. J., and Starbuck, J. M., "On the use of a Driven Wedge Test to Acquire Dynamic Fracture Energies of Bonded Beam Specimens: Part I - Motivation and Experimental Implementation", To be submitted (*Journal of Adhesion*).
2. Pohlit, D. J., Dillard, D. A., Jacob, G. C., Starbuck, J. M., and Kapania, R., "On the Use of a Driven Wedge Test to Acquire Dynamic Fracture Energies of Bonded Beam Specimens: Part II - Numerical Analysis", To be submitted (*Journal of Adhesion*).
3. Jacob, G. C., Starbuck, J. M., Pohlit, D. J., and Dillard, D. A., "Evaluating the Rate-Dependent Fracture Toughness of an Automotive Adhesive", To be submitted (*Journal of Adhesion*).
4. Blackman, B. R. K., Kinloch, A. J., and Paraschi, M., "The Determination of the Mode II Adhesive Fracture Resistance, G_{IIc}, of Structural Adhesive Joints: An Effective Crack Length Approach", *Engineering Fracture Mechanics*, **72**, 2005, pp. 877-897.
5. Blackman, B. R. K., Brunner, A. J., and Williams, J. G., "Mode II Fracture Testing of Composites: A New Look at an Old Problem", *Engineering Fracture Mechanics*, **73**, 2006, pp. 2443-2455.

Appendix A: Correction Factors

Correction factors have been developed previously to account for large displacements and end-block stiffening effects that are relevant to the fracture of the bonded composite joint configurations studied within this thesis. A correction factor, *F*, is used to account for the effective shortening of adherend arms that occurs under large deflections or opening displacements [1-4]. Another correction factor, *N*, is used to account for the beam stiffening effect that occurs due to the mechanically fastened steel loading blocks [1-4]. The components of these correction factor calculations, as mentioned in Section 4.1.1 of Chapter 4 of this thesis, are provided in this Appendix. Figure A.1 provides a schematic of the DCB specimen.

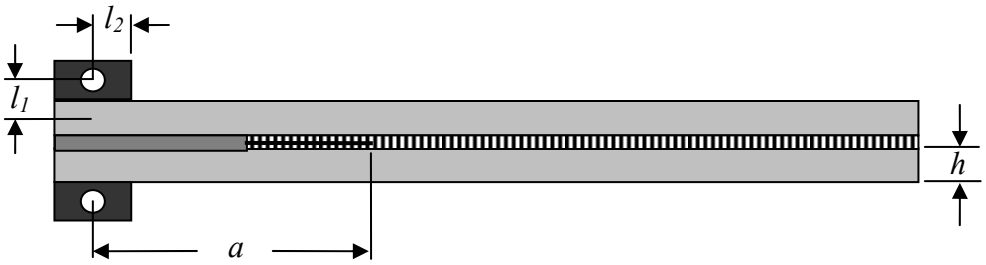

Figure A.1. Schematic of DCB specimen with load blocks.

Double Cantilever Beam:

$$\left.\begin{aligned} &\theta_1 = \frac{3}{10}, \theta_2 = \frac{3}{2}, \theta_3 = 1, \\ &\theta_4 = \frac{9}{8}\left[1 - \left(\frac{l_2}{a}\right)^2\right], \\ &\theta_5 = \frac{9}{35} \end{aligned}\right\} \tag{A.1}$$

Single Leg Bend:

$$\left.\begin{aligned}
\theta_1 &= \frac{3}{20}\left[\frac{15+150\left(a/L\right)^2+367\left(a/L\right)^4}{\left(1+7\left(a/L\right)^3\right)^2}\right] \\
\theta_2 &= 3\left[\frac{1+7\left(a/L\right)^2}{1+7\left(a/L\right)^3}\right]\cdot\left(\frac{L}{a}\right) \\
\theta_3 &= \frac{8}{1+7\left(a/L\right)^3} \\
\theta_4 &= \frac{9}{4}\left[\frac{1-\left(a/L\right)\left(1+7\left(a/L\right)^3\right)+8\left(a/L\right)^2\left(1-\left(l_1/a\right)^2\right)\left(1+7\left(a/L\right)^2\right)}{\left(1+7\left(a/L\right)^3\right)^2}\right] \\
\theta_5 &= \frac{36}{35}\left[\frac{1+7/8\left(a/L\right)^3\left(35+182\left(a/L\right)^2+367\left(a/L\right)^4\right)}{\left(1+7\left(a/L\right)^3\right)^3}\right]
\end{aligned}\right\}$$

End-Loaded Split:

$$
\left.
\begin{aligned}
\theta_1 &= \frac{3}{20}\left[\frac{15+50\left(a/L\right)^2+63\left(a/L\right)^4}{\left(1+3\left(a/L\right)^3\right)^2}\right] \\
\theta_2 &= -3\left(\frac{L}{a}\right)\left(\frac{1+3\left(a/L\right)^2}{1+3\left(a/L\right)^3}\right) \\
\theta_3 &= \frac{4}{1+3\left(a/L\right)^3} \\
\theta_4 &= -\frac{9}{4}\left[\frac{1-\left(a/L\right)\left(1+3\left(a/L\right)^3\right)+4\left(a/L\right)^2\left(1-\left(l_2/a\right)^2\right)\left(1+3\left(a/L\right)^2\right)}{\left(1+3\left(a/L\right)^3\right)^2}\right] \\
\theta_5 &= \frac{36}{35}\left[\frac{1+3/8\left(a/L\right)^3\left(35+70\left(a/L\right)^2+63\left(a/L\right)^4\right)}{\left(1+3\left(a/L\right)^3\right)^3}\right]
\end{aligned}
\right\} \qquad \text{(A.3)}
$$

References

1. Williams, J. G., "Large Displacement and End Block Effects in the 'DCB' Interlaminar Test in Modes I and II", *Journal of Composite Materials*, **21**, 1987, pp. 330-347.
2. Hashemi, S., Kinloch, A. J., and Williams, J. G., "The Analysis of Interlaminar Fracture in Uniaxial Fibre-Polymer Composites", *Proceedings of the Royal Society of London. Series A, Mathematical and Physical Sciences*, **427** (1872), 1990, pp. 173-199.
3. BSI. *BS-7991*: "Determination of the Mode I Adhesive Fracture Energy, G_{Ic}, of Structural Adhesives Using the Double Cantilever Beam (DCB) and Tapered Double Cantilever Beam (TDCB) Specimens", 2001.
4. Blackman, B. R. K., Brunner, A. J., and Williams, J. G., "Mode II Fracture Testing of Composites: A New Look at an Old Problem", *Engineering Fracture Mechanics*, **73**, 2006, pp. 2443-2455.

Appendix B: Mixed-Mode I/II ADCB Analysis

Assuming a homogeneous, isotropic, linearly elastic infinite layer of material, Hutchinson and Suo [1] were able to establish approximate solutions for the mode I and mode II stress intensity factor partitions, K_I and K_{II} , respectively, present in the mixed-mode I/II loading of asymmetric DCB specimens. The assumed geometry is illustrated in Figure B.1.

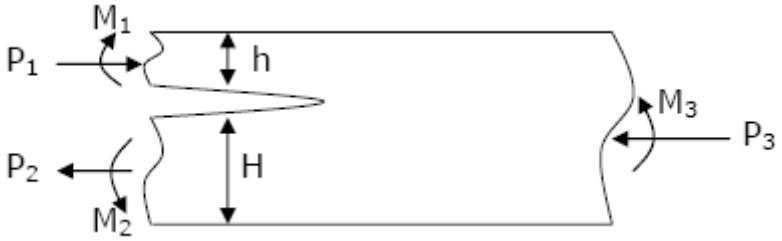

Figure B.1. Asymmetric DCB specimen generalization [2].

Solutions for geometric factors critical to the analysis of the above configuration, as discussed in Section 4.2.1 of Chapter 4 of this thesis, are provided as follows [1]:

$$\frac{1}{U} = 1 + 4\frac{h}{H} + 6\left(\frac{h}{H}\right)^2 + 3\left(\frac{h}{H}\right)^3 \tag{B.1}$$

$$\frac{1}{V} = 12\left[1 + \left(\frac{h}{H}\right)^3\right] \tag{B.2}$$

$$\sin\gamma = 6\left(\frac{h}{H}\right)^2\left(1 + \frac{h}{H}\right)\sqrt{UV} \tag{B.3}$$

$$\omega = 52.1^\circ - 3^\circ\frac{h}{H} \tag{B.4}$$

References

1. Hutchinson, J. W. and Suo, Z., "Mixed Mode Cracking in Layered Materials", *Advances in Applied Mechanics*, **29**, 1992, pp. 63-191.
2. Simón, J. C., "Response and Failure of Adhesively Bonded Automotive Composite Structures Under Impact Loads", Master's Thesis, Virginia Tech, Blacksburg, VA, 2004.